

**TWO DIMENSIONAL DELINEATION OF
SEMICONDUCTOR DOPING BY
SCANNING CONDUCTANCE MICROSCOPY**

by

Cyrus Shafai

A thesis
presented to the University of Manitoba
in partial fulfillment of the
requirements for the degree of
Master of Science
in
Electrical Engineering

Winnipeg, Manitoba, 1992

© Cyrus Shafai, 1992



National Library
of Canada

Acquisitions and
Bibliographic Services Branch

395 Wellington Street
Ottawa, Ontario
K1A 0N4

Bibliothèque nationale
du Canada

Direction des acquisitions et
des services bibliographiques

395, rue Wellington
Ottawa (Ontario)
K1A 0N4

Your file *Votre référence*

Our file *Notre référence*

The author has granted an irrevocable non-exclusive licence allowing the National Library of Canada to reproduce, loan, distribute or sell copies of his/her thesis by any means and in any form or format, making this thesis available to interested persons.

L'auteur a accordé une licence irrévocable et non exclusive permettant à la Bibliothèque nationale du Canada de reproduire, prêter, distribuer ou vendre des copies de sa thèse de quelque manière et sous quelque forme que ce soit pour mettre des exemplaires de cette thèse à la disposition des personnes intéressées.

The author retains ownership of the copyright in his/her thesis. Neither the thesis nor substantial extracts from it may be printed or otherwise reproduced without his/her permission.

L'auteur conserve la propriété du droit d'auteur qui protège sa thèse. Ni la thèse ni des extraits substantiels de celle-ci ne doivent être imprimés ou autrement reproduits sans son autorisation.

ISBN 0-315-81686-4

Canada

TWO DIMENSIONAL DELINEATION OF SEMICONDUCTOR
DOPING BY SCANNING CONDUCTANCE MICROSCOPY

BY

CYRUS SHAFAI

A Thesis submitted to the Faculty of Graduate Studies of the University of Manitoba in
partial fulfillment of the requirements for the degree of

MASTER OF SCIENCE

© 1993

Permission has been granted to the LIBRARY OF THE UNIVERSITY OF MANITOBA to
lend or sell copies of this thesis, to the NATIONAL LIBRARY OF CANADA to microfilm
this thesis and to lend or sell copies of the film, and UNIVERSITY MICROFILMS to
publish an abstract of this thesis.

The author reserves other publication rights, and neither the thesis nor extensive extracts
from it may be printed or otherwise reproduced without the author's permission.

I hereby declare that I am the sole author of this thesis.

I authorize the University of Manitoba to lend this thesis to other institutions or individuals for the purpose of scholarly research.

I further authorize the University of Manitoba to reproduce this thesis by photocopying or by other means, in total or in part, at the request of other institutions or individuals for the purpose of scholarly research.

ABSTRACT

A new technique for the two dimensional delineation of P-N junctions is presented using a Scanning Conductance Microscope (SCM). The SCM uses a conducting probe with a small radius of curvature tip, to perform localized conductance measurements over a surface in order to delineate between regions of different doping. Lateral conductivity profiles of a surface, in one or two dimensions, are obtained by scanning the surface beneath the SCM probe.

An Atomic Force Microscope (AFM) is used to maintain a low probe surface contact force. This has the effect of maintaining a small contact radius between the SCM probe and the sample. Thus, achieving high spacial resolution. Experimental results show the SCM capable of P-N junction delineation with sub-micron spacial resolution. While conductance measurements are performed, topographical information of the sample surface is obtained by the AFM. This ability cannot be achieved by other dopant profiling techniques.

A short review of techniques currently being used for doping profiling is presented. This is followed by a discussion of instrument considerations in the design of the SCM. A theoretical discussion of what factors play a part in SCM conductivity measurements is presented. Finally, results of conductivity measurements performed over a variety of samples is given.

ACKNOWLEDGMENTS

I would like to thank Professor Douglas Thomson for his advice and guidance throughout the work described in this thesis. I greatly appreciated his open door policy whenever problems, of which there were many, arose. I would like to thank Professor Howard Card for his helpful discussions, and Dr. Gord McGonigal for his help when equipment problems arose.

The assistance of my colleagues with in the Scanning Tunneling Microscopy Lab, and the VLSI group must be acknowledged. The efforts of Y. Loke, M. Normandin, and G. A. Mattiussi in providing test samples are appreciated. Finally, the financial support of the Natural Sciences and Engineering Research Council is appreciated.

TABLE OF CONTENTS

ABSTRACT		iv
ACKNOWLEDGEMENTS		v
LIST OF FIGURES		viii
LIST OF TABLES		ix
1 INTRODUCTION		1
1.1 Reason For Undertaking This Thesis		1
1.2 The Scanning Conductance Microscope		2
1.3 Instrument Considerations		5
1.3.1 The Conductance Probe		5
1.3.2 Atomic Force Microscope (AFM) Positioner		5
1.4 The Atomic Force Microscope		6
1.4.1 Controlling The Probe-Surface Contact Force		9
1.5 Schematic Of The SCM/AFM Setup		10
1.6 Abilities And Limitations Of The SCM		11
1.7 Scope Of This Thesis		12
2 SEMICONDUCTOR DOPING MEASUREMENTS:		13
CURRENT TECHNIQUES		
2.1 Introduction		13
2.2 Secondary Ion Mass Spectroscopy		13
2.3 Chemical Methods For Junction Delineation		15
2.4 Transmission Electron Microscopy		16
2.5 Capacitance-Voltage Measurements		17
2.6 Spreading Resistance		18
2.7 The Scanning Tunneling Microscope		19
2.7.1 Localized Conductance Measurements		20
2.7.2 STM Measurements In Conjunction With Preferential Etching		21
2.8 Scanning Capacitance Microscopy		21

3	THE SCM: PRACTICAL CONSIDERATIONS	23
3.1	Introduction	23
3.2	Probe Mount And Sample Setup	24
3.3	PC Interface	24
3.4	AFM Controller And Piezoelectric Scanner	25
3.5	Spring Deflection Sensor	26
3.6	The SCM Probe	30
3.6.1	The SCM Probe: Mechanical Characteristics	30
3.6.2	Probe-Surface Contact Radius	32
3.6.3	Metallized AFM Probes	34
3.6.4	Electrochemically Etched Probes	36
3.7	Circuitry Used To Perform Conductance Measurements	38
3.8	Mechanical And Electrical Isolation	40
4	THE SCM: A THEORETICAL DISCUSSION	41
4.1	SCM Conductivity Measurements: What The SCM Measures	41
4.2	Equivalent Circuit	42
4.3	Spreading Resistance	44
4.4	Contact Resistance	45
4.4.1	Barrier Height	46
4.4.2	Barrier Width	47
4.4.3	Deviations From The Ideal Contact	48
4.4.4	Current Transport Across The Barrier	49
4.5	Thermionic Emission	51
4.5.1	Ideality Factor	51
4.5.2	Conductance Simulation	52
4.6	Field Emission	55
4.6.1	Point Contact Situation	55
4.6.2	Conductance Simulation For Combined Thermionic And Field Emission	56
4.7	Space Charge Limited Conduction	59
4.8	Conductance Measurements With The SCM	60
4.8.1	Detecting Changes In Dopant Concentration	61
4.8.2	Detecting Changes In Dopant Type	62
4.8.3	An Example	62

4.9	Crossing Over A Metallurgical Junction	68
4.9.1	Width Of The SCR Between P And N Doped Regions	68
4.10	Spacial Resolution Of The SCM	69
4.11	Conductance Microscopy: An Absolute Or Relative Technique?	70
5	EXPERIMENTAL RESULTS	71
5.1	Experiment Preparation And Details	71
5.1.1	Preparing Samples	71
5.1.2	Preparing Probes	71
5.1.3	Ohmic Contact To Sample	72
5.2	Current-Voltage Characteristic Of Probe-Surface Contact	75
5.2.1	Discussion Of Current-Voltage Data	80
5.3	One Dimensional Conductance Profiling	81
5.3.1	Analysis Of Figure 5.8	85
5.3.2	Negative Biased SCM Probe	86
5.3.3	Conductivity Profile With A Tungsten Probe	91
5.3.4	Dual-Bias Conductivity Profile	94
5.3.5	Grayscale Display Of Conductance Profiles	96
5.4	Two Dimensional Conductance Profiling	98
5.4.1	Imaging P-Doped Dots	98
5.4.2	Lateral Images Of A P-N Junction	101
5.4.3	Lateral Images Of Implanted N-Type Lines	106
5.5	Experimental Artifacts	111
5.5.1	Deposited Material By The SCM Probe	111
5.5.2	SCM Probe Sticking To The Sample	111
5.5.3	Resistive Heating At The Probe-Surface Interface	111
5.5.4	Friction Heating At The Probe-Surface Interface	112
5.5.5	Differences Between Tungsten And Molybdenum Probes	112
5.6	Conclusions	113
6	RECOMMENDATIONS	114
	APPENDIX A - I-V MEASUREMENTS	115
	REFERENCES	128

LIST OF FIGURES

1.1	Schematic of a conductance measurement.	2
1.2	An example of a two dimensional conductance image obtained by the SCM.	4
1.3	Primary components of the SCM.	5
1.4	Schematic of the AFM.	7
1.5	An example of an AFM topographical image showing the ability of the AFM to resolve surfaces in three dimensions.	8
1.6	Experimental setup of the SCM.	10
3.1	Experimental setup of the SCM.	23
3.2	Probe and sample setup.	24
3.3	Laser spring deflection sensor.	27
3.4	Fiber-optic interferometer spring deflection sensor.	27
3.5	AFM spring deflection sensor.	28
3.6	AFM used as the sensor to detect vertical deflections of the SCM probe.	29
3.7	Cantilevered SCM probe.	30
3.8	Cantilevered probes used by the AFM.	35
3.9	Configuration of a simple electrochemical etchant scheme.	37
3.10	Tip changes during electrochemical etching.	38
3.11	Equivalent circuit of an SCM measurement.	39
4.1	Schematic of the conductance measurement.	41
4.2	Equivalent circuit of an SCM measurement.	42
4.3	Equivalent circuit of the probe-surface interface.	43
4.4	Spreading resistance region of an idealized point contact.	44
4.5	Energy band diagram of a rectifying metal-n-type semiconductor contact.	46
4.6	Metal-n-type semiconductor contacts with increasing dopant concentrations.	50
4.7	Current density vs. voltage characteristics of Mo-n-Si and Mo-p-Si contacts.	53
4.8	Contact resistance vs. voltage characteristics of Mo-n-Si and Mo-p-Si contacts.	54
4.9	Current density vs. voltage characteristics of Mo-n-Si and Mo-p-Si contacts for field emission.	57

4.10	Contact resistance vs. voltage characteristics for field emission, for a probe-surface contact radius of $a = 10$ nm.	58
4.11	Equivalent circuit of the probe-surface interface.	60
4.12	Current-voltage characteristic of an ideal diode.	61
4.13	Doping concentration vs. position characteristic of test sample as measured by spreading resistance profile.	63
4.14	Plot of current density vs. positive probe bias voltage.	65
4.15	Plot of current density vs. negative probe bias voltage.	66
4.16	Plot of current density vs. probe-surface barrier height.	67
5.1	Ohmic contacts placed on sample.	72
5.2	Resistance measured between the two contacts of Figure 5.1.	74
5.3	I-V measurements performed with tungsten probe [#] 1.	76
5.4	Contact resistance of I-V characteristics shown in Figure 5.3.	77
5.5	I-V measurements performed with tungsten probe [#] 3.	78
5.6	Contact resistance of I-V characteristics shown in Figure 5.5.	79
5.7	Experimental setup used to profile p-n junction.	81
5.8	Conductance profile taken with a molybdenum SCM probe biased to 0.2 volts.	83
5.9	Determination of sample edge from AFM topographical profile.	84
5.10	Conductance profile of p-n junction shown in Figure 5.8 with sample edge labeled as 0.0 μm	87
5.11	Expanded view of Figure 5.10.	88
5.12	Current profile of p-n junction taken with a molybdenum SCM probe biased to -0.2 V.	89
5.13	Expanded view of Figure 5.12.	90
5.14	Current profile of p-n junction taken with a tungsten SCM probe biased to 0.2 volts.	92
5.15	Conductance profile related to the current flow shown in Figure 5.14.	93
5.16	Dual bias scan across the p-n junction performed with a tungsten SCM probe.	95
5.17	SCM and AFM measurements across a p-n junction taken with a tungsten SCM probe biased to 0.2 volts.	97
5.18	Experimental setup used to locate p-type dots on an n-type surface.	98
5.19	Two dimensional current flow image of p-type dots on an n-type surface.	100
5.20	Lateral two dimensional current flow image of a p-n junction.	103

5.21	One dimensional cross section of the SCM profile of Figure 5.21,	104
	taken across the junction.	
5.22	Doping profile as a function of depth for the sample of Figure 5.20. . . .	105
5.23	Experimental setup used to locate n-type lines on a p-type substrate. . . .	106
5.24	Two dimensional current flow image of highly doped implanted	109
	n-type lines on a p-type substrate.	
5.25	One dimensional cross section of the SCM profile of Figure 5.24. . . .	110

LIST OF TABLES

2.1	SIMS sensitivity limits for typical dopants and contaminants in silicon. . . .	15
3.1	Probe-surface contact radius between a tungsten probe and a silicon sample calculated for a variety of applied forces.	33
4.1	Spreading resistance calculated for three probe-surface contact radii for n- and p-type silicon doped to 10^{15} atoms/cm ³ and 10^{20} atoms/cm ³ .	45

Chapter 1

INTRODUCTION

1.1 Reason For Undertaking This Thesis

To meet the challenge of producing ULSI circuits, there is an increasing need for the development of nanometer scale diagnostic measurements of semiconductor doping. In particular, there is a need to develop techniques for the two dimensional imaging of semiconductor doping type with high spacial resolution. There are a number of techniques presently used for semiconductor doping measurements. However, each of these techniques has its own weaknesses. For example, spreading resistance and secondary ion mass spectroscopy are destructive and have poor lateral resolution. Furthermore, these techniques can only make one dimensional measurements. Chemical staining and etching methods are destructive and have poor accuracy. Transmission electron microscopy is destructive and labor intensive. Recently, the Scanning Tunneling Microscope (STM) has been used to delineate P-N junctions. However, the STM is unable to scan over nonconducting regions. Many practical devices contain nonconducting regions that would pose severe problems to imaging by an STM based instrument.

This thesis was undertaken to study the merits of a new technique for P-N junction delineation based on a new instrument, the Scanning Conductance Microscope (SCM¹). This thesis will discuss instrument considerations in the design of the SCM, artifacts encountered in conductance measurements, and will provide an analysis of the SCM's capabilities.

¹ Hereafter, SCM may refer to the instrument (SC Microscope) or the field (SC Microscopy). The specific meaning will be clear from the context.

1.2 The Scanning Conductance Microscope

The principle behind the SCM's operation is relatively simple. The SCM uses localized conductance measurements, performed by a conducting probe with a small radius of curvature tip, to delineate between regions of different doping on a surface. Conductance measurements are performed as follows (see Figure 1.1). The SCM probe is placed in contact with the sample under test. A bias voltage is applied to the SCM probe which induces electric current to flow between the probe and the sample. The magnitude of the current flow is used to obtain information on the local conductivity of the probe-surface interface. One or two dimensional conductivity profiles of a surface are obtained by scanning the surface beneath the SCM probe.

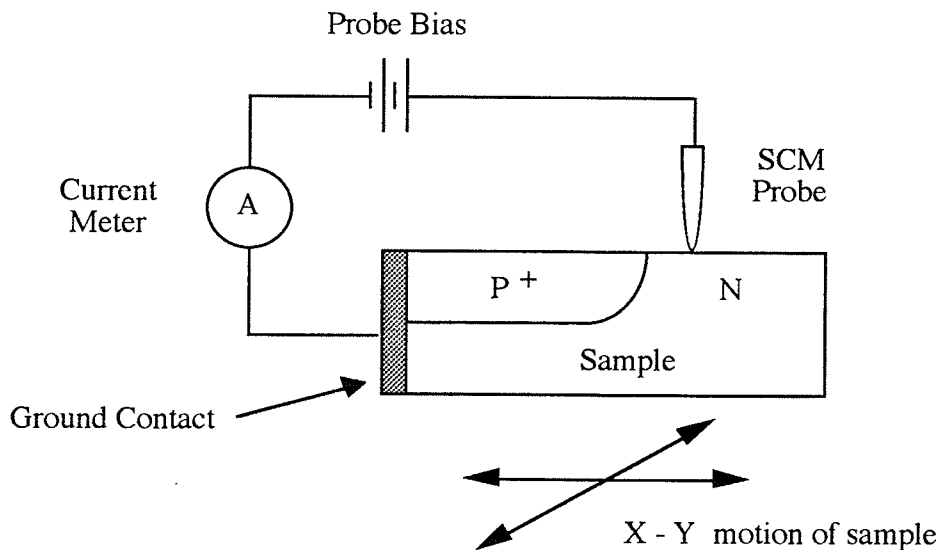


Figure 1.1: Schematic of a conductance measurement.

This idea is not new. It is the same principle used in single probe spreading resistance measurements.² There are, however, two essential differences between the SCM's operation and spreading resistance (SR) measurements.

First, in SR measurements the probe is stepped across the surface. However, the

² A discussion of spreading resistance is given in section 2.6 of this thesis.

SCM probe is not stepped over the surface, the surface is scanned beneath the probe. That is to say, the probe remains in contact with the surface as it is scanned beneath the probe. Thus, the SCM obtains a continuous conductivity profile of the surface. By raster scanning³ the surface beneath the probe, the SCM can provide two dimensional conductance profiles (sometimes referred to as conductance images) of surfaces.

Second, the SCM probe has a smaller radius of curvature tip than a SR probe. Furthermore, this probe contacts the surface with a much lower force than for SR measurements. These two factors result in the probe-surface contact size to be much smaller for the SCM than for spreading resistance.⁴ Thus, the SCM performs higher spacial resolution conductance measurements than single probe spreading resistance measurements. This thesis shows the SCM to be capable of sub-micron resolution of surface conductance over a wide range of doping concentrations.

An example of a two dimensional conductance image obtained by the SCM is shown in Figure 1.2. The sample is a p-type substrate which is covered with an implanted n-type layer. Dots, 1 μm in diameter, were masked during n-type implantation. Thus, they remain p-doped.. The scan is 7.2 μm x 7.2 μm in size, and was obtained with the SCM probe biased to 0.6 V with the p-doped substrate electrically grounded. In this image, the electric current flow between the SCM probe and the sample is represented by grayscale shading. White signifies regions of high current flow and so high conductance. Black signifies regions of low current flow and so low conductance. This image clearly shows the p-doped dots represented by regions of high conductivity. A highly conducting p-type region is also evident on the right side of this image. A detailed discussion of this image will be given in section 5.4.1 of this thesis.

³ Raster scanning is the two dimensional scanning of a surface following a pattern made up of a series of closely spaced parallel lines. For the case of the SCM, let us assume the surface is plane located on an X,Y coordinate system. Raster scanning is done by scanning the SCM probe with a higher frequency in the X direction with respect to the Y direction. Thus, the SCM probe is scanned across a surface in a two dimensional pattern made up of a series of parallel lines in the X direction.

⁴ The physical contact between the SCM probe and the sample is on the order of 10 nanometers in radius.

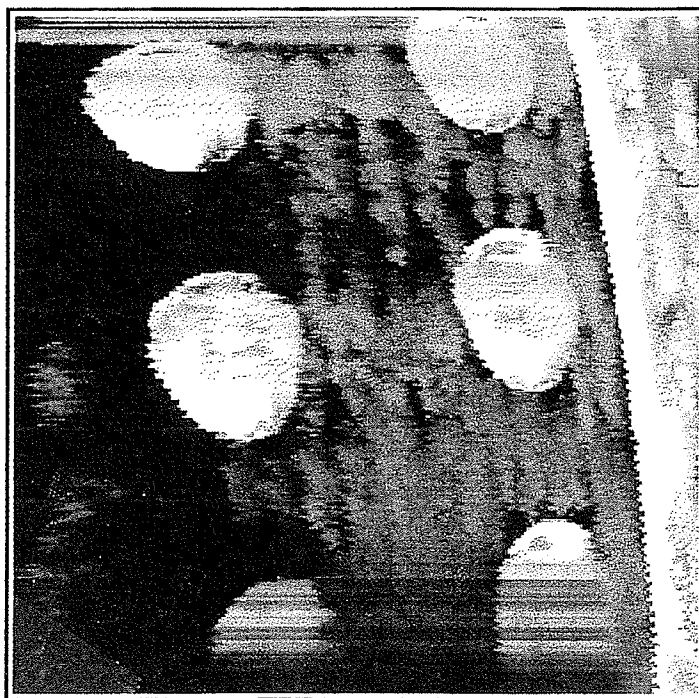


Figure 1.2: An example of a two dimensional conductance image obtained by the SCM. This image clearly shows p-doped dots represented by regions of high conductivity. A highly conducting p-type region is also evident on the right side of this image. The scan is $7.2 \mu\text{m} \times 7.2 \mu\text{m}$ in size, and was obtained with the SCM probe biased to 0.6 V with the p-doped regions electrically grounded.

1.3 Instrument Considerations

For the SCM to be effective, four elements are needed; a conducting probe with a small radius of curvature tip, a system capable of accurately positioning the probe with nanometer resolution, circuitry to perform conductance measurements, and a PC to record data (see Figure 1.3). These elements are discussed in detail in chapter 3 of this thesis. However, a brief discussion of two of these elements is provided below.

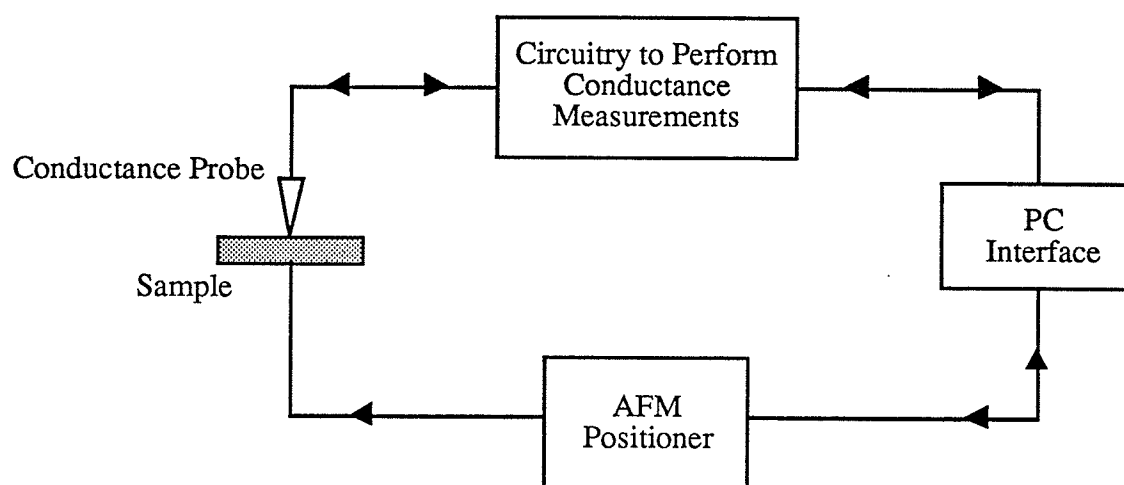


Figure 1.3: Primary components of the SCM.

1.3.1 The Conductance Probe

A cantilevered metal probe is used by the SCM to perform conductance measurements. The probe tip is electrochemically etched to provide a sharp and clean tip.

1.3.2 Atomic Force Microscope (AFM) Positioner

In order to make full use of the SCM's potential for high resolution measurements, a system is needed which is capable of providing fine control of the SCM probe position with respect to the sample. This system must be able to control probe

position in the plane parallel to the sample surface,⁵ and the must control the vertical separation⁶ between the probe and the sample. Fine control in the X,Y plane is required to obtain high resolution two dimensional conductance measurements. Fine control in the Z direction is required to maintain a low probe-surface contact force, thus, maintaining a low contact area.

A piezoelectric scanner is used to control the position of the sample with respect to the SCM probe. Piezoelectrics are ceramics which deform or bend when a voltage is applied across them. The magnitude of the displacement is a function of the applied electric field [45]. The piezoelectric scanner used by the SCM is a tube scanner, which is capable of three dimensional motion. The sample is mounted on the piezoelectric scanner, and so will displace in conjunction with the piezoelectric by the application of a voltage. The SCM described in this thesis uses an Atomic Force Microscope (AFM) to control the motion of the piezoelectric scanner.

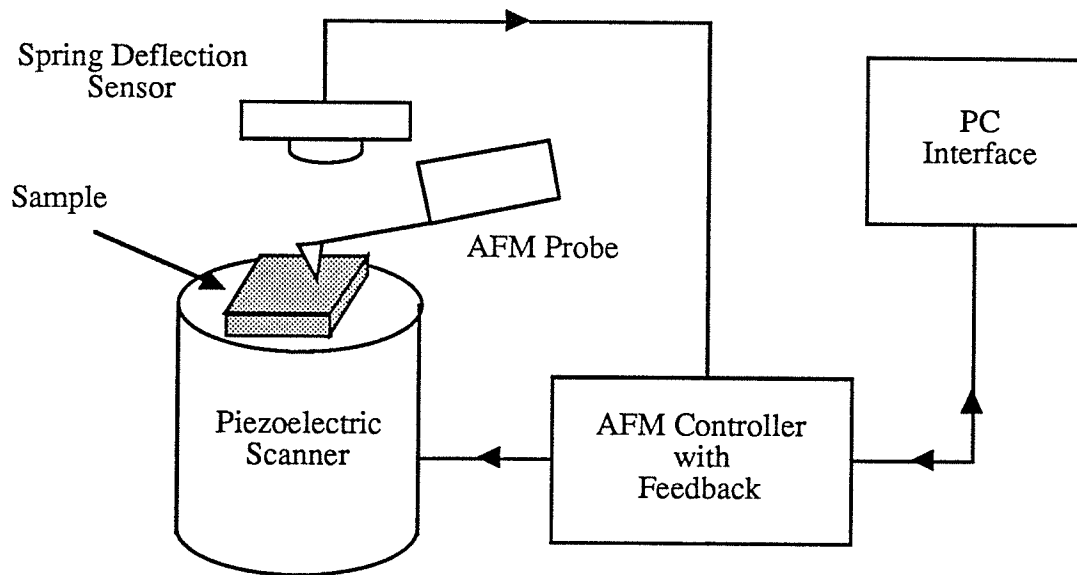
1.4 The Atomic Force Microscope

The Atomic Force Microscope (AFM) was developed in 1986 by Gerd Binnig et al. [1]. It is primarily used as a device to resolve topographical surface features. The AFM resolves surface topography as follows. The sample is mounted on the piezoelectric scanner (see Figure 1.4a). A cantilevered probe with a sharp tip is placed in contact with the sample (see Figure 1.4b). The AFM controller scans the sample beneath the probe by applying appropriate voltages to the piezoelectric scanner. Upon encountering a surface feature, the probe is deflected vertically. This deflection is monitored by a spring deflection sensor and recorded on a PC. By scanning the sample in a raster pattern beneath the probe, the AFM produces topographical maps of the surface.

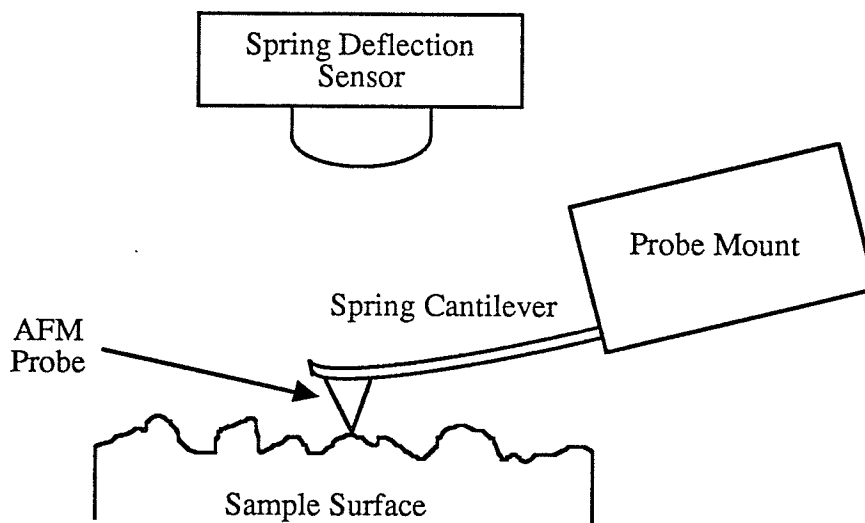
The spacial resolution of the AFM is on the order of 10's of nm in the X,Y plane, and less than 1 nm in the Z direction. The AFM attains this high resolution by using a probe with a small radius of curvature tip (approximately 30 nm), and by maintaining the probe-surface contact force very low (on the order of 10^{-8} N). These two factors result in a small probe-surface contact size, which is responsible for the AFM's high spacial resolution. An example of a topographical image obtained by the AFM is shown in Figure 1.5.

⁵ This plane is entitled the X,Y plane in this thesis.

⁶ This direction is entitled the Z direction in this thesis.



(a)



(b)

Figure 1.4: (a) Schematic of the AFM. (b) The AFM probe deflected vertically by a surface feature.

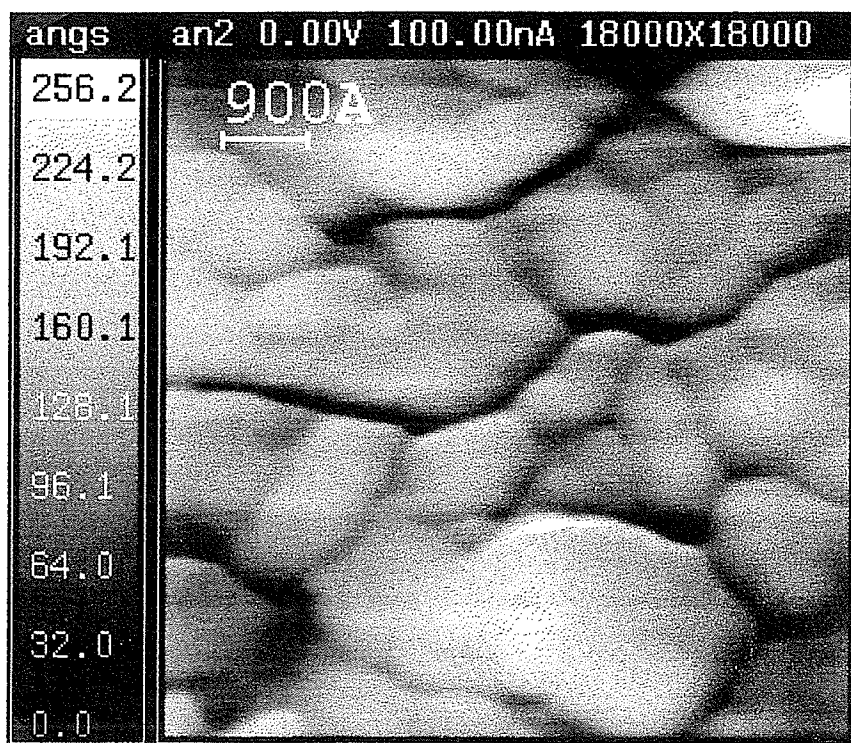


Figure 1.5: An example of an AFM topographical image showing the ability of the AFM to resolve surfaces in three dimensions. The sample is a CVD polycrystalline silicon surface after annealing. The image is $0.72 \mu\text{m} \times 0.72 \mu\text{m}$ in size. In this image, vertical height is represented by a grayscale. White signifies high surface features, and black signifies low surface features. On the left side of this image is a vertical scale which attaches height information to the grayscale.

1.4.1 Controlling The Probe-Surface Contact Force

A feedback system, located in the AFM controller, is responsible for the low probe-surface contact force. This system is coupled to the spring deflection sensor, and to the piezoelectric scanner of the AFM (see Figure 1.4a). The feedback system operates as follows.

As the sample is scanned beneath the AFM probe, the AFM probe will be deflected vertically when it encounters a surface feature. This deflection is monitored by the spring deflection sensor. The feedback system adjusts the height of the sample in an attempt to compensate for the deflection of the AFM probe. It does this by adjusting the voltage applied to the Z direction of the piezoelectric tube. Thus, the deflection of the AFM probe is kept to a minimum. This results in the feedback system maintaining a low probe-surface contact force. A discussion of the feedback control system is provided in [11] and [33].

A beneficial side effect of the feedback system's operation, is that the height of surface features becomes known through the changes in the vertical position of the sample by the feedback system. The AFM can then provide quantitative information as the height of surface features. This is not possible with optical imaging mechanisms or with the Scanning Electron Microscope (SEM). Included with Figure 1.5 is a legend indicating the height of surfaces features, as measured by the AFM.

1.5 Schematic Of The SCM/AFM Setup

A schematic of the SCM/AFM setup is shown in Figure 1.6. The sample under test is mounted on the piezoelectric scanner of the AFM. As the surface is scanned beneath the SCM probe, the spring deflection sensor monitors the SCM probe position. The AFM controller then adjusts the voltage applied to the Z direction of the piezoelectric scanner in order to maintain a low probe-surface contact force. This ensures a small probe-surface contact size, which gives the SCM high spacial resolution. Surface topography information obtained by the AFM is recorded on the PC.

Circuitry performing conductance measurements is connected to the SCM probe. Data from these measurements is recorded on the PC.

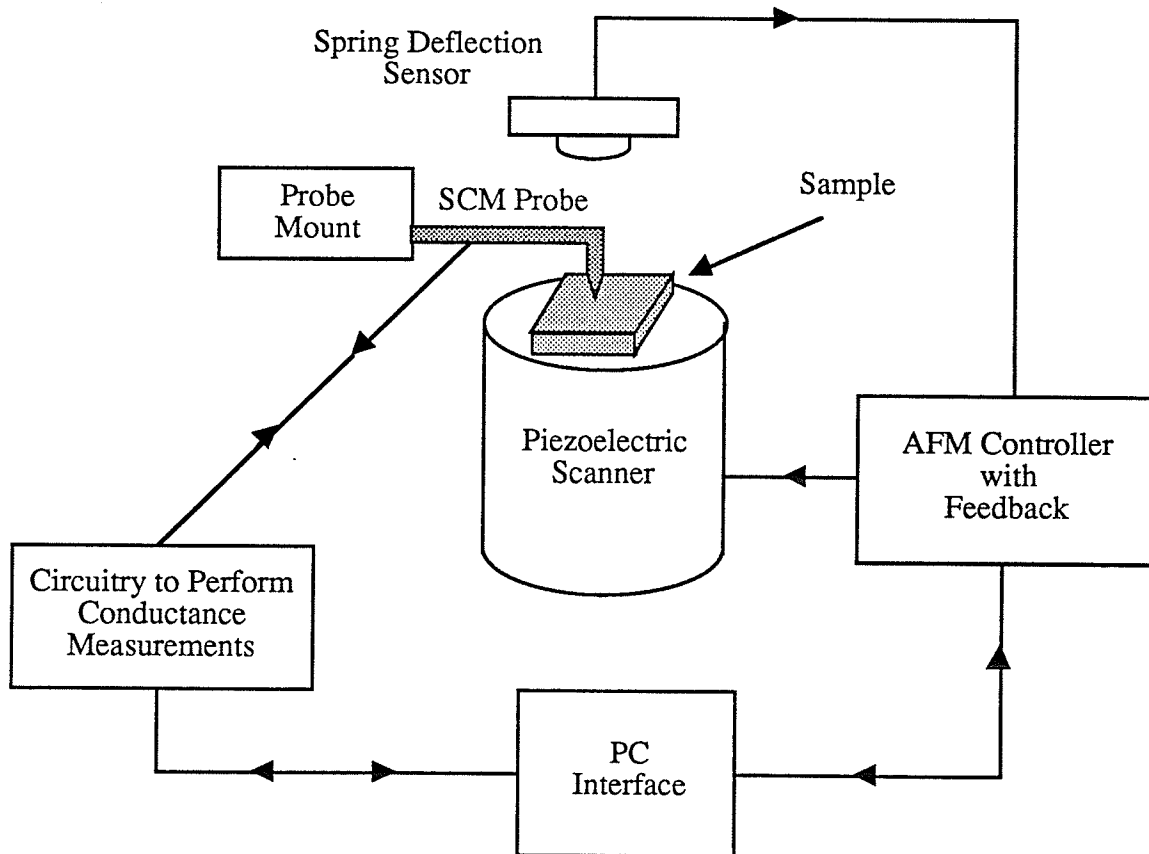


Figure 1.6: Experimental setup of the SCM.

1.6 Abilities And Limitations Of The SCM

Due to the AFM's high resolution, the SCM described in this thesis is capable of two dimensional conductance measurements with sub-micron resolution. This resolution is achieved directly on the sample surface, without the need to bevel the sample. Beveling involves the planing of the sample at a shallow angle to enhance the spacial resolution of measurements along the slope of the bevel. This results in the destruction of the sample. By not requiring the sample to be beveled, measurements made by the SCM can be made non-destructively to the sample.

One of the main advantages of an AFM based SCM, is that AFM control of the vertical position of the SCM probe is performed independently to the conductance measurements of the SCM. Thus, the AFM can be used to simultaneously obtain surface topography information, while the SCM obtains conductivity information. This ability cannot be achieved by other dopant profiling techniques.

Because the AFM mechanically probes surfaces, it is capable of operating over both electrically conducting and electrically insulating surfaces. This gives the SCM the ability to scan over regions of low conductivity. This ability is not possible with an STM based conductance microscope.

The SCM delineates between regions of different doping, by measuring the electric current flowing between the SCM probe and the sample. Because of this, the SCM is only sensitive to the concentration of electrically active dopants in the sample. Not to the total concentration of dopants.

The AFM is designed to operate in an open air environment. It (and consequently the SCM) does not require that the sample be placed in a vacuum environment. This aspect of the SCM operation does, however, result in the presence of surface contaminants or oxide on the SCM probe and on the sample. Measurements should then be performed soon after the sample, and the probe, have been cleaned of surface contaminants.

1.7 Scope Of This Thesis

- Chapter 2 will discuss techniques currently being used to measure dopant levels. The resolution of these techniques (both spacial resolution and the resolution of dopant concentration) as well as the limitations of these techniques will be addressed.
- Chapter 3 will discuss in detail the various components of the SCM.
- Chapter 4 presents a theoretical discussion of the operation of the SCM. An analysis of what factors play a part in SCM conductivity measurements is discussed.
- Chapter 5 presents experimental results obtained by the SCM. Discussions as to how experimental results relate to the theory presented in chapter 4 are given.
- Chapter 6 lists future experiments and analysis that should be done.

Chapter 2

SEMICONDUCTOR DOPING MEASUREMENTS: CURRENT TECHNIQUES

2.1 Introduction

The ability to measure semiconductor doping is required so that one can verify and study the distribution of dopants in semiconductor devices. Clearly, the techniques used for this purpose should be accurate and should yield consistent results. As devices are now being fabricated with sub-micron dimensions, dopant profiling techniques should be capable of sub-micron resolution. There is also a need for profiling techniques capable of two or three dimensional resolution. This ability is needed, as devices are now being fabricated with multi-layer dopant levels. There are a number of techniques currently used to perform doping measurements. This chapter will discuss several of these techniques in an effort to provide the reader with some background in this area.

2.2 Secondary Ion Mass Spectroscopy

Secondary ion mass spectroscopy (SIMS) is one of the most powerful and widely used techniques for semiconductor doping characterization. It is a widely used method for impurity profiling, and provides accurate and reliable results. SIMS was developed independently by two groups; Castaing and Slodzian at the University of Paris in France, and Herzog and collaborators at the GCA Corp. in the United States in the early 1960's [2]. SIMS is a destructive technique which employs a sputtering beam to remove material from the substrate under test. The ionized sputtered material is collected by a mass spectrometer, for mass-to-charge analysis to determine its atomic composition. It is worth noting, that most of the sputtered material is electrically neutral and cannot be detected by a conventional SIMS. However, a small, highly variable percentage of this

material, often in the range of 1% of the total [2], is ionized.

SIMS is quite sensitive and can detect some elements present in concentrations less than 10^{15} cm^{-3} . SIMS has a depth resolution on the order of 10 nm. It, however, has poor lateral resolution. Recent advances in this technique have reduced the lateral resolution to less than $0.5 \mu\text{m}$ [3]. However, higher sensitivity SIMS measurements are achieved when larger beam spot sizes are used (such as $100 \mu\text{m}$). This is because when smaller beam spot sizes are used, fewer total atoms are ejected from the sample. The poor lateral resolution of the SIMS technique makes the use of SIMS impractical for the two dimensional profiling of dopants on sub-micron devices.

Dopant profile measurements with SIMS are produced by sputtering the sample with ions, and measuring the secondary ion signal of a given element as a function of time. Typically sputtering energies of 1 to 20 keV are used in the SIMS technique. These energies result in the ejection of atoms (secondary ions) from the sample from depths a few monolayers deep. Over 90% of the secondary ions are ejected from the outer two monolayers of the sample [3]. The sputtering process leaves a crater on the bombarded sample, which increases in depth with time. A depth profile of dopant atoms is obtained by measuring the depth of the crater after the SIMS measurement, and using this depth to produce a plot of dopant concentration vs. depth. To achieve higher accuracy, the sputtered beam is rastered over the surface to create a crater with a flat bottom. Mass analysis of the ejected ions is only performed over the center of the crater.

SIMS detects all elemental ions, isotopes, and molecular species ejected from the sputtered sample. Thus, it is able to determine the concentration of all impurities present in the sample, from Hydrogen to Uranium. As SIMS identifies ionized molecules from their mass, it is important that the SIMS measurement be performed in a high vacuum with high resolution detectors. For example, it is difficult to detect the presence of $^{31}\text{P}^+$ ions when water vapor is present. This is because Si reacts with H to form $^{31}\text{SiH}^+$ ions which have a mass very close to $^{31}\text{P}^+$ ions.

The sensitivity of SIMS varies widely with the impurity being measured. Table 2.1 lists SIMS sensitivity limits for typical dopants and contaminants in silicon [3]. Furthermore, the sensitivity of SIMS varies with the beam used for sputtering (cesium and oxygen are typically used). For example, the detection limit for gold in silicon with an oxygen beam is $\sim 100 \text{ ppma}$,¹ while for a cesium beam it is 0.1 ppma [3]. A difference of 1000 times in sensitivity. This variation in sensitivity can render the interpretation of measured results difficult.

¹ ppma: parts per million atoms

Table 2.1: SIMS sensitivity limits for typical dopants and contaminants in silicon.

Element	Sputtering Beam	Detected Element	Sensitivity (atoms/cm ⁻³)
Arsenic	Cs ⁺	⁷⁵ As ⁻	5 x 10 ¹⁴
Phosphorus	Cs ⁺	³¹ P [±]	5 x 10 ¹⁵
Boron	O ₂ ⁺ , O ⁻	¹¹ B ⁺	1 x 10 ¹³
Oxygen	Cs ⁺	¹⁶ O ⁻	1 x 10 ¹⁷
Hydrogen	Cs ⁺	¹ H ⁻	5 x 10 ¹⁸

The SIMS measurement differs from electrical doping profile measurement techniques, such as spreading resistance or C-V measurements, in that it measures the total concentration of impurity atoms in the sample under test. Whereas, electrical measurement techniques measure the concentration of electrically active dopant atoms. SIMS can then be used to profile implanted dopants before annealing. This is not possible for electrical measurements, as the dopants are not yet electrically active.

The SIMS technique has several weaknesses. It requires complex equipment and samples must be analyzed under high vacuum conditions. It does not have the sensitivity of electrical techniques. In addition, SIMS is not applicable when the dopant species is not an impurity. For example, in p-type HgCdTe semiconductors, doping can be due to Hg vacancies in the semiconductor [2]. In this case doping concentration cannot be detected by SIMS, but can be detected by electrical methods.

2.3 Chemical Methods For Junction Delineation

Methods which use chemicals to delineate junctions are some of the fastest and simplest ways for delineating junctions. These methods take advantage of the fact that a doped region on a semiconductor will react differently to chemical attack, than a region of a different doping type or concentration. There are three types of chemical methods commonly used; staining, plating, and etching.

Staining is an oxidation-reduction reaction whereby a thin layer of oxide is grown over the semiconductor. The oxide has different optical properties over the p and n regions of the semiconductor. Plating is the deposition of a particular metal selectively on either n-type or p-type silicon. Etching is the preferential etching of either n- or p-type

Si. After staining, plating, or etching has been performed, these methods require the use of a resolving device, such as an optical microscope or a SEM, to locate and study the effected junctions. These methods are often used in conjunction with beveling to provide greater resolution.

Chemical methods can provide information as to the lateral extent of a junction in addition to depth information. However, these methods are destructive in nature. Furthermore, while these methods can be used to determine junction depth, they cannot be used to obtain the dopant profile of a junction. Chemical methods are also temperamental and so it is difficult to obtain consistent results with these methods. To over come this problem, electrochemical methods for junction plating and etching have been used, since they are more controllable and so are more reproducible. A good discussion of electrochemical plating and etching is provided in [4].

2.4 Transmission Electron Microscopy

Transmission electron microscopy (TEM) is a high resolution technique used for two dimensional junction delineation. This technique utilizes a transmission electron microscope (also referred to as a TEM) to obtain images of junctions. The high spacial resolution of the TEM, approaching 2 Å, is where the strength of this technique lies. The TEM images a sample by transmitting an electron beam (accelerated typically to 50 to 400 keV) through the sample. As the beam passes through the sample, it is scattered or diffracted by the atoms in the sample. After passing through the sample, the transmitted beam is projected on to a screen for viewing or on to a photographic plate. By analysing the image of the transmitted beam, one can determine the location of doped regions on the sample.

Variations in the scattering of the transmitted beam (and thus in the contrast of the transmitted image) are due to differences in sample thickness, crystal structure and orientation, and impurities in the sample. However, high impurity concentrations (above 10^{19} cm^{-3}) are needed to cause significant contrast change in the TEM image [5]. In order to delineate lower doped regions, the contrast in the TEM image due to these regions is artificially enhancing by reducing the thickness of select doped regions by preferential etching, or by the preferential creation of lattice defects in select doped regions.

One of the main weaknesses of the TEM technique, is the difficulty in the

preparation of samples. Because the beam is required to pass through the sample, the sample must be thin enough to transmit the beam. Samples must be prepared to thicknesses on the order of 0.1 - 1 μm depending on the accelerating voltage of the electron beam. Ion milling is commonly used to prepare samples to the required thickness [3]. This is a laborious and time consuming task. Furthermore, one has to ensure that the region of interest is present in the thinned region of the sample.

A further weakness of the TEM technique is the interpretation of TEM images. Due to the wide variety of beam scattering processes, interpretation of images can often be difficult.

2.5 Capacitance-Voltage Measurements

Capacitive-voltage (or C-V) measurements are a relatively simple method of obtaining doping depth information. C-V measurements are performed as follows. A Schottky contact is placed over the region of the sample where the measurement is to be performed. A reverse bias DC voltage is applied to the contact, which causes a reverse bias space-charge region (scr) to form. The width of this scr is determined by measuring the capacitance of the contact. By adding a small signal AC voltage to the DC bias, the junction capacitance is varied. The concentration of electrically active dopants is found from the slope of the capacitance vs. voltage curve.

For example, if we assume the junction can be represented as a parallel plate capacitor, the width of the scr is calculated using:

$$W = \frac{k\epsilon_0 A}{C} \quad (2.1)$$

where k is a constant, A is the junction area, and C is the measured capacitance. The concentration of electrically active dopants is found from:

$$N_A(W) = \frac{2}{qk\epsilon_0 A^2 [d(1/C^2)/dV]} \quad (2.2)$$

Thus, by measuring the capacitance as a function of voltage, we can use (2.1) and (2.2) to determine the concentration of electrically active dopants as a function of depth.

This method's strength lies in its simplicity. One only needs to differentiate the

C-V data to obtain doping depth information. A further advantage is that measurements can be performed non-destructively if liquid metal contacts (such as mercury contacts) are used as the Schottky contacts.

The C-V method does have several weaknesses. This method can only be applied to moderately doped materials. In addition, measurement depths are limited to a minimum depth of at least the depth of the zero bias scr formed by the Schottky contact,² and to a maximum depth by voltage breakdown. However, the maximum depth can be enhanced by performing multiple C-V measurements after etching of the junction.

2.6 Spreading Resistance

Spreading resistance (SR) is a well accepted and routinely used method for Si profiling. SR measurements are commonly performed by stepping two metal probes over a beveled semiconductor surface. As the probes are stepped over the surface, the probes are biased, and the current flowing between the probes is measured. The current vs. voltage (I-V) data is used to determine the concentration of electrically active dopants on the surface.

The probes used for SR measurements have small radius tips and are made of hardened highly conductive alloys (such as a tungsten-osmium alloy [2]). The tip-sample contact force is typically 0.1 N, and the contact radius is 1 - 10 μm . A small contact radius is a factor in obtaining high resolution measurements, as about 80% of the total potential drop due to the spreading resistance occurs within a distance of about 5 times the contact radius of the probe [2], [6]. In practice, a constant voltage of 1 to 10 mV (ie. a voltage smaller than kT/q) is applied between the probes. A voltage in this range minimizes joule heating, and non-ohmic properties of the metal-semiconductor contact [6].

The SR probes are positioned very close together, perpendicular to the slope of the beveled surface. For probe spacings ranging from 10 μm to 1000 μm , the bulk resistance of the semiconductor between the probes can be neglected. Thus, the measured resistance is primarily due to the spreading resistance of the pair of probes only, given by:

² This is not entirely true. C-V measurements can be performed with the Schottky contact slightly in forward bias.

$$R_{sp} = \frac{k\rho}{2a} \quad (2.3)$$

where k is an empirical constant, ρ is the semiconductor resistivity and a is related to the effective electrical contact radius of the probe. From equation (2.3) we see that R_{sp} is a function of sample resistivity. By comparing the measured resistance to equation (2.3), the profile of electrically active dopants beneath the probes can be determined, at least in theory.

In practice, the interpretation of measured R_{sp} is complex, as distortions in the measured data can be caused by many factors such as carrier spilling [8], surface charge [9], non-ohmic properties of the metal-semiconductor contact, sample conductivity type, sample orientation, and preparation. Furthermore, the condition of the probes affects the measured value of R_{sp} . Thus, in practice spreading resistance is not an absolute technique, but is a relative technique. The probes require periodic calibration against specimens of known resistivity. This calibration is valid only when using the same probes, probe load, sample conductivity type, orientation, and preparation.

Nonetheless, SR is a widely accepted measurement technique. It can profile a wide range of dopant concentrations, ranging from 10^{12} to 10^{21} cm^{-3} depending on the dynamic range of the electronics employed [6]. It has no depth limitation and can profile through an arbitrary number of p-n junctions.

However, SR has several weaknesses. Sample preparation is difficult, because great care must be taken to insure the bevel angle of the sample is well controlled. SR measurements are destructive and a skilled operator is required in order to obtain consistent results. Finally, SR does not work well for semiconductors other than Si or Ge, however, advances have been made in its use for GaAs semiconductors [2], [7].

2.7 The Scanning Tunneling Microscope

The Scanning Tunneling Microscope (or STM) developed in 1981 by G. Binnig et al. [10], has been used extensively for the topographic imaging of surfaces with atomic, or near atomic resolution. The STM uses the principle of quantum mechanical tunneling to achieve its high resolution. A conducting probe with a small radius of curvature tip is used by the STM to scan an object's surface. When the probe is biased and placed in close proximity to the surface (with a probe-surface separation on the order of 1 nm),

electrons tunnel between the probe and the surface. The amplitude of this tunneling current is exponentially dependant to the probe-surface spacing. It is this sensitivity to position that gives the STM its high resolution. State of the art STM's achieve a spacial resolution of approximately 2 Å parallel to a surface, and less than 1 Å perpendicular to it [11].

Recently, a number of different studies have been undertaken to investigate the STM's potential as a device for p-n junction delineation. These studies have attempted to utilize the STM's high resolving ability to obtain high resolution, two dimensional, dopant profile information. There have been two techniques used in these studies to delineate p-n junctions; localized conductance measurements, and topographical measurements in conjunction with preferential etching. These two techniques are discussed in sections 2.7.1 and 2.7.2 respectively. These techniques have been used to delineate junctions with dopant concentrations ranging from 10^{15} to 10^{20} cm⁻³ across the junction.

The major weakness encountered by STM techniques for dopant profiling, is the inability of the STM to scan over regions of low conductivity. The separation between the STM probe and the surface is maintained by a feedback system which monitors the tunneling current. The feedback system increases or decreases the probe-surface separation in order to maintain a constant tunneling current. If the STM probe is scanned over a regions of low conductivity, the probe may impact the surface. The electrical characteristics of the probe tip may be changed after this collision, resulting in subsequent errors in measurements.

The STM can then not be used to study surfaces showing significant oxidation. Surfaces must be cleaned of surface oxide and should be placed in high vacuum conditions if they are to be studied for any length of time. Furthermore, many practical devices are unsuitable for study with an STM based instrument, because they contain regions of low conductivity that are integral parts of the device itself. For example, the gate region of a MOS transistor contains several nonconducting regions.

2.7.1 Localized Conductance Measurements

The amplitude of the current tunneling between the biased STM probe and the sample is dependant on two factors; on the probe-surface separation, and on the conductivity of the probe-surface interface. If the imaged surface is a flat plane surface,

the tunneling current will only depend on the conductivity of the probe-surface interface. Thus, by scanning the STM probe in a raster pattern over the surface, a two dimensional map of the surface conductivity is obtained. This map of surface conductivity can be used to delineated between low and high doped regions on a surface. Due to the electrical nature of this technique, this technique is sensitive only to electrically active dopants.

S. Hosaka et al. [12] delineated p-n junctions at with a constant bias voltage applied to the STM probe. S. Kordic et al. [13] and [14] imaged junctions at various probe-surface bias voltages and obtained delineation of the p-n junction to within 30 nm in [13]. J. V. LaBrasca et al. [15] delineated p-n junctions with constant probe bias, and measured probe-surface I-V characteristics. H. E. Hessel et al. [16] used STM delineation of n⁺/n junctions to determine dopant migration after annealing between two differently annealed samples. P. Murali [17] used an STM to map the potential drop across a forward biased GaAs p-n junction. E. T. Yu et al. [18] used an STM to measure potential distributions across a Si(001) p-n junction with better than 100 Å resolution.

2.7.2 STM Measurements In Conjunction With Preferential Etching

Delineation of p-n junctions has been performed by using an STM to measure the resulting surface topography after preferential etching of implanted dopants. M. Tanimoto et al. [19] and T. Takigami et al. [20], used chemical etching to remove implanted boron dopant. After etching, the STM was successfully used to delineate etched regions. In [20], the profile obtained after the measurement was compared to profiles obtained after SIMS and SR measurements. The STM measurement was found to agree with these measurements.

2.8 Scanning Capacitance Microscopy

Delineation of semiconductor junctions in two dimensions has been performed successfully by scanning capacitance microscopy in [21], [22], and [23]. This technique involves the use of a scanning capacitance microscope (SCM) [24] to perform high resolution C-V measurements of a sample, as the probe of the microscope is scanned over the sample.

Capacitance measurements are performed using a small radius tip to probe the sample. The probe is not placed in contact with the sample, but rather it is maintained at a constant separation from the sample by a feedback system measuring the force between the probe and the sample. C-V measurements of the probe-surface interface are performed in a similar manner to traditional C-V measurements. The probe is biased with a small signal AC voltage added to a DC bias. The AC voltage is used to sense the probe-surface capacitance. By monitoring the capacitance as a function of probe position, it is possible to delineate between regions of different dopant concentration. In [21] and [23] junction delineation has been achieved with 100 nm resolution, over junctions with dopant concentrations ranging from 10^{15} to 10^{20} cm^{-3} across the junction.

Due to its electrical nature, this technique is sensitive only to electrically active dopants. It has an advantage over the STM technique in that it is not restricted by regions of low conductivity.

Chapter 3

THE SCM: PRACTICAL CONSIDERATIONS

3.1 Introduction

This chapter describes in detail the various components of the SCM. These components were discussed briefly in chapter 1. A schematic of the SCM/AFM setup is shown below.

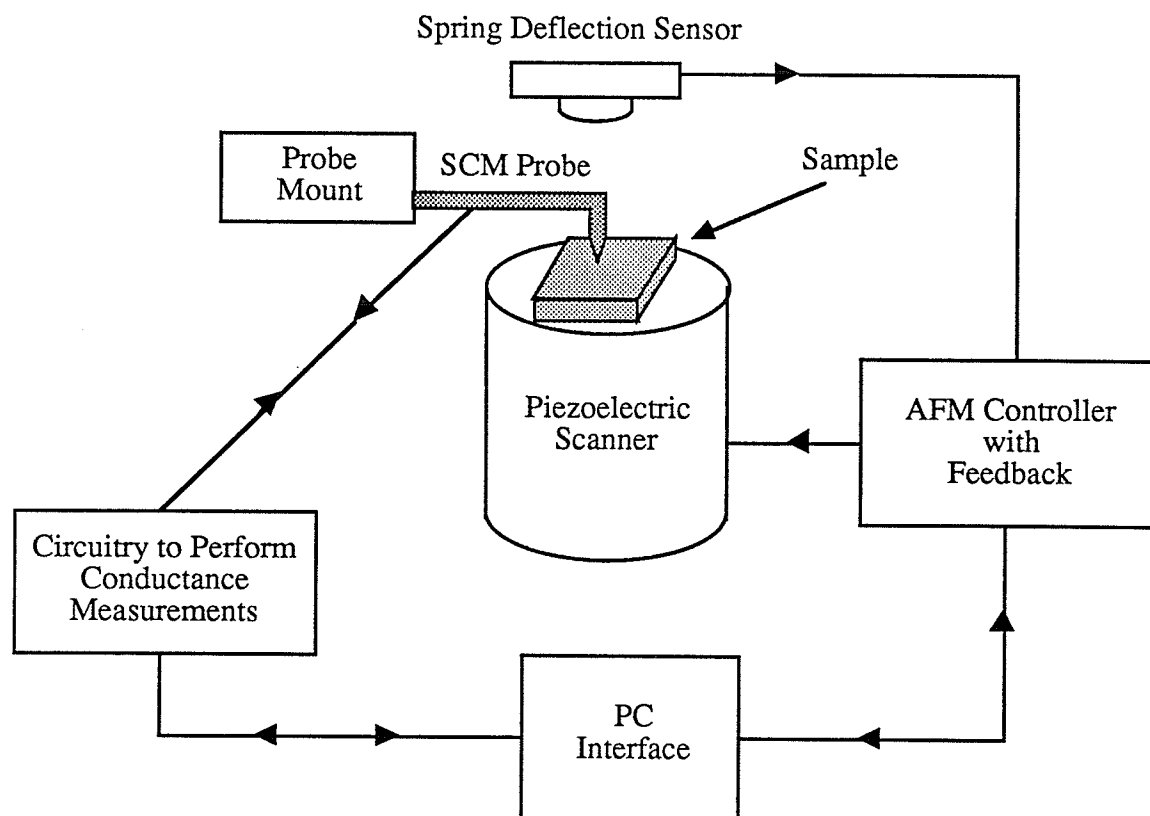


Figure 3.1: Experimental setup of the SCM.

3.2 Probe Mount And Sample Setup

A schematic of the probe and sample setup is shown in Figure 3.2. The probe mount is a Wentworth Laboratories needle probe positioner. This device has three micrometers which control the probe position in the X,Y,Z directions. This positioner is used for coarse positioning of the SCM probe over the sample. For each micrometer, one full turn corresponds to a displacement of approximately 4 mm. Fine control of the sample's position is performed by the piezoelectric tube scanner of the AFM. The sample is mounted on a sample stage, which is in turn mounted on the piezoelectric scanner. The control system of the AFM is used to control the motion of the sample in the X,Y,Z directions.

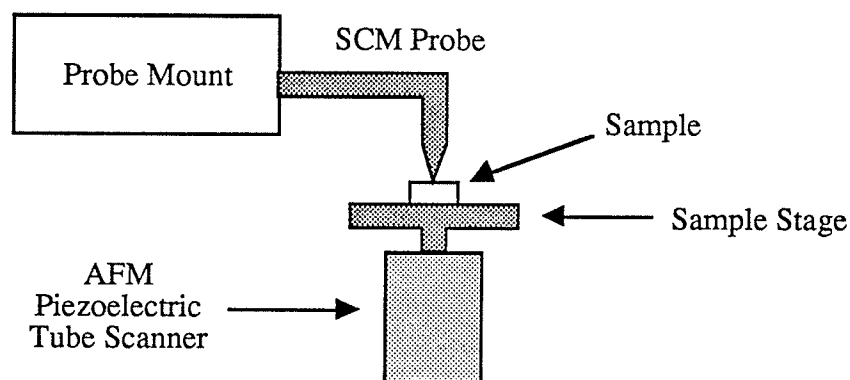


Figure 3.2: Probe and sample setup. Micrometers on the probe mount are used for coarse positioning of the probe. The piezoelectric scanner of the AFM is used for fine control of the sample position.

3.3 PC Interface

An IBM PC running custom software written at the University of Manitoba, is used to store conductance data from the SCM, as well as topographical data from the AFM. The PC is connected to measurement electronics via an interface board providing A/D, D/A, and digital I/O capabilities. Through this connection, the PC is also capable of

supplying AC or DC bias voltages to the SCM probe. A discussion of the PC set up is provided in [11].

Images of surface conductance or topography are stored on the PC as a 256 x 256 pixel image in the X and Y directions respectively. Each pixel of the image is given an integer value ranging from -2048 to 2047. For topographical images, this value represents information as to the vertical height of a given pixel with respect to neighboring pixels. For conductance images, this value represents information as to the electric current flowing between the SCM probe and the sample.

3.4 AFM Controller And Piezoelectric Scanner

A Park Scientific Instruments AFM, operated from custom electronics [11], is used to provide fine control of the sample's position. The AFM displaces the sample in three dimensions, by applying a combination of voltages around the circumference of the piezoelectric tube's inner and outer walls. The sensitivity of the piezoelectric scanner in the X,Y,Z directions to the application of voltage is:

<u>Direction</u>	<u>Sensitivity</u>
X	240 Å/V
Y	240 Å/V
Z	82 Å/V

Using our AFM setup, the piezoelectric scanner is capable of displacing the sample up to 7.2 μm in the X and Y directions, and 1.2 μm in the Z direction. The control system of our AFM enables the operator to set the size of the scan, as well as the frequency (or speed) of the scan. Typical scan frequencies are 5 to 10 Hz in the X direction. The speed in the Y direction is set to $1/512$ of the frequency in the X direction.

The reason the sample is scanned as opposed to the SCM probe is as follows. If the probe was to be displaced by the piezoelectric, it would mechanically oscillate and disturb the measurement. Moving the sample instead of the probe solves this problem.

3.5 Spring Deflection Sensor

When the SCM probe is brought into contact with the sample, or when the probe encounters a surface feature during a scan, the probe will be deflected vertically. This vertical deflection is detected by a spring deflection sensor. The output of this sensor is input to the feedback system of the AFM.¹ The AFM's feedback system controls the probe-surface contact force, which in turn determines the probe-surface contact size.

Control of the probe surface contact size is required for two reasons. First, a controlled contact size will result in consistent SCM measurements. Second, if the contact force and so the contact size can be made small, SCM measurements can be made with higher spacial resolution. It is then important that the spring deflection sensor be very sensitive to changes in the SCM probe's position.

Three different spring deflection sensors were investigated for the SCM. Each system will be discussed briefly below. Reasons as to why each system was used or not used are given.

Sensor# 1:

In this sensor, the SCM probe is placed in the path of a laser beam, which shines between a laser source and a photodetector (see Figure 3.3). The photodetector has two separate detectors; A and B. Before the SCM probe is placed in contact with the sample, the photodetector is aligned such that the laser beam strikes detectors A and B equally. Thus, the difference (A - B) is equal to zero. Any vertical deflections of the probe will result in the difference signal (A - B) deviating from zero.

This sensor has two advantages over the other two sensors which were considered. First, it is easy to align the photodetector, and thus it is easy to setup the SCM for a measurement. Second, it is easy to change SCM probes, as this only requires the photodetector to be re-aligned.

At the time this sensor was investigated, the sensitivity of this sensor and its signal to noise ratio were not sufficient to make this sensor workable. However, this design should be considered if the sensitivity and signal to noise ratio are improved.

¹ The AFM's feedback control system is discussed in section 1.4.1 of this thesis.

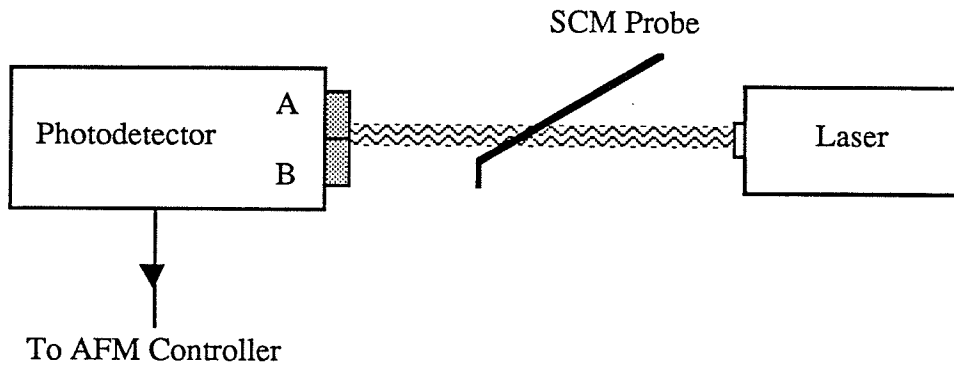


Figure 3.3: Laser spring deflection sensor.

Sensor# 2:

A fiber interferometer [31], [32] was investigated as a possible spring deflection sensor. The interferometer uses a single mode optical fiber to direct a laser beam on to the end of the cantilevered SCM probe (see Figure 3.4). The interferometer studied has a peak to peak noise from DC - 5 kHz of 0.1 \AA . The signal level measured is 3.7 mV/\AA of displacement.

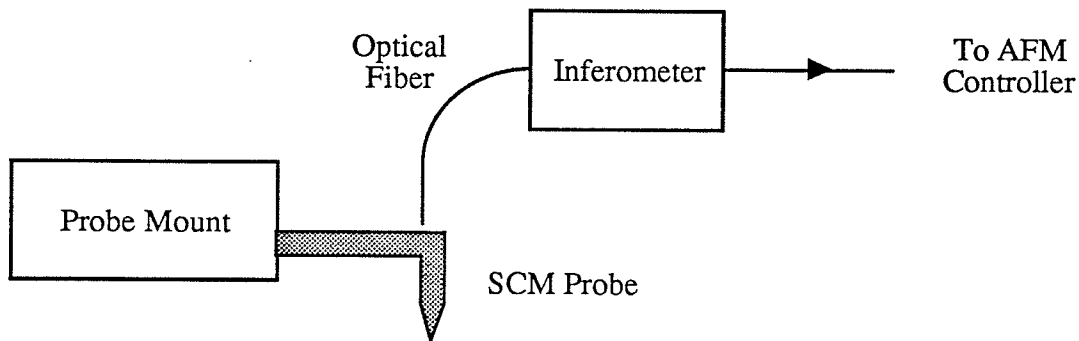


Figure 3.4: Fiber-optic interferometer spring deflection sensor.

Of the three sensors investigated, this sensor has the highest sensitivity. The signal to noise ratio of this interferometer shows that it is capable of detecting vertical

deflections of the SCM probe smaller than 1 \AA . However, a mechanism to mount the optical fiber on the SCM probe positioner was not available. In order to use this interferometer as the spring deflection sensor, it would have been necessary to position the optical fiber over a pre-positioned SCM probe. It was thought that this could be done easier with sensor# 3, and so the interferometer was not used.

Sensor# 3:

Due to the problems with the above two sensors, it was decided to use the AFM to directly monitor the position of the SCM probe. The AFM has its own spring deflection sensor which it uses to monitor its own probe² (see Figure 3.5).

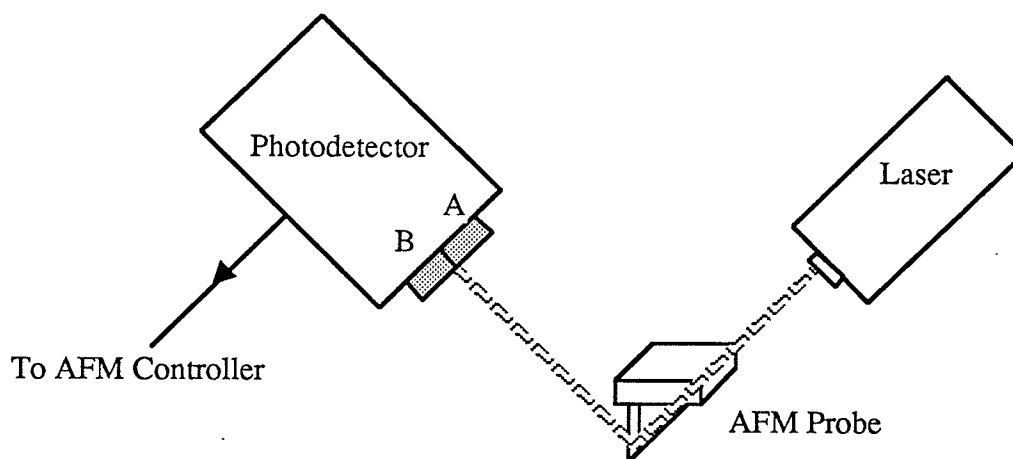


Figure 3.5: AFM spring deflection sensor. The AFM's spring deflection sensor operates as follows. The incident beam from the laser reflects off the surface of the AFM probe and strikes the photodetector. Before the AFM probe is placed in contact with a surface, the photodetector is aligned such that the laser beam strikes detectors A and B equally. Thus, the difference $(A - B)$ is equal to zero. Any vertical deflections of the probe will result in the difference signal $(A - B)$ deviating from zero.

² The AFM probes are discussed in section 3.6.3 of this thesis.

The AFM is used to monitor the position of the SCM probe as follows. A polished piece of silicon is glued to the end of the SCM probe with five minute epoxy (see Figure 3.6). The AFM probe is lowered on to the polished silicon. With this setup, any vertical deflections of the SCM probe would result in like deflections of the silicon mounted on the probe. These deflections are then detected by the AFM probe. The polished silicon is used to provide a flat surface for the AFM probe to make contact to. Initially, the AFM probe was made to contact the SCM probe directly. However, it was found that the surface of the SCM probe was too rough to provide good contact during measurements.

While this setup seems to be a good method to detect deflections of the SCM probe, it is not without problems. The main problem is that the SCM probe and AFM probe are aligned by different mechanisms. Thus, when making conductance measurements, the SCM probe must be brought into contact with the sample, before the AFM probe can be brought into contact with the SCM probe. This is done using the coarse positioning micrometers of the probe mount, with the aid of an optical microscope. This coarse positioning results in a higher probe-surface contact force, and so poorer spacial resolution for the SCM.

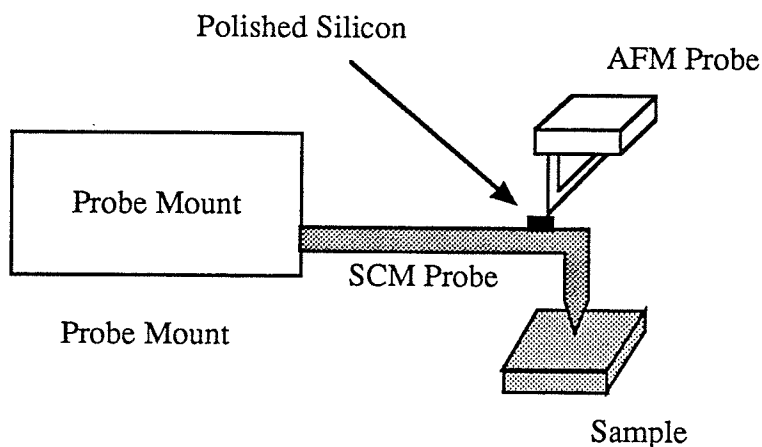


Figure 3.6: AFM used as the sensor to detect vertical deflections of the SCM probe.

3.6 The SCM Probe

The probes used by the SCM are electrochemically etched tungsten or molybdenum wires of diameter $250\ \mu\text{m}$. An SCM probe is fabricated as follows. The probe wire is first cut to a length of approximately 3 cm. The probe tip is emersed in an etchant solution and is electrochemically etched. The etched tip is bent to an angle of 90° with respect to the probe wire. The probe is mounted as shown in Figure 3.7, forming a cantilevered structure.

Discussions relating to the mechanical characteristics of the SCM probe, to the probe-surface contact radius, and to the fabrication of the probe are given in the following sections.

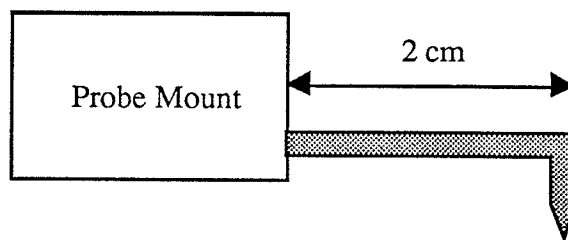


Figure 3.7: Cantilevered SCM probe. The length of the cantilevered probe is approximately 2 cm.

3.6.1 The SCM Probe: Mechanical Characteristics

The mechanical force constant of the SCM probe plays a part in the spacial resolution of the SCM. A low force constant is required to minimize the probe-surface contact force. The resonant frequency of the SCM probe plays a part in the scan speed of the surface beneath the SCM probe. A high resonant frequency would enable the conductivity scans to be made at a higher speed.

For the cantilevered structure of the SCM probe shown in Figure 3.7, we can determine the force constant and resonant frequency of the probe. As shown in [34], the

force constant and resonant frequency of a cantilevered beam, uniformly loaded by its own mass, are given by:

$$k = \frac{3EI}{L^3} \text{ N/m} \quad (3.2)$$

$$\omega_n = 3.52 \sqrt{\frac{EI}{\mu L^4}} \text{ rad/sec} \quad (3.3)$$

where E is the Young's modulus of the probe³, D is the diameter of the probe wire, L is the length of the probe, I is the area moment on the inertia of the probe, and μ is the mass per unit length of the probe. For a solid circular beam:

$$I = \frac{\pi D^4}{64} \quad (3.4)$$

$$\mu = \pi \left(\frac{D}{2}\right)^2 \rho \quad (3.5)$$

where ρ is the density of the probe material⁴. Substituting equations (3.4) and (3.5) into equations (3.2) and (3.3), the force constant and resonant frequency of the SCM probe are given by:

$$k = \frac{3\pi ED^4}{64L^3} \text{ N/m} \quad (3.6)$$

$$\omega_n = 3.52 \sqrt{\frac{ED^2}{16\rho L^4}} \text{ rad/sec} \quad (3.7)$$

Solving for molybdenum and tungsten wires of diameter 250 μm and length 2 cm, and using $f_n = \omega_n / 2\pi$ we obtain:

Molybdenum

$$k = 23.3 \text{ N/m}$$

$$f_n = 490 \text{ Hz}$$

Tungsten

$$k = 29.5 \text{ N/m}$$

$$f_n = 403 \text{ Hz}$$

³ Young's modulus of molybdenum is $320 \times 10^9 \text{ N/m}^2$, of tungsten is $410 \times 10^9 \text{ N/m}^2$.

⁴ The density of molybdenum is 10.2 g/cm^3 , for tungsten is 19.3 g/cm^3 .

When the SCM is in operation, the probe tip is contacting the sample surface. Therefore, our model of the cantilevered SCM probe is different when the SCM is in operation. We must instead consider the mechanical structure of the probe to be that of a solid circular beam fixed at both ends. The resonant frequency of such a structure is given by:

$$\omega_n = 22.4 \sqrt{\frac{EI}{\mu L^4}} \text{ rad/sec} \quad (3.8)$$

This resonant frequency is greater than that given in equation (3.3) by the ratio:

$$\frac{\omega_{n \text{ fixed-fixed}}}{\omega_{n \text{ fixed-free}}} = \frac{22.4}{3.52} = 6.36 \quad (3.9)$$

Thus, when the SCM is in operation, the resonant frequency of the above mentioned molybdenum and tungsten probes are:

$$\begin{array}{l} \text{Molybdenum} \\ f_n = 3120 \text{ Hz} \end{array}$$

$$\begin{array}{l} \text{Tungsten} \\ f_n = 2560 \text{ Hz} \end{array}$$

3.6.2 Probe-Surface Contact Radius

One of the factors governing the spacial resolution of the SCM is the radius of contact between the SCM probe and the sample under test. To achieve high resolution it is important that this contact size be very small. A small contact area is achieved by; using a small radius probe tip, and a small probe-surface contact force. As shown by Weihs et al. in [25], the probe-surface contact radius can be approximated by considering the Hertzian contact between a spherical tip and an elastic half space. Given an applied force by the SCM probe tip of P , and a tip radius of R , the contact radius a is given by:

$$a = (3RP/4E^*)^{1/3} \quad (3.1)$$

where $E^* = [(1 - \nu_1^2)/E_1 + (1 - \nu_2^2)/E_2]^{-1}$ and E_1, ν_1 and E_2, ν_2 are Young's modulus and Poisson's ratio of the tip and sample respectively. From equation (3.1), we

see that the contact radius varies with the cube root of the tip radius and the contact pressure. Thus, small changes in the tip size or contact pressure during measurements will not lead to large variations in the measured conductivity.

The contact radius between a tungsten probe and a silicon sample is calculated on Table 3.1 for a variety of applied probe loads. This calculation is done for two probe tip radii; 30 nm and 100 nm. It was felt that these two radii are good estimates of the upper and lower limits of the true tip radius after electrochemical etch [26]. These results can be applied to molybdenum probes, as the Young's modulus and Poisson's ratio of molybdenum are similar to that of tungsten.

Table 3.1: Probe-surface contact radius between a tungsten probe and a silicon sample calculated for a variety of applied forces.

Tip Radius	Contact Force	Contact Radius	Contact Pressure
100 nm	10^{-3} N	59.4 nm	9.0×10^{10} Pa
	10^{-4} N	27.6 nm	4.2×10^{10} Pa
	10^{-5} N	12.8 nm	1.9×10^{10} Pa
	10^{-6} N	5.9 nm	9.0×10^9 Pa
	10^{-7} N	2.8 nm	4.2×10^9 Pa
	10^{-8} N	1.3 nm	1.9×10^9 Pa
30 nm	10^{-3} N	40.0 nm	2.0×10^{11} Pa
	10^{-4} N	18.5 nm	9.3×10^{10} Pa
	10^{-5} N	8.6 nm	4.3×10^{10} Pa
	10^{-6} N	4.0 nm	2.0×10^{10} Pa
	10^{-7} N	1.9 nm	9.3×10^9 Pa
	10^{-8} N	0.9 nm	4.3×10^9 Pa

It should be noted that equation (3.1) applies only to an elastic contact. Thus, if the contact pressure exceeds the yield limit of the sample (or the probe), equation (3.1) will not be valid. The elastic limit for silicon is on the order of 10^9 - 10^{10} Pa. As we can see from Table 3.1, the contact pressure is on the order of the yield limit of Si. Thus, the contact may be plastic in nature. If this is the case, equation (3.1) cannot be used to

accurately approximate the contact size. For the rough calculations used in this work, equation (3.1) is assumed to be valid. However, in the future, this assumption should be verified.

It was mentioned in the discussion of sensor# 3 in section 3.5, that the SCM probe is brought into contact with the sample using the coarse positioning micrometers of the probe mount, with the aid of an optical microscope. Using the force constant of the SCM probe, and assuming that the operator can align the probe to the surface to within 10's of micrometers, the probe-surface contact force will be on the order of 10^{-4} N to 10^{-3} N. From Table 3.1, we see that this results in probe-surface contact radii between 20 nm to 60 nm, depending on the radius of curvature of the probe tip. Thus, the SCM should easily be able to achieve a spacial resolution of $< 1 \mu\text{m}$.

3.6.3 Metallized AFM Probes

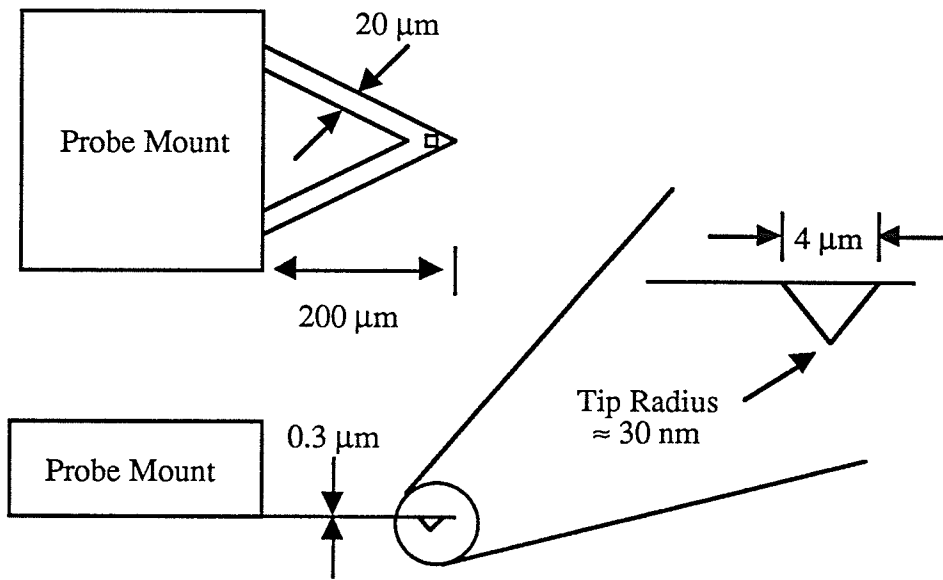
Initially, metallized AFM probes were investigated as probes for the SCM. The AFM measures the topography of surfaces with a small cantilevered probe. The probes used by our AFM are micromachined from silicon nitride (Si_3N_4). The radius of curvature of the probe tip is approximately 30 nm (see Figure 3.8a). It was felt that these probes could be used effectively for the SCM, if a thin layer of conducting material was deposited on the probe tip (see Figure 3.8b). The small radius of curvature of the probe tip would ensure high resolution conductance measurements.

Two types of metallization were investigated. Probes with 100 nm of aluminum metallization, and probes with chrome-gold metallization (40 nm chrome deposited on the probe, topped by 80 nm of gold). Both types of metallization were deposited by thermal evaporation at a pressure of less than 10^{-5} torr.

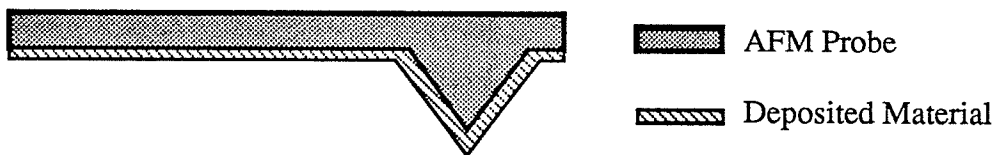
When placed into contact with a sample and biased with respect to the sample, it was found that current flowed between the probe and the sample. As was to be expected. However, this current flow decreased as the probe was repeatedly scanned over the surface, eventually reaching the point where no current flowed between the probe and sample. This result was attributed to the metallized layer rubbing off the probe tip as the probe was scanned over the surface. Referring to Table 3.1, we see that with a 30 nm contact radius and a low contact force of 10^{-8} N (this is typical for the AFM), the probe-

surface contact pressure is greater than 10^9 Pa. This is above the yield strength of deposited metallic films [42], which *suggests* that this may be the case.

The word *suggest* was used, because a definite number for the yield strength of deposited films cannot realistically be used here. Yield strengths are calculated for macroscopic samples. The probe-surface contact size is microscopic, and so the resulting yield strength may be much higher than for the macroscopic scale.



(a)



(b)

Figure 3.8: Cantilevered probes used by the AFM; (a) dimensions of the probe, (b) deposited conducting material on the underside of the probe.

Metallized AFM probes were used by Hosaka et al. in [27] to perform current measurements over silicon facets. They used AFM probes with a 20 nm platinum film deposited on the underside of the probe. During AFM topographical measurements of the surface, the metallized probes were biased and the probe-surface current flow was monitored. They found that no current flowed over flat areas of the silicon surface, but did flow at facet edges on the surface. They attributed this effect to a thinner oxide layer at the facet edges of the surface.

It is the opinion of this author that their conclusion is in error. The current flow at the facet edges is not due to a thinner oxide layer. This author proposes that the platinum metallization rubbed off of the AFM probe tip as it was scanned over the surface. However, the metallization on the sides of the probe tip would not rub off, as this location is not in continuous contact with the surface. Therefore, no current would flow when the probe is located over flat regions of the surface. When the probe is located next to a facet edge, the side of the probe would contact the facet edge. This would result in current flow, as there is still metallization on the sides of the AFM probe tip.

3.6.4 Electrochemically Etched Probes

With the failure of the metallized AFM probes (discussed in section 3.6.3), electrochemically etched metal wires were investigated as probes for the SCM. 250 μm diameter tungsten and molybdenum wires were both investigated. These two materials were chosen, first because they had a high melting point (Thus, it was felt that joule heating from the probe-sample current would not affect the probes.), and because the materials were readily available in our laboratory. These types of probes proved to be successful.

Metallic probes with small radius tips have been used extensively in the areas of Scanning Tunneling Microscopy (STM) and Field Ion Microscopy (FIM). There has then been a great deal of study regarding the fabrication of sharp tips. Methods such as electrochemical etching/polishing, chemical etching/polishing, ion milling, sputtering, whisker growth, flame polishing, vapor deposition, mechanical shaping, machining, fragmenting, cutting, and many more have been used to fabricate sharp tips. From these methods, electrochemical etching was chosen due to its relative simplicity and reliability in producing sharp tips [11], [28]-[30].

Etching is performed by suspending the tip wire below the surface of an aqueous etchant solution. The wire is biased with respect to a second electrode placed in the etchant solution (see Figure 3.9). The resulting current flow between the two emersed electrodes, results in an electrochemical etch of the tip wire. The etch of the tip wire proceeds as follows. First, the diameter of the wire decreases (see Figure 3.10) uniformly. After a time, this “necking in” process ends, and the length of the tip is decreased. As this etching process continues, the amplitude of the etchant current decreases. Etching should be stopped just before the current drops to zero to obtain the sharpest tips.

The SCM probes were etched using the simple etchant scheme shown in Figure 3.9. The probe wires were emersed to a depth of approximately 3 mm in a 1.27 M KOH solution. Typical starting currents in the etching process were 150 mA AC. Etching took approximately 2 to 3 minutes to complete. More elaborate etchant techniques can be used, but it was found that this simple technique provided tips of adequate sharpness.

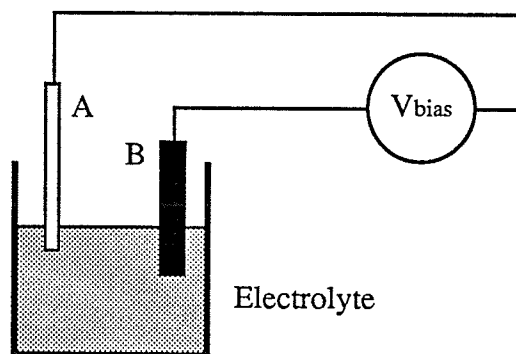


Figure 3.9: Configuration of a simple electrochemical etchant scheme. A is the wire to be etched. B is the counter electrode. V_{bias} can be either an AC or DC bias. The choice of AC or DC bias, and of bias voltage is dependant on the rate of etching desired.

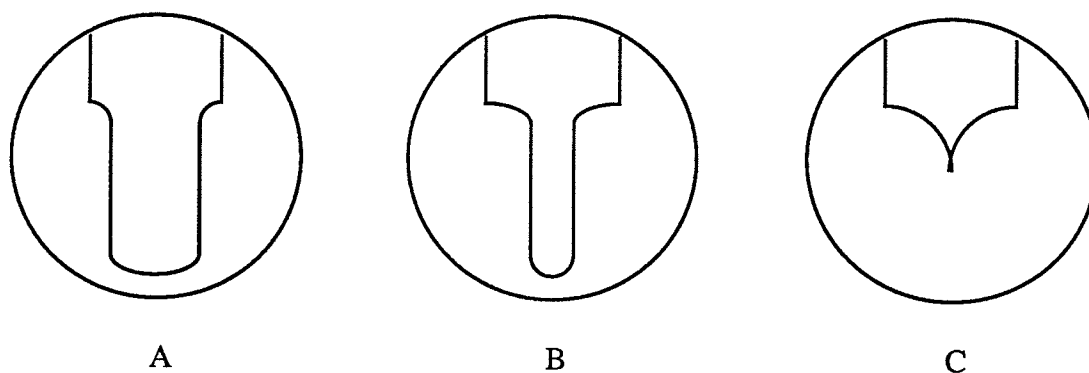


Figure 3.10: Tip changes during electrochemical etching. In A, the diameter reduces uniformly. In B, the length of the tip is reduced. At C, a sharp, well-supported tip has been formed. Etching is stopped at this point (from [11]).

3.7 Circuitry Used To Perform Conductance Measurements

Conductance measurements are made by measuring the electric current flowing between the biased SCM probe and the sample. Figure 3.11 shows an equivalent circuit of an SCM measurement. The equivalent circuit operates as follows. The conductance current (I_c) flows through the sample, and is dropped across the $10\text{ M}\Omega$ resistor, resulting in a voltage gain of 10^7 V/A . This voltage is labeled V_o . The amplified current signal is sent to the PC via a buffer amplifier.

The rationale for the various circuit components is as follows. The $10\text{ M}\Omega$ resistor is used to limit the current flow in the circuit, and to provide a voltage gain of 10^7 V/A . The 10 pF capacitor together with the $10\text{ M}\Omega$ resistor, act as a low pass filter with a cutoff frequency of approximately 1600 Hz . The buffer amplifier, fabricated from a low noise JFET op-amp, is used to isolate this circuit from the PC. The input impedance of the JFET op-amp is $10^{12}\ \Omega$.

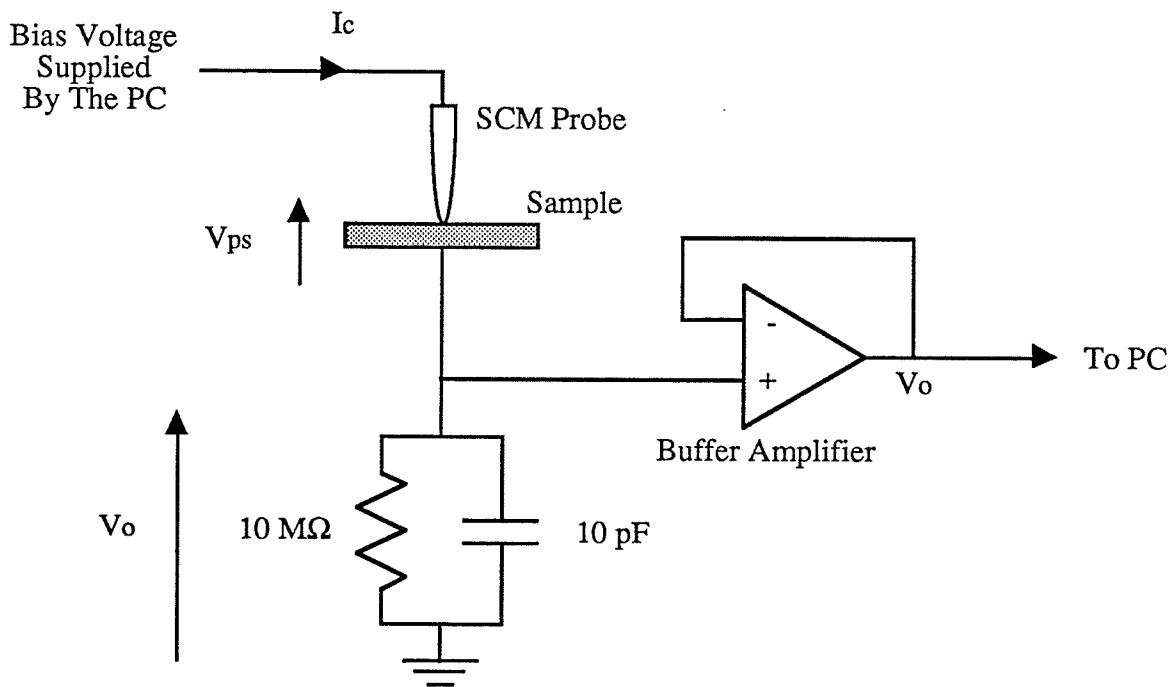


Figure 3.11: Equivalent circuit of an SCM measurement.

The conductance of the probe-surface junction is found as follows. First, the voltage V_o is subtracted from the probe bias voltage. This yields the potential drop across the SCM probe and the sample, labeled V_{ps} . Second, the voltage V_o is divided by 10^7 (the resistance of the $10\text{ M}\Omega$ resistor). This yields the conductance current flowing in the circuit, labeled I_c . The conductance of the probe-sample contact is found by dividing the conductance current I_c , by the voltage V_{ps} .

It can be seen that if the current flow is high enough, the voltage V_o may be such that the voltage V_{ps} (the probe-sample potential difference) is noticeably reduced. To avoid this, the probe bias voltage should be selected such that this will not occur.

The electrical noise inherent in the measurement electronics was measured. Noise was measured with the probe-surface contact open circuited, and with the contact short circuited by contacting the SCM probe to a metallic pad. For the open circuit case, the electrical noise was measured to be 10 mV peak to peak. For the short circuit case, the electrical noise was 5 mV peak to peak. These noise levels correspond to peak to peak

noise currents of 1 nA and 0.5 nA respectively.

3.8 Mechanical And Electrical Isolation

The area of contact between the SCM probe and the surface under test is dependant on the probe-surface contact force. Mechanical vibrations can then influence the contact area, and thus the conductance measurements. The SCM should then be operated in an environment which minimizes mechanical vibrations. The SCM is operated in a lab in the basement to minimize building vibrations. Furthermore, measurements were performed on a vibration isolation table in an effort to isolate the SCM from building vibrations.

Care was taken to reduce electrical noise in the measurement equipment used by the SCM. Techniques for electrical shielding, capacitive decoupling of power supplies and amplifiers, and for minimizing ground loops in measurement circuitry were used. Furthermore, lights were turned off around the SCM during measurements. This was done to prevent carrier generation in the sample due to the illumination by room lights. Illumination of the sample may influence the conductivity of the sample.

Although the following techniques were not used for experiments in this thesis, they should be considered for future experiments.

The SCM should be placed in an electrically shielded, solid, and opaque can for best results. The electrical shielding would reduce noise in measurements by shielding the SCM electronics from electrical noise in the environment. This is necessary because the SCM uses high gain current to voltage amplifiers for its conductance measurements, and is thus very susceptible to electrical noise. A solid can is required to isolate the SCM from mechanical vibrations due to air currents or sounds in the room. An opaque can is required to prevent light in the environment from striking the sample.

Operating the SCM in a vacuum environment would be preferable to operation in an open air environment. A vacuum environment would prevent oxidation and contaminants from forming on the sample and on the probe.

Chapter 4

THE SCM: A THEORETICAL DISCUSSION

4.1 SCM Conductivity Measurements: What The SCM Measures

As mentioned in chapter 1, the SCM operates in a manner similar to single probe spreading resistance (SR) measurements. Like SR, the SCM is an electrical conductance profiling technique. Conductance measurements are performed as follows. The SCM probe is placed in contact with the sample under test. The probe is biased with respect to the sample, and the electrical current flowing between the probe and the sample is measured (see Figure 4.1). The conductance of the probe-surface interface, at the utilized probe bias voltage, is then obtained. The factors affecting the measured conductivity are the topic of this chapter.

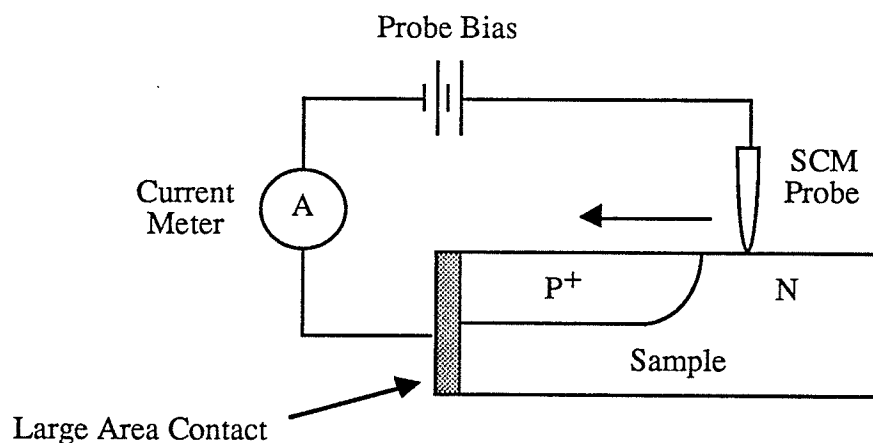


Figure 4.1: Schematic of the conductance measurement.

4.2 Equivalent Circuit

The electrical conductance measured by the SCM can be broken into four resistances¹ (see Figure 4.2). R_p is the resistance of the SCM probe wire. R_c is the resistance of the probe-surface contact. This is metal-semiconductor contact and so it has a non-linear current-voltage relationship. R_{sp} is the spreading resistance under the probe. The spreading resistance is the resistance encountered by the current flowing through the body of the semiconductor, at the probe surface interface. R_g is the resistance of the large area contact used as the return path for the current. Like R_c , this is a metal-semiconductor contact. The total measured resistance, for a given bias voltage, is given by:

$$R_T = \frac{V_{bias}}{I} = R_p + R_c + R_{sp} + R_g \quad (4.1)$$

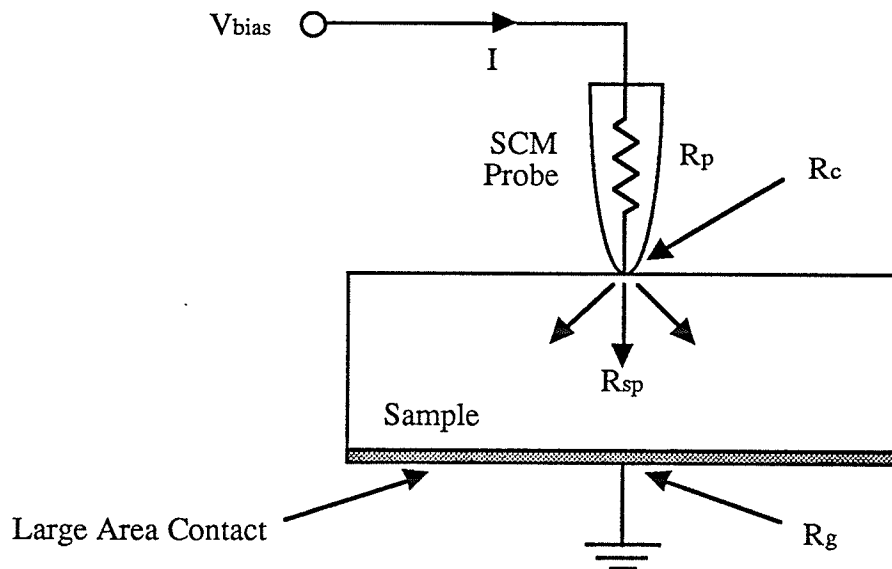


Figure 4.2: Equivalent circuit of an SCM measurement.

¹ This is assuming we ignore the internal resistance of the voltage source biasing the SCM probe, the internal resistance of the current meter measuring the current flow between the probe and the surface, and the resistance of all connection wiring.

The resistance R_p can be neglected, because the SCM probe is made from a material with a much higher conductivity than the semiconductor samples being tested (both tungsten and molybdenum wires were used as probes). This equation can be further simplified by ensuring that the resistance $R_g \ll R_c$. This is done by using a large area contact for R_g . The total measured resistance simplifies to:

$$R_T = \frac{V_{\text{bias}}}{I} = R_c + R_{sp} \quad (4.2)$$

S. Kordic et al. [35] represented the contact of equation (4.2) with the equivalent circuit of Figure 4.3.

Assuming an ideal metal-semiconductor contact between the SCM probe and the sample,² the resistances R_c and R_{sp} will depend on the following. The probe to surface contact area, the material composition of the SCM probe and the sample, the resistivity of the semiconductor beneath the probe, the current flow through the probe,³ and in the case of R_c , on the bias voltage of the SCM probe.⁴ Sections 4.3 through 4.8 of this chapter will discuss the resistances R_c and R_{sp} . Section 4.8 will discuss which of these two resistances dominates the contact resistance.

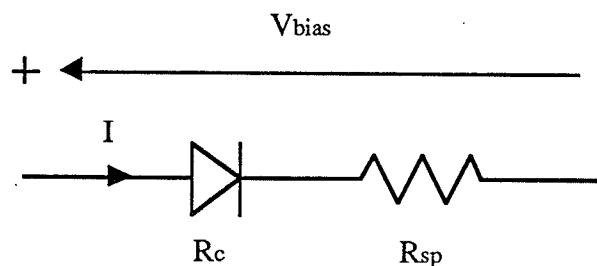


Figure 4.3: Equivalent circuit of the probe-surface interface.

-
- 2 An ideal contact, being a contact with no interfacial layer present between the probe and the surface, and with no trapped charges at the interface.
 - 3 High current flows may result in joule heating of the semiconductor, which would result in a change in the mobility of charge carriers in the semiconductor.
 - 4 The metal-semiconductor contact possesses a non-linear current voltage characteristic.

4.3 Spreading Resistance (R_{sp})

The spreading resistance is the resistance encountered by the current flowing through the body of the semiconductor, at the probe-surface interface. With the assumptions that the probe-surface contact is an indenting hemispherical contact, and that the probe is highly conducting, we can say that the hemispherical probe-surface contact is an equipotential surface of radius r_0 [36] (see Figure 4.4). The resistance of a concentric shell of thickness dr at a radius r is given by:

$$\frac{\rho dr}{2\pi r^2} \quad (4.3)$$

where ρ is the semiconductor resistivity. The total resistance encountered is then:

$$R_{sp} = \frac{\rho}{2\pi} \int_{r_0}^{\infty} r^{-2} dr = \frac{\rho}{2\pi r_0} \Omega \quad (4.4)$$

The upper limit of the integration can be taken as infinity, since the base (R_g in Figure 4.2) is a long distance away from the contact, compared to the contact radius.

Equation (4.4) shows that the spreading resistance is dependant only on the semiconductor resistivity, and on the probe-surface contact radius. Using equation (4.4), equation (3.1), and assuming a uniform electric contact, we can determine R_{sp} as a function of contact radius. Table 4.1 lists the result of this calculation for different sample resistivities and probe-surface contact radii. These probe radii are in the range expected for SCM measurements.

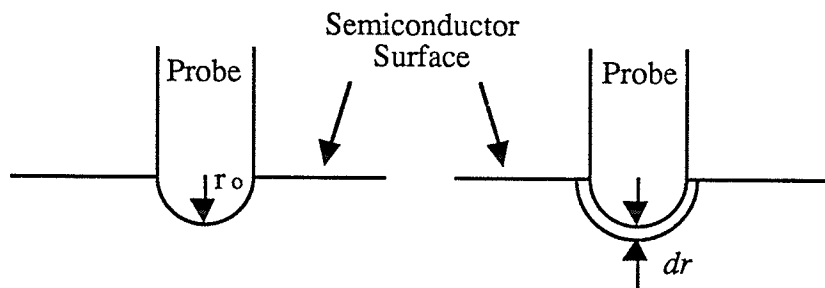


Figure 4.4: Spreading resistance region of an idealized point contact [36].

Table 4.1: Spreading resistance (R_{sp}) calculated for three probe-surface contact radii for n- and p-type silicon doped to 10^{15} atoms/cm³ and 10^{20} atoms/cm³.

Contact Radius	N-type Silicon		P-type Silicon	
	10^{15} cm ⁻³	10^{20} cm ⁻³	10^{15} cm ⁻³	10^{20} cm ⁻³
≈ 50 nm	140 K Ω	23 Ω	410 K Ω	38 Ω
≈ 10 nm	720 K Ω	110 Ω	2.1 M Ω	190 Ω
≈ 5 nm	1.4 M Ω	230 Ω	4.1 M Ω	380 Ω

4.4 Contact Resistance (R_c)

The contact resistance R_c is not so easily explained and estimated as the spreading resistance R_{sp} . R_c possesses a non-linear current-voltage relationship which results from a potential barrier which exists at the metal-semiconductor interface. The impedance of this barrier (for a given probe-surface potential difference) is a function of the barrier height and the barrier width. Application of a potential across the barrier, results in a change in the barrier height and width, which results in a change in the impedance of the barrier. The discussion below deals with a rectifying metal-n-type semiconductor contact. The results of this discussion can be applied to other metal-semiconductor contact types.

Figure 4.5 shows the energy band diagram of a rectifying metal-n-type semiconductor contact, before and after contact. The contact is assumed to be intimate, thus, there is no interfacial layer present between the metal and semiconductor. In a rectifying metal-n-type semiconductor contact, the metal work function ϕ_m is greater than the semiconductor work function ϕ_s . When the metal and semiconductor make intimate contact, electrons from the semiconductor flow into the metal. A space charge region (scr) then forms at the metal-semiconductor interface. The net flow of electrons will cease, when the space charge builds to such a level that the Fermi levels of the metal and semiconductor align.

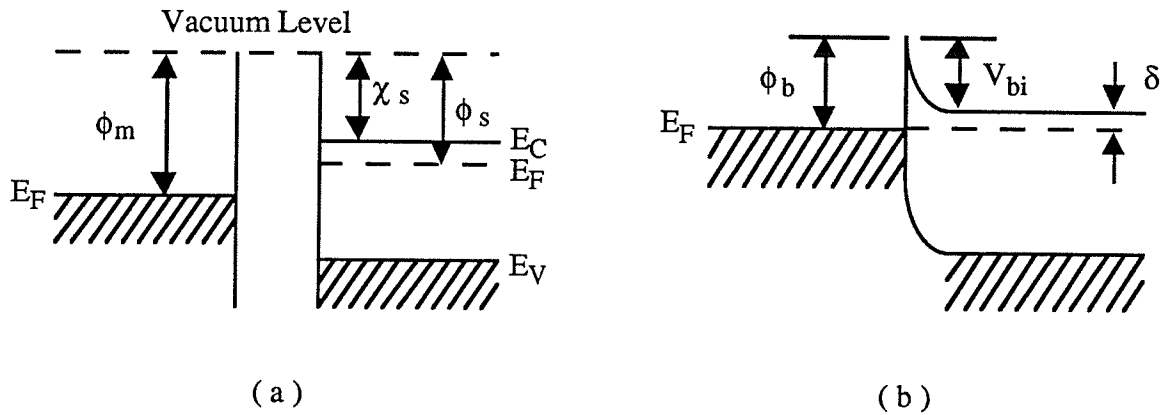


Figure 4.5: Energy band diagram of a rectifying metal-n-type semiconductor contact ($\phi_m > \phi_s$); (a) before contact, (b) after contact.

4.4.1 Barrier Height

For an ideal metal-semiconductor contact, the barrier height, as seen from the metal, is given by:

$$\phi_b = \phi_m - \chi_s \quad (4.5)$$

where χ_s is the electron affinity of the semiconductor, defined as the potential difference between the bottom of the conduction band and the vacuum level. In practice, ϕ_b does not follow the relationship of equation (4.5), but is dominated by the presence of interface states [39], [40]. Deviations from the ideal case are discussed in section 4.4.3. The built in potential for the n-type semiconductor is given by:

$$V_{bi} = \phi_{bn} - \delta \quad (4.6)$$

where ϕ_{bn} is the barrier height seen in practice, ie. not in the ideal case of equation (4.5), and δ is the difference between E_C and E_F of the semiconductor, and is given by:

$$\delta = \frac{kT}{q} \ln \left(\frac{N_c}{N_D} \right) \quad (4.7)$$

where N_c is the effective density of states in the conduction band of the semiconductor ($N_c = 2.8 \times 10^{19} \text{ cm}^{-3}$ for silicon), and N_D is the dopant concentration of the semiconductor. The potential V_{bi} can be raised or lowered, by the application of a forward or reverse bias voltage respectively, across the metal-semiconductor interface.

4.4.2 Barrier Width

For metal-n-type semiconductor contacts, the scr exists as a positively charged region in the semiconductor. For a planar contact, the width of the scr can be approximated using the abrupt-junction approximation for a P⁺/N semiconductor to semiconductor junction [37]. This is given by:

$$W_{\text{planar}} = \sqrt{\frac{2\epsilon_s}{qN_D} (V_{bi} - V)} \quad (4.8)$$

where ϵ_s is the semiconductor permittivity, N_D is the semiconductor doping, V_{bi} is the built in potential of the barrier, and V is the potential difference applied across the metal-semiconductor junction.

The situation involving the contact between the SCM probe and the semiconductor is different. Due to the small probe-surface contact radius, the contact size is on the order of, or smaller than, the scr width. Therefore, the contact cannot be considered to be planar. The situation is that of a point contact. The scr region width for a point contact is given by [36]:

$$W_{\text{pt}}^3 + 1.5aW_{\text{pt}}^2 - 1.5aW_{\text{planar}}^2 = 0 \quad (4.9)$$

where W_{pt} is the scr width for a point contact, W_{planar} is the scr width for a planar contact, and a is the contact radius. If the contact radius a is large wrt to the scr width for a planar contact (W_{planar}), W_{pt} will approach W_{planar} . If the radius a is on the order of, or smaller than, the scr width W_{planar} , W_{pt} will be thinner than W_{planar} .

4.4.3 Deviations From The Ideal Contact

In practice, the relationship of equation (4.5) is not the case. ϕ_b can be dependant on the doping of the semiconductor, or on the bias voltage applied across the metal-semiconductor contact. Two other factors which have an affect on ϕ_b are interface states, and image force. These factors were ignored in the discussions of sections 4.5 and 4.6.

Interface States:

There may be the presence of interface states (sometimes called surface states) at the metal-semiconductor interface. These states could be due to dangling bonds at the metal-semiconductor interface, or trapped charges in an interfacial layer between the metal and the semiconductor. An interfacial layer is likely due to surface contaminants or an oxide layer present on the surface of the metal and/or semiconductor.

In the absence of interface states, the charge Q_m present in the scr on the metal surface, must be equal and opposite in charge to the charge Q_s present in the scr on the semiconductor surface. Thus, $Q_m + Q_s = 0$. With presence of interface states, the neutrality condition becomes $Q_m + Q_s + Q_i = 0$, where Q_i is the charge in the interface states. The presence of interface states then affects the width of the scr, and thus affects the barrier height ϕ_b . H. C. Card et. al [38] showed that presence of an interfacial film modifies the transmission coefficient of the barrier. Furthermore, a bias dependant potential difference can be sustained in the interface. Thus, reducing the dependance of the semiconductor surface to applied bias.

If the density of the interface states is high, even after the metal is brought into mechanical contact with the semiconductor, the potential just inside the semiconductor surface will be much the same as it was before the contact was established. Thus, the barrier height ϕ_b does not depend on the metal work function ϕ_m as shown in equation (4.4). This argument was used by Bardeen to explain why the rectifying properties of semiconductors are independent (to a degree) to the work function of the metal used for the point contact [39], [40].

Image Force:

Another factor which has an affect on the barrier height ϕ_b , is the image force between an electron and the surface of the metal. When an electron approaches the metal, there exists a force of attraction between the electron and the induced positive image charge in the metal. The effect of the image force is that the barrier which an electron has to surmount in order to pass from the metal to the semiconductor, is lowered by an amount $\Delta\phi_b$. The effective barrier height is then given by [40]:

$$\phi_e = \phi_b - \Delta\phi_b \quad (4.10)$$

A discussion of the image force will not be included in the analysis of the experimental data obtained with the SCM. This is because the precision of the SCM measurements is not sufficient for such an analysis to be relevant.

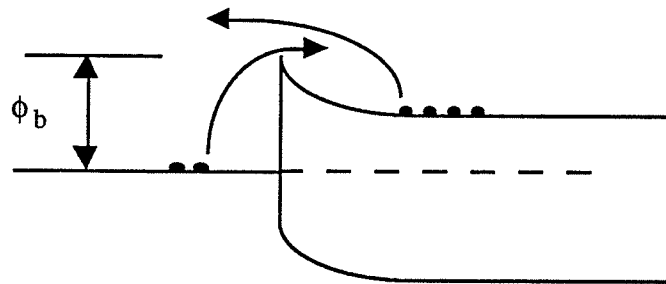
4.4.4 Current Transport Across The Barrier

Two forms of electrical conduction across the metal-semiconductor junction, thermionic emission (TE) and field emission (FE), are likely to dominate the current flow. In thermionic emission, electrons are thermally excited over the metal-semiconductor barrier. In field emission, electrons tunnel through the barrier. These two current transport mechanisms act in parallel. The current flow across the barrier is then governed by whichever of these two mechanisms is dominant.

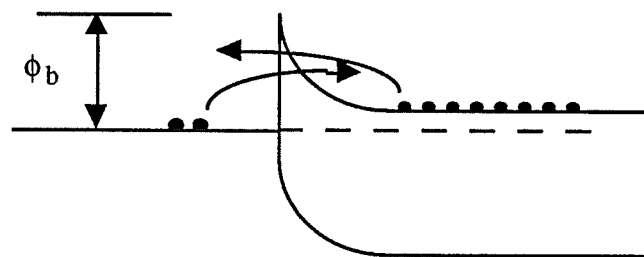
The mechanism which is dominant depends primarily on the doping concentration of the semiconductor. From equation (4.8) we see that the planar scr width (W_{planar}) is proportional to $N_D^{-1/2}$. Thus, metal contacts to higher doped semiconductors will have narrower scr widths than contacts to lower doped semiconductors. The narrower the scr width, the greater the probability of electrons tunnelling between the metal and the semiconductor.

The conduction mechanisms for metal-n-type semiconductor junctions is illustrated in Figure 4.6. For low doped semiconductors ($N_D \leq 10^{17} \text{ cm}^{-3}$), the dominant current flow mechanism is thermionic emission. For highly doped semiconductors ($N_D \geq 10^{19} \text{ cm}^{-3}$), the dominant current flow mechanism is field emission. In the intermediate

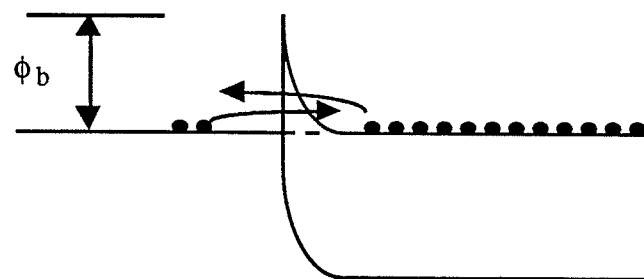
range ($10^{17} \leq N_D \leq 10^{19} \text{ cm}^{-3}$) the current flow may be a combination of these two effects [2], [37]. Sections 4.5 and 4.6 discuss these two current transport mechanisms.



(a) Low N_D : Thermionic Emission



(b) Intermediate N_D : Thermionic/Field Emission



(c) High N_D : Field Emission

Figure 4.6: Metal-n-type semiconductor contacts with increasing dopant concentrations. Electron flow is illustrated by the arrows [2].

4.5 Thermionic Emission

The thermionic emission of charge carriers across a metal-semiconductor junction is governed by the following:

$$J = J_s \left[\exp\left(\frac{qV}{kT}\right) - 1 \right] \text{ A/cm}^2 \quad (4.11)$$

$$J_s = A^* T^2 \exp\left(-\frac{q\phi_b}{kT}\right) \text{ A/cm}^2 \quad (4.12)$$

where J is the current density, J_s is the saturation current at zero bias, V is the bias voltage across the junction (positive for forward bias), and A^* is the effective Richardson constant (in units $\text{A/K}^2\text{cm}^2$) for thermionic emission. The value of A^* depends on the effective mass of the charge carrier. The approximate value used for A^* in subsequent calculations in this chapter is 110 for n-type Si, and 32 for p-type Si [37].

Equation (4.11) and (4.12) show that the thermionic emission current is not dependant on dopant concentration (This is assuming the work function difference ϕ_b does not change with doping).

In practice, the voltage drop V across the metal-semiconductor contact will never reach the barrier height ϕ_b . When V approaches ϕ_b , the current flow will make the voltage drop across the series spreading resistance R_{sp} (see Figure 4.3), dominant. Thus, when making calculations in a practical device, the voltage V in equation (4.11) should be represented as $V - IR_{sp}$, where IR_{sp} is the series voltage drop across to the spreading resistance R_{sp} .

4.5.1 Ideality Factor

Diodes do not always satisfy the thermionic emission equation (4.11) exactly. They can more closely be represented by the following equation:

$$J = J_s \left[\exp\left(\frac{qV}{nkT}\right) - 1 \right] \text{ A/cm}^2 \quad (4.13)$$

where n is the ideality factor of the diode. n is approximately independent of V and is greater than one. For low values of n ($n < 1.1$), the current flow can be determined accurately by the thermionic emission theory. For large values of n , the metal-semiconductor junction is not ideal, and the current flow cannot be determined accurately by the thermionic emission theory. Large values of n may be due to the presence of a thick interfacial layer, the recombination of charge carriers in the scr region, or to a bias dependance of the barrier height ϕ_b [38], [40].

4.5.2 Conductance Simulation

Using equations (4.12) and (4.13), an analysis of ideal metal-semiconductor contacts governed by thermionic emission can be performed. Figure 4.7 (a) and (b) are plots of the current density vs. probe-to-surface voltage for molybdenum contacts to n-Si and to p-Si semiconductors. Calculations were performed for the ideality factors of $n = 1$ and $n = 2$, at temperature of $T = 300$ °K. The value of ϕ_b for Mo-n-Si and Mo-p-Si contacts are taken to be 0.68 eV and 0.42 eV respectively [37].⁵

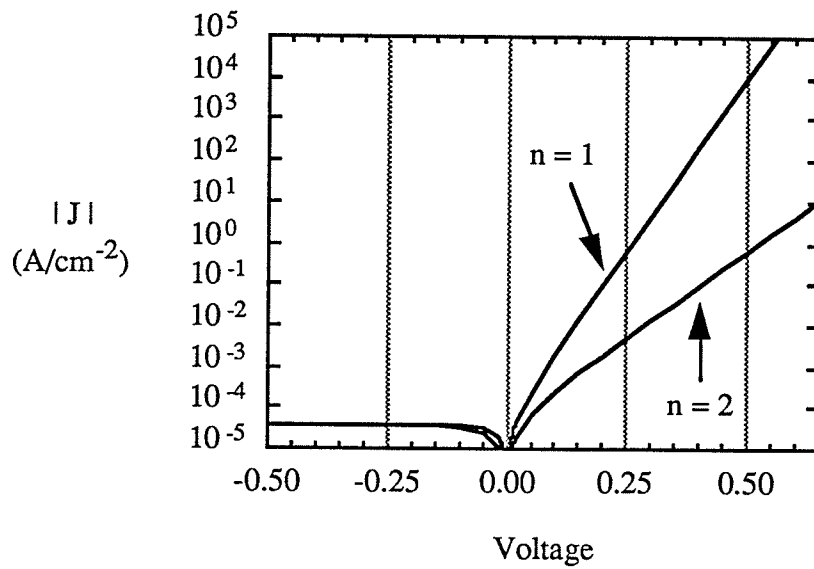
From these plots we can see that the Mo-p-Si contacts are more conductive than Mo-n-Si contacts.

Using the current vs. voltage characteristics of Figure 4.7, the contact resistance R_c can be determined from the relationship:

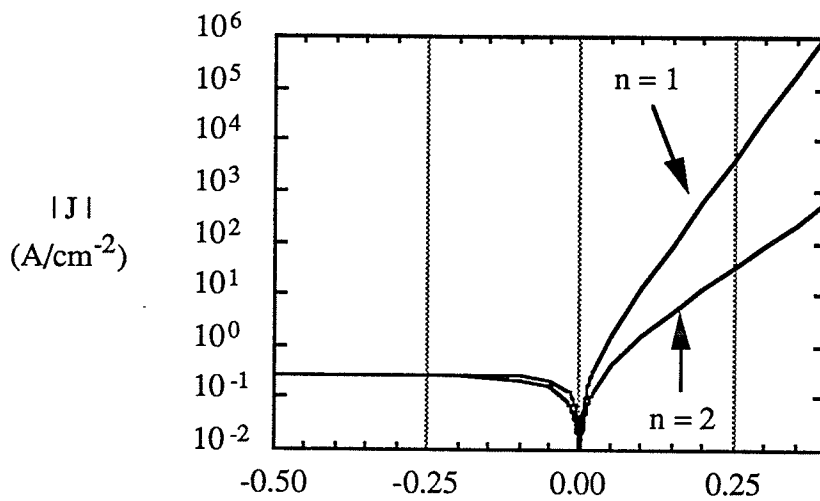
$$R_c (V_{\text{bias}}) = \frac{\partial V}{\partial I} \Omega / \text{cm}^2 \quad (4.14)$$

Plots of R_c vs. probe-to-surface bias voltage are given in Figure 4.8 for three probe-surface contact radii; $a = 5$ nm, $a = 10$ nm, and $a = 50$ nm. These contact radii are in the in the range expected for SCM measurements. R_c was calculated for an ideality factor of $n = 1$, at a temperature of $T = 300$ °K. These plots were calculated by neglecting the series spreading resistance R_{sp} (see Figure 4.3). The effect of the series spreading resistance will be discussed in section 4.8.

⁵ The data in Figure 4.7 for Mo-Si contacts is also a good approximation for W-Si contacts, as the value of ϕ_b for Mo-Si is close to that for W-Si. ϕ_b for W-n-Si and W-p-Si contacts are taken to be 0.67 eV and 0.45 eV respectively [37].

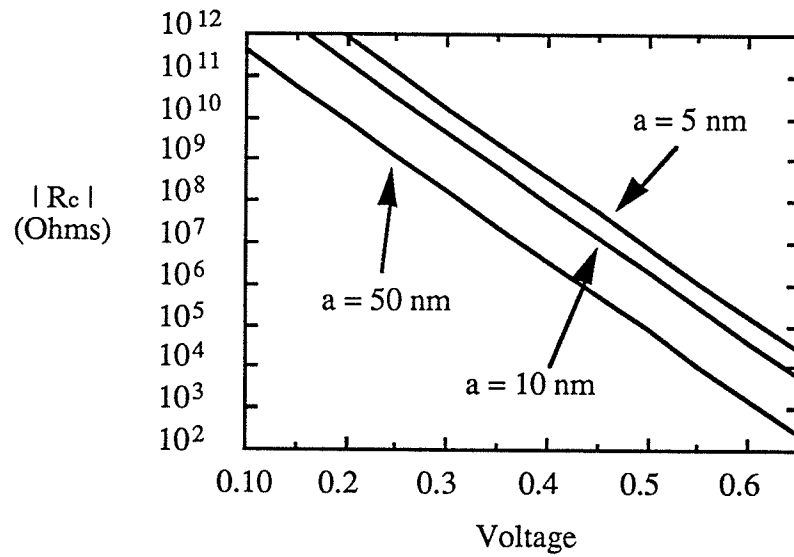


(a) Mo-n-Si contact

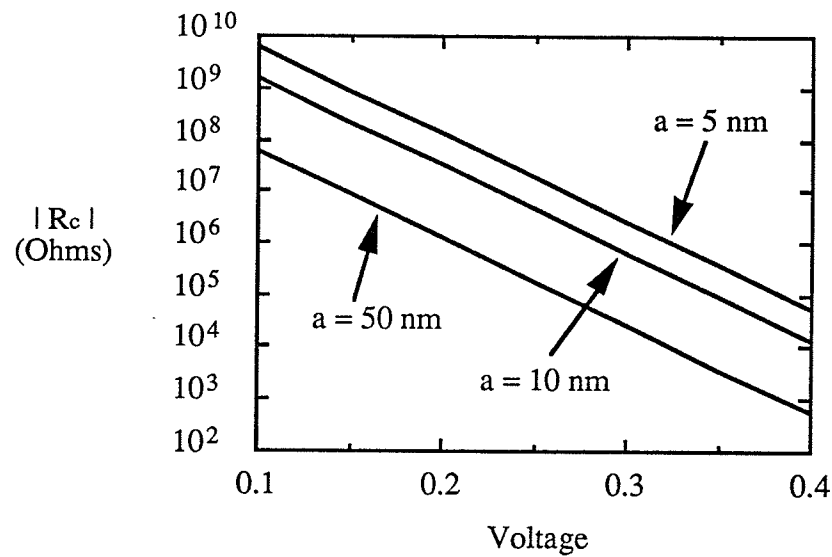


(b) Mo-p-Si contact

Figure 4.7: Current density vs. voltage characteristics of Mo-n-Si and Mo-p-Si contacts. Positive voltage is forward bias in both plots. Calculations were performed for a temperature of $T = 300 \text{ }^\circ\text{K}$.



(a) Mo-n-Si contact



(b) Mo-p-Si contact

Figure 4.8: Contact resistance vs. voltage characteristics of Mo-n-Si and Mo-p-Si contacts. Positive voltage is forward bias in both plots. Calculations were performed for a temperature of $T = 300$ °K, with $n = 1$.

4.6 Field Emission

At room temperature, the dominant current flow mechanism for metal contacts to highly doped semiconductors is primarily field emission. The magnitude of the field emission current is very sensitive to semiconductor doping, and is exponentially dependant on $(N_D)^{-1/2}$. Using the WKB (Wentzel-Kramers-Brillouin) approximation, the field emission current of a metal semiconductor barrier can be approximated as (for low temperatures, and for $V < \phi_b$) [41]:

$$J = J_s \left[\exp\left(\frac{qV}{kT}\right) - 1 \right] \text{ A/cm}^2 \quad (4.15)$$

$$J_s = A^* T^2 \left(\frac{qE_{00}}{kT}\right)^2 \frac{(\phi_b - V)}{\phi_b} \exp\left(-\frac{2(\phi_b)^{3/2}}{3E_{00}\sqrt{\phi_b - V}}\right) \text{ A/cm}^2 \quad (4.16)$$

where J is the current density, J_s is the saturation current at zero bias, V is the bias voltage across the junction (positive for forward bias), A^* is the effective Richardson constant (in units $\text{A/K}^2\text{cm}^2$), and

$$E_{00} = \frac{2}{\alpha} \sqrt{\frac{N_D}{2\epsilon}} \text{ eV} \quad (4.17)$$

$$\alpha = \frac{4\pi\sqrt{2m^*}}{h} \quad (4.18)$$

where ϵ is the dielectric permittivity of the semiconductor ($11.9\epsilon_0$ for silicon), N_D is the dopant concentration of the semiconductor, h is Planck's constant, and m^* is the effective mass of charge carriers. The effective mass was taken to be $2.15m$ for $\langle 111 \rangle$ n-type silicon and $0.66m$ for p-type silicon, where m is the mass of an electron [41].

4.6.1 Point Contact Situation

The above equations governing field emission were derived for the case of a planar metal-semiconductor contact. In such a contact the space charge region (scr) width (W_{planar}) is given by equation (4.8). However, in the case of the SCM, the

situation is that of a point contact (see section 4.4.2). The scr region width for a point contact (W_{pt}) is given by equation (4.9). This equation indicates that W_{pt} is smaller than W_{planar} . This smaller width results in a higher electric field across the scr. The smaller scr width and higher electric field would result in a field emission current that is higher than that for the planar contact case.

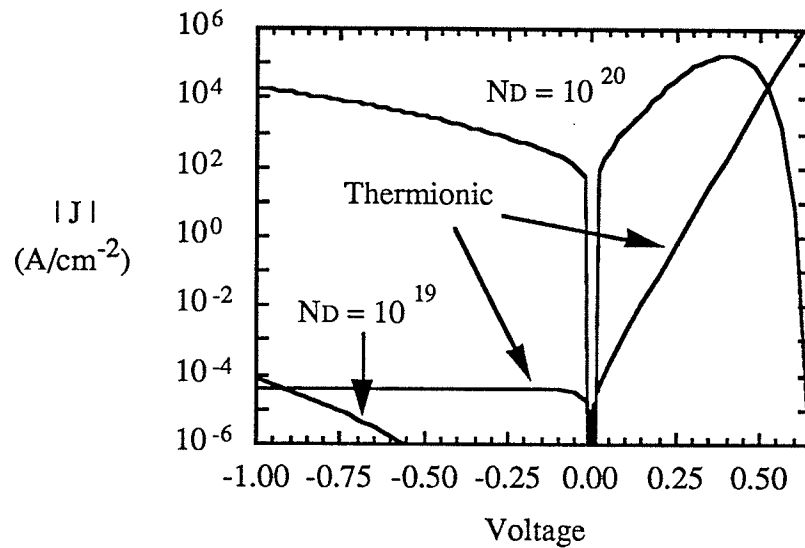
This thesis will not discuss equations governing field emission for a point contact situation. The analysis of section 4.6.2 involves the use of field emission equations for a planar contact situation. However, it should be noted that the analysed metal-semiconductor contact will be more conductive than what is shown by the results of section 4.6.2.

4.6.2 Conductance Simulation For Combined Thermionic And Field Emission

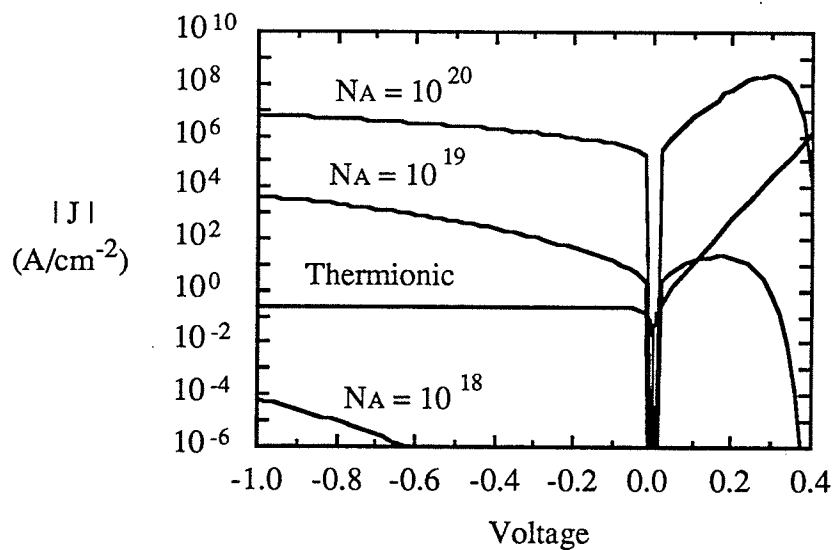
Figure 4.9 (a) and (b) are plots of the current density vs. probe-to-surface voltage of Mo-n-Si and Mo-p-Si contacts due to field emission. Calculations were performed at a temperature of $T = 300$ °K. For comparison, the current density vs. voltage characteristic for thermionic emission with an ideality factor of $n = 1$ is included. The contact resistance R_c of these contacts is found using equation (4.14). Results are plotted on Figure 4.10 (a) and (b) for a probe-surface contact radius of $a = 5$ nm.

From these plots we can see several things. First, Mo-p-Si contacts are much more conductive than Mo-n-Si contacts. Second, the magnitude of the field emission current is highly dependant on doping. Finally, in highly doped semiconductors, field emission is the dominant current flow mechanism.

The plots of Figures 4.9 and 4.10 were calculated by neglecting the series spreading resistance R_{sp} (see Figure 4.3). The effect of the series spreading resistance will be discussed in section 4.8.

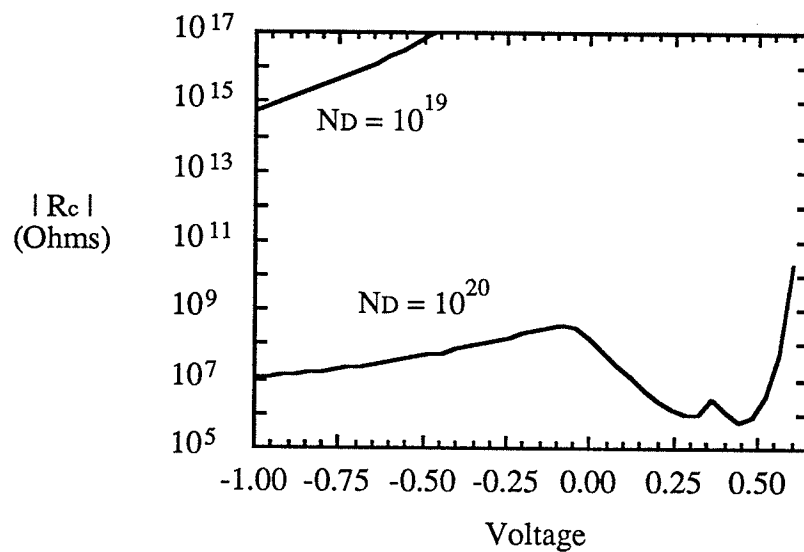


(a) Mo-n-Si contact

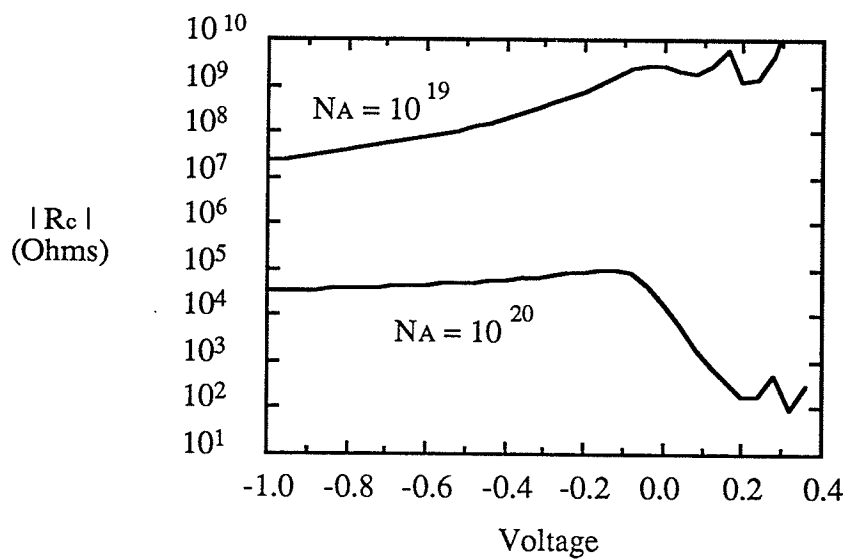


(b) Mo-p-Si contact

Figure 4.9: Current density vs. voltage characteristics of Mo-n-Si and Mo-p-Si contacts for field emission. Positive voltage is forward bias in both plots. Calculations were performed for a temperature of $T = 300$ °K.



(a) Mo-n-Si contact



(b) Mo-p-Si contact

Figure 4.10: Contact resistance vs. voltage characteristics for field emission, for a probe-surface contact radius of $a = 10$ nm. Positive voltage is forward bias in both plots. Calculations were performed for a temperature of $T = 300$ °K.

4.7 Space Charge Limited Conduction

Space charge limited (SCL) conduction is the limiting of current flow by the space charge in the semiconductor. SCL conduction operates as follows. If the injection of charge carriers is higher than the rate which the bulk semiconductor can accept the injected carriers, a space charge region (scr) will form at the interface which will block the injection of carriers. Thus, the current is controlled by the carrier mobility in the scr inside the semiconductor.

The equations governing SCL conduction between two concentric spherical electrodes of radii r_a and r_b (where $r_b \gg r_a$), separated by a semiconductor of thickness d (where $d = r_b - r_a$) are shown below [41]. These equations are valid for the case $r_b \gg r_a$. With the inner electrode as the injecting contact (ie. for operation in the reverse bias mode wrt electrode r_a), SCL conduction is governed by:

$$I = \frac{3\pi\epsilon\mu V^2}{2r_b} \quad (4.19)$$

where ϵ is the dielectric permittivity of the intervening semiconductor, μ is the mobility of charge carriers in the semiconductor, and V is the bias voltage. With the outer electrode as the injecting contact (ie. for operation in the forward bias mode wrt electrode r_a), SCL conduction is governed by:

$$I = \frac{3\pi\epsilon\mu V^2}{2r_b} \left(\frac{2r_a}{r_b}\right)^2 \quad (4.20)$$

A calculation of the SCL conduction current was performed using r_a as the radius of contact between the SCM probe and the sample, and with r_b taken to be twice the spreading resistance radius.⁶ This calculation showed that SCL conduction has little effect on the resistance R_c .

⁶ The spreading resistance radius is defined as the radius where 80 % of the potential drop between the probe and the sample due to spreading resistance occurs [2], [6]. This radius is equal to five times the probe-surface contact radius.

4.8 Conductance Measurements With The SCM

Having discussed the origins of the resistances R_{sp} and R_c in sections 4.3 through 4.7, we can now determine which of these two resistances dominates the total resistance R_T , given by equation (4.2). The equivalent circuit of the probe-surface contact is given in Figure 4.3, and is redrawn below:

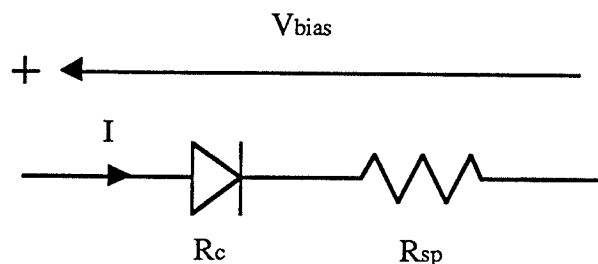


Figure 4.11: Equivalent circuit of the probe-surface interface. The total resistance is given by $R_T = R_c + R_{sp}$.

From the results of sections 4.3 through 4.7, we see that $R_c \gg R_{sp}$ for probe-to-surface potential differences of $V < \phi_b$. As V approaches ϕ_b , the potential barrier between the metal probe and the semiconductor sample collapses. The resistance R_c then becomes less dominant. At values of $V > \phi_b$, the current flow is dominated by the spreading resistance R_{sp} . Which of the two resistances is dominant, then depends on the potential difference between the SCM probe and the sample. This is illustrated in Figure 4.12 for the case of an ideal diode.

When making conductance measurements with the SCM, the probe to surface potential difference should be kept low in order to limit the current flow. High current flows would result in excessive heating of the probe-surface interface, and may result in ensuing damage to the SCM probe tip or the sample. However, the current flow should be sufficient so that it is significant in comparison to electrical noise present in measurements. Operation of the SCM will be discussed further in chapter 5 of this thesis.

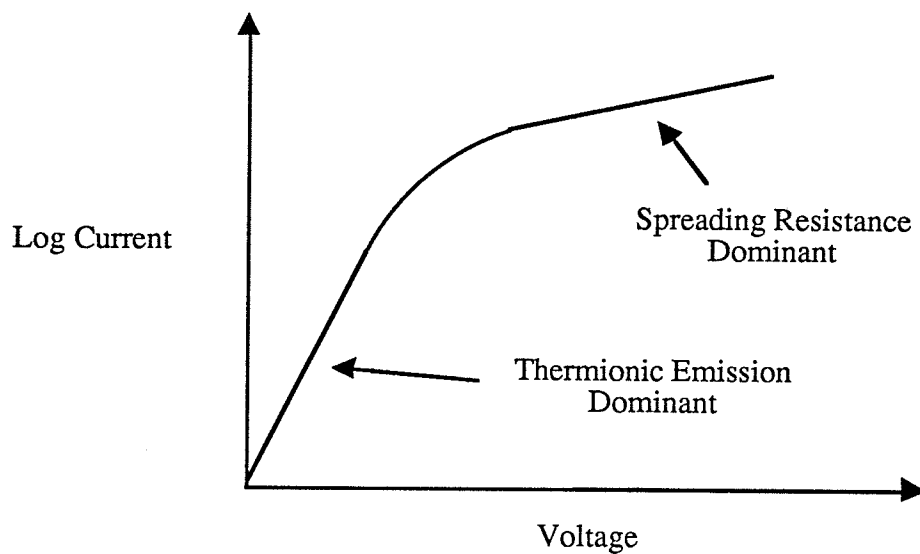


Figure 4.12: Current-voltage characteristic of an ideal diode. At low voltages, the current flow is governed by thermionic emission. At high voltages, the current flow is dominated by spreading resistance.

4.8.1 Detecting Changes In Dopant Concentration

The discussion of this section is related to the detection of changes in dopant concentration within a region of given dopant type (ie. n-type or p-type).

If the SCM probe is biased such that the spreading resistance R_{sp} is dominant, the current flow is inversely proportional to the resistivity, and thus to the dopant concentration of the sample (this was shown in section 4.3). Changes in dopant concentration can then be detected by monitoring changes in the current flow between the SCM probe and the sample under test.

If the SCM probe is biased such that the contact resistance R_c is dominant, the dependence of the current flow on dopant concentration will not be as obvious. For low doped semiconductors where the dominant current flow mechanism is thermionic emission (for $N_D \leq 10^{17} \text{ cm}^{-3}$), the current flow does not change with changes dopant

concentration. However, for highly doped samples where the dominant current flow mechanism is field emission (for $N_D \geq 10^{19} \text{ cm}^{-3}$), the current flow is exponentially dependant on $(N_D)^{-1/2}$.

Therefore, if R_c is dominant, relatively small changes in dopant concentration in low doped samples should not be detectable by the SCM. However, they may be detectable in highly doped samples. Furthermore, large changes in dopant concentration, which result in the switching of the dominant current flow mechanism between thermionic and field emission, should be detectable by the SCM.

4.8.2 Detecting Changes In Dopant Type

The discussion of this section is related to the detection of a change in dopant type (ie. from a p-type region to an n-type region, or visa versa).

If the SCM probe is biased such that the spreading resistance R_{sp} is dominant in both dopant type regions, the SCM would only be able to detect a change in dopant type, if there is a noticeable difference in the resistivity between the regions of different dopant type.

If the SCM probe is biased such that the contact resistance R_c is dominant, we must again consider the case of thermionic emission and field emission individually. In the case of thermionic emission, significant current flow only occurs when the probe-surface contact is forward biased. Thus, the probe bias can be selected such there will only be significant current flow over either the n-type or p-type regions of the sample. In the case of field emission, significant current flow occurs for both forward and reverse biased probe-surface contacts. Thus, the probe bias must be selected such that the probe-surface conductivity is higher over either the n-type or p-type regions of the sample.

4.8.3 An Example

In order to illustrate some of the ideas of sections 4.8.1 and 4.8.2, the expected conductance of the SCM probe-sample interface is calculated below as the probe is scanned across a p-n junction. This was done using the dopant concentration vs. position

characteristic of a p-n junction test sample. Actual conductance scans across this junction by the SCM are presented in section 5.3.

The dopant concentration vs. position characteristic of the p-n junction test sample is shown in Figure 4.13. From this figure we can see that the concentration of p-type dopant is approximately 10^{20} cm^{-3} near the surface of the sample, and that the concentration of n-type dopant is $3 \times 10^{15} \text{ cm}^{-3}$ in the bulk of the sample. A discussion as to how this sample was fabricated is given in section 5.2.

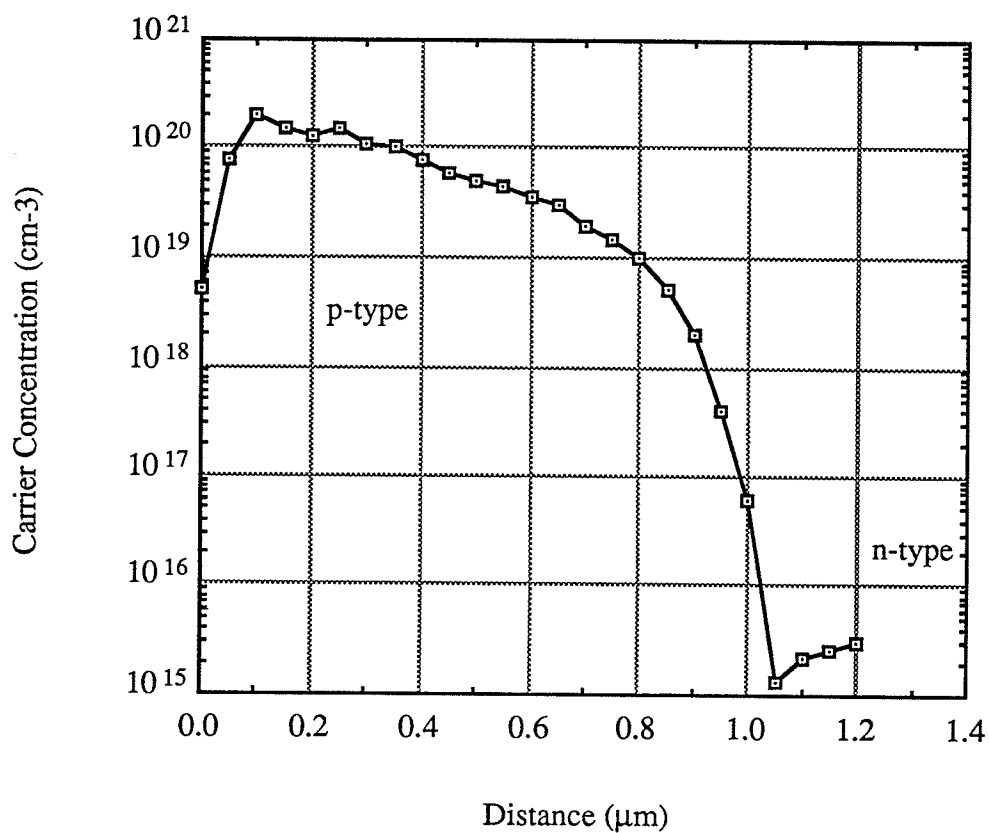


Figure 4.13: Doping concentration vs. position characteristic of test sample as measured by spreading resistance profile [47]. In this figure, 0.0 μm signifies the surface of the sample.

Using the information of figure 4.13, plots of the expected current density present at the probe-surface interface were calculated as a function of probe position. Calculations were performed assuming the contact resistance R_c was the dominant resistance. Thermionic emission (with the ideality factor $n=1$) and field emission were considered to be the only current flow mechanisms, and they were considered to be operating in parallel at a temperature of $T = 300$ °K. In addition, both the n-type and p-type regions of the sample were considered to be electrically grounded.

Figure 4.14 and 4.15 are plots of current density vs. probe bias voltage. Figure 4.14 shows results for positive probe bias voltage. Figure 4.15 show results for negative probe bias voltages. A positive biased probe results in a forward biased probe-surface contact over the n-type region, while a negative biased probe results in a forward biased contact over the p-type region. Data was calculated for probe-surface barrier heights of 0.45 eV over the p-type region and 0.67 eV over the n-type region. This is given by Sze in [37] to be a good W-Si contact.

Figure 4.14 shows three things. First, for probe bias voltages above 0.2 V, the n-type region is more conductive than the low doped p-type region. Second, the conduction of the highly doped p-type region is greater than that of the n-type region, even for a bias voltage of 0.6 volts. Third, the conduction in the highly doped p-type region depends greatly on doping.

Figure 4.15 shows three things. First, current flow exists primarily in the p-type region. Second, the conduction of the highly doped p-type region is greater than that of the lower doped p-type region. Third, the conduction in the highly doped p-type region depends greatly on doping and probe bias.

These results indicate to us several things. First, with an appropriate bias voltage on the SCM probe, it should be possible to distinguish between low doped n-type and p-type regions. Second, within a region of given dopant type, we should be able to distinguish between highly doped and lowly doped regions. Finally, within a highly doped region, the SCM should be able to resolve small changes in doping.

Figure 4.16 is a plot of current density vs. probe-sample barrier height. Barrier heights of 0.2 eV, 0.4 eV, 0.6 eV, and 0.8 eV were used in both the n-type and p-type regions. Data was calculated for a probe bias of 0.2 V.

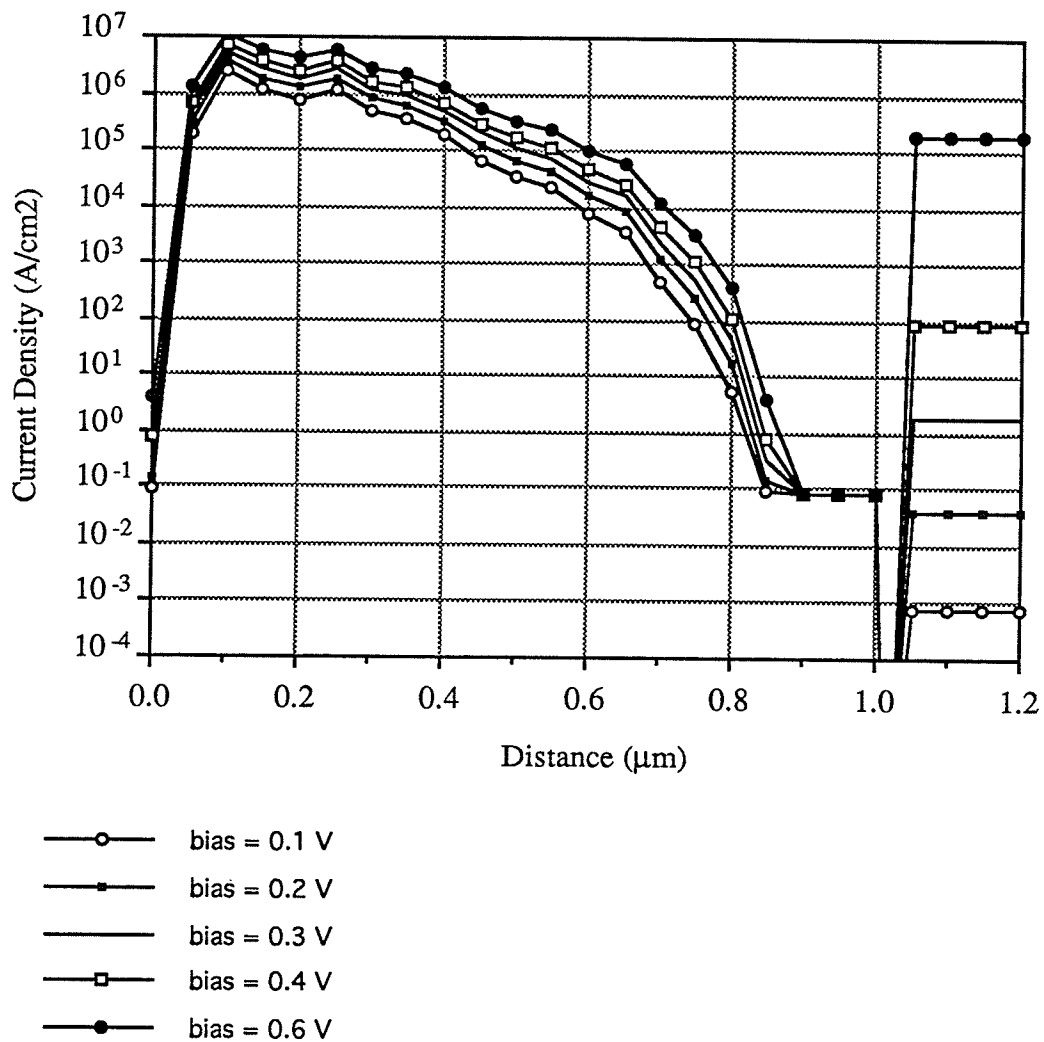


Figure 4.14: Plot of current density vs. positive probe bias voltage. Probe-surface barrier heights of 0.45 eV over the p-type region and 0.67 eV over the n-type region were used.

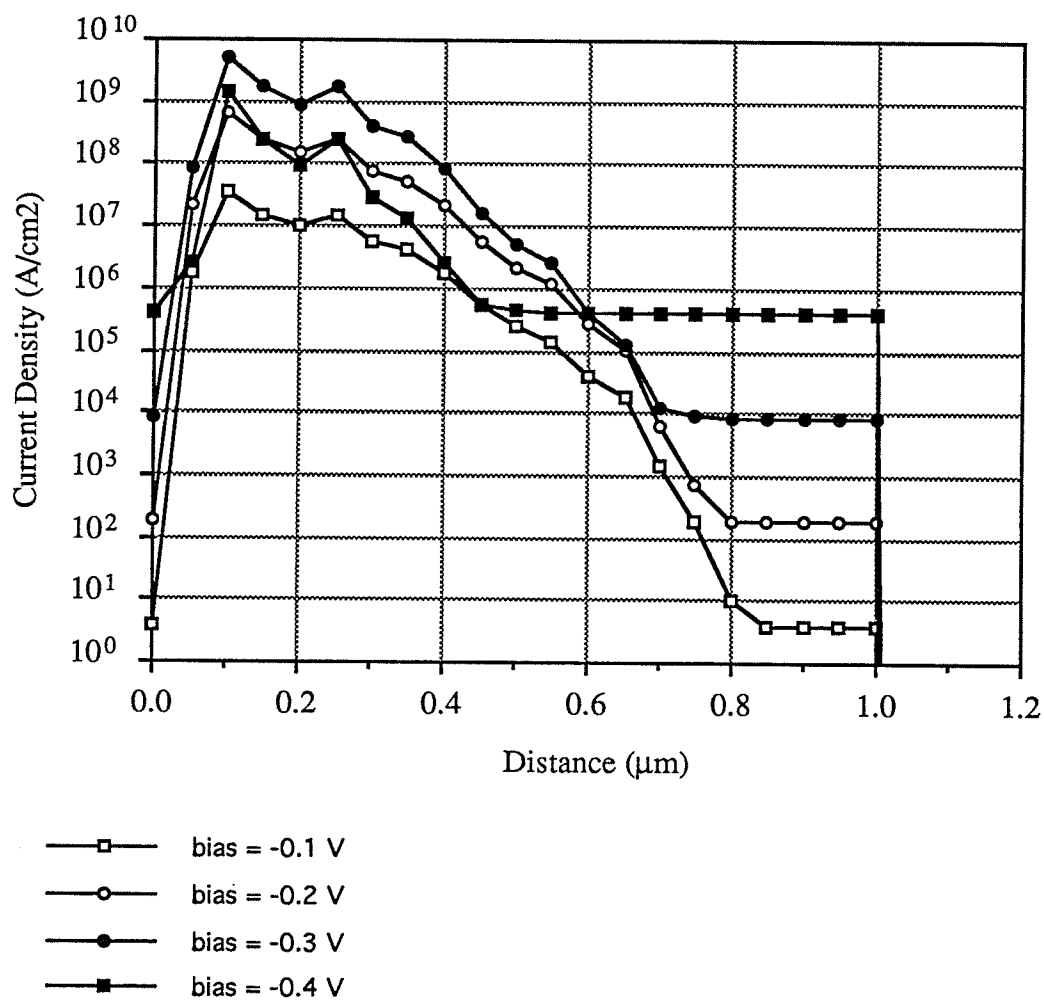


Figure 4.15: Plot of current density vs. negative probe bias voltage. Probe-surface barrier heights of 0.45 eV over the p-type region and 0.67 eV over the n-type region were used.

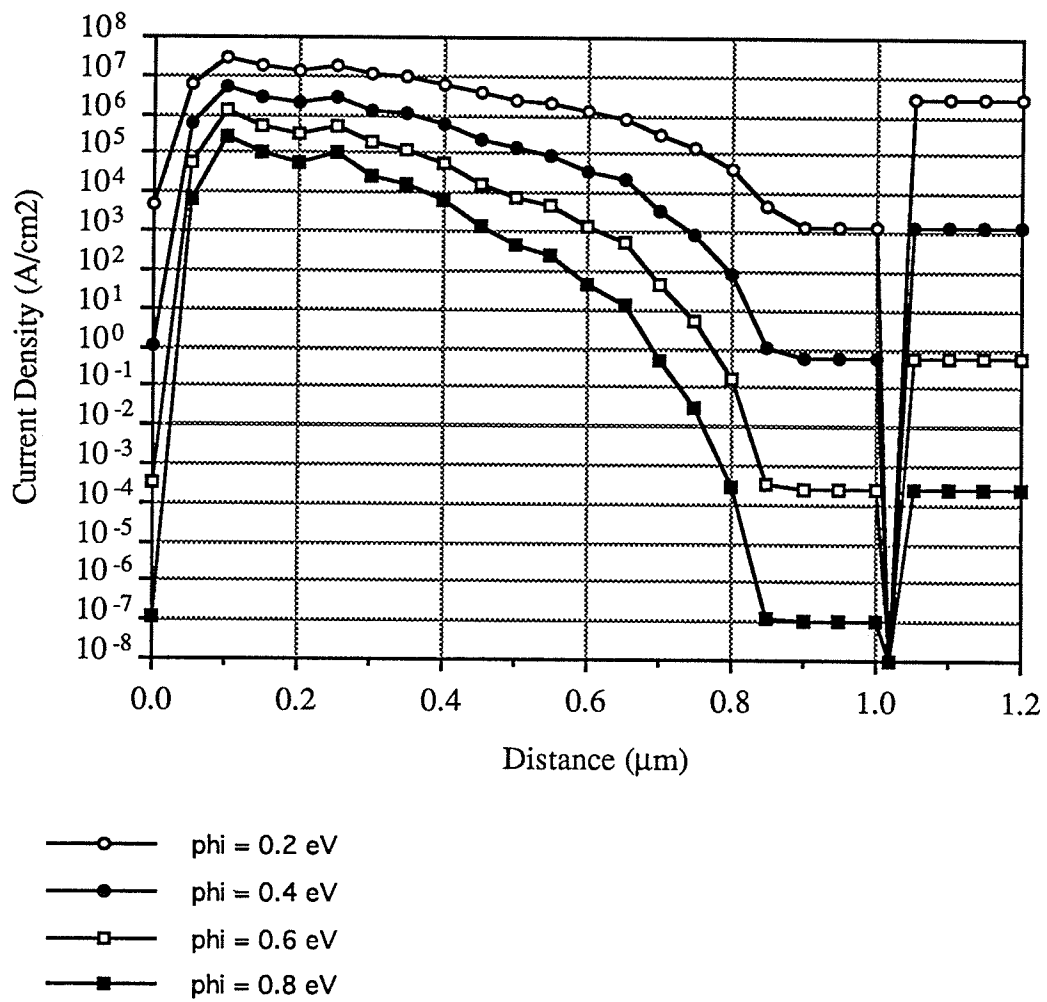


Figure 4.16: Plot of current density vs. probe-surface barrier height. The probe bias voltage is 0.2 V.

4.9 Crossing Over A Metallurgical Junction

When the SCM probe is scanned over a metallurgical junction between regions of different dopant types, it may observe much more than a difference in the conductance of the probe-surface contact. Because of the high spacial resolution of the SCM, it may be possible to observe the depletion region existing between regions of different dopant type.

S. Kordic et al. in [35] were able to detect the presence of the depletion region between a p-type and an n-type region on a cleaved silicon sample. They scanned over a p-n junction with a scanning tunneling microscope (STM), and found that the tunneling current dropped off over the depletion region. Furthermore, they found that they could vary the size of the depletion region by applying a bias across the p-n junction.

They also found that the presence of an appropriately biased STM probe was able to locally forward bias the the p-n junction. In this experiment, the STM probe was biased at a voltage less than the potential of the p-type side of the junction. When the probe was brought to the vicinity of the p-n junction from the n side of the junction, the difference in potential between the probe and the p side, resulted in the probe locally forward biasing the junction. Thus, the p-n junction in the vicinity of the STM tip injected strongly. The injected minority carriers decreased the value of the resistance of the material, so that a higher than normal tunneling current was possible.

This suggests that a spike in the conductance current measured by the SCM may be present in the vicinity of the depletion region. Whether the spike is on the p or n side of the p-n junction would depend on the bias voltage of the SCM probe.

4.9.1 Width Of The SCR Between P And N Doped Regions

The width of the space charge or depletion region between regions of different dopant types, is dependant on the dopant concentration of each region. The width of the depletion region is given by [37]:

$$W = \sqrt{\frac{2\epsilon}{q} \left(\frac{1}{N_A} + \frac{1}{N_D} \right) (V_{bi} - V)} \quad (4.21)$$

$$V_{bi} = \frac{kT}{q} \ln \left(\frac{N_A N_D}{n_i^2} \right) \quad (4.22)$$

where ϵ is the dielectric permittivity of the semiconductor, N_A is the dopant concentration of the p-type material, N_D is the dopant concentration of the n-type material, V_{bi} is the built in potential, and V is the potential difference across the depletion region (V is positive in forward bias). A more accurate result for the depletion width W is obtained by considering the Debye length (see section 4.10 below). For an abrupt p-n junction:

$$W = \sqrt{\frac{2\epsilon}{qN_B}(V_{bi} - V)} \quad (4.23)$$

where $N_B = N_D$ or N_A depending on whether $N_A \gg N_D$ or visa versa. For abrupt junctions with ultra-shallow depths, this equation may not be valid [37], [44].

4.10 Spatial Resolution Of The SCM

It was mentioned in chapter 3, that the contact size between the SCM probe and the sample plays a part in the spacial resolution of the SCM. A smaller mechanical contact should result in a higher spacial resolution. However, the electrical contact size between the probe and the sample should also be considered.

If the SCM was operated with probe bias voltages such that the dominant current flow mechanism was the spreading resistance (R_{sp}), the spacial resolution of the SCM would be influenced by the spreading resistance radius. About 80% of the total potential drop due to the spreading resistance occurs within a distance of about 5 times the electrical contact radius of the probe [2], [6].

If the SCM was operated with probe bias voltages such that the dominant current flow mechanism was the contact resistance (R_c), the spacial resolution of the SCM would be influenced by the width of the space charge region (scr) at the probe-surface interface. This width is defined by equations (4.8) and (4.9) in section 4.4.2. From these equations we see that the scr width is a function of semiconductor doping and probe bias voltage. Higher dopant concentrations or the application of a forward bias to the SCM probe will decrease the scr width. Lower dopant concentrations or the application of a reverse bias to the SCM probe will increase the scr width. This suggests that it may be possible to

vary the spacial resolution of the SCM by changing the probe bias voltage.

Equation (4.8) assumes that the width of the scr ends abruptly. However, in reality the width of the scr decays exponentially. In order to include this extension to the width of the scr, the term V_{bi} in equation (4.8) should be replaced by $(V_{bi} - 2kT/q)$, yielding [37], [43]:

$$W_{\text{planar}} = \sqrt{\frac{2\epsilon}{qN_B} \left(V_{bi} - \frac{2kT}{q} - V \right)} \quad (4.24)$$

The factor kT/q results from adding twice the Debye length to the low doped side of the abrupt junction. The Debye length (L_D) is given by:

$$L_D = \sqrt{\frac{\epsilon kT}{q^2 N_B}} \quad (4.25)$$

This length is small when compared to W_{planar} and is normally neglected. However, it is independent of the applied potential across the metal-semiconductor junction. Thus, when the SCM probe is biased such that the junction is in a forward bias condition, the Debye length becomes more predominant.

4.11 Conductance Microscopy: An Absolute Or Relative Technique?

SCM measurements are made with an electrochemically etched probe in an open air environment. It is then expected that the radius of curvature of the SCM probe tip will vary between etched probes, and that there will be the presence of surface contaminants or an oxide layer on the sample and probe surfaces. Therefore, the conductance measured with the SCM may vary with when different probes or samples are used.

Accurate and consistent results can be obtained with the SCM, if conductance measurements are made as relative measurements. This is done by calibrating the SCM probe against specimens of known resistivity. Of course this calibration is valid only when using the same probe, the same probe load, sample conductivity type, orientation, and preparation. These are essentially the same experimental procedures used to obtain reliable SR measurements.

Chapter 5

EXPERIMENTAL RESULTS

5.1 Experiment Preparation And Details

5.1.1 Preparing Samples

Before a sample can be analyzed with the SCM, it should be cleaned of surface oxide so that there is good electrical contact between the sample and the SCM probe. This was done using two methods. The first method involved cleaving the sample to provide a clean surface. The second method involved the removal of surface oxide by chemical etching. Samples studied in this thesis were silicon. The surface oxide was removed by using an HF etch, or a buffered oxide etch made from a 10:1 solution of Ammonium Fluoride and HF respectively. Etching was performed until it was deemed that the silicon sample was hydrophobic. Thus, indicating the removal of surface oxide.

SCM measurements are made in an open air environment. Thus, a native oxide layer is formed on the sample rapidly after etch or cleaving. This layer remains thin even after several hours of exposure to air. E. A. Taft showed in [46] that after 1000 minutes the oxide layer is only approximately 15 Å thick. Due to the thinness of this layer, it does not significantly hamper SCM measurements. Good results can be achieved with the SCM after several days of sample exposure to an air environment. This agrees with the results of [46].

5.1.2 Preparing Probes

SCM probes were etched before use. New probes were etched when new samples were used or when the quality of the conductance image degraded.

5.1.3 Ohmic Contact To Sample

Referring to sections 4.1 and 4.2 of this thesis, we see that a large area contact (with resistance R_g) must be made to the sample. This contact is used as the return path for the conductance current. This contact was made after sample etch, by fixing a wire to the sample with silver epoxy. The size of this contact was made as large as possible to minimize the contact resistance.

It is preferable that this contact be ohmic and that its resistance be negligible to that of the probe-surface contact (ie. the contact that we are interested in). The quality of this type of contact was tested on an n-type silicon sample doped to $3 \times 10^{15} \text{ cm}^{-3}$. The sample was first scratched with 600 grit emery paper, then contact wires were fixed to the scratched region with silver epoxy. The contacts were each approximately 2 - 3 mm in diameter, and were placed on the sample separated by a distance of approximately 2 mm (see Figure 5.1). The total resistance of this set up is:

$$R_T = 2R_g + R_{\text{Bulk}} \Omega \quad (5.1)$$

where R_g is the resistance between the sample and each contact, and R_{Bulk} is the resistance of the bulk semiconductor between the two contacts. R_{Bulk} is small in comparison to R_g , and so it can be neglected. Thus, R_g is equal to $R_T / 2$.

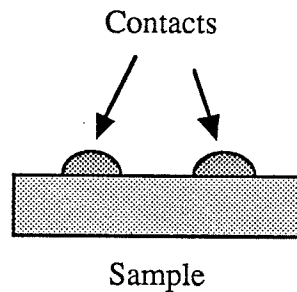


Figure 5.1: Ohmic contacts placed on sample.

An AC bias voltage was placed across the two contacts. The bias voltage was swept between ± 0.1 volt, and the current flowing between the contacts was measured. We can determine the contact resistance (for a given bias voltage) using equation 4.14, which is displayed again below.

$$R_c (V_{\text{bias}}) = \frac{\partial V}{\partial I} \Omega \quad (5.1)$$

A plot of the measured contact resistance is shown in Figure 5.2. This plot shows that the contacts are indeed ohmic in nature, and that the total resistance between the two contacts (R_T) is on the order of $10^6 \Omega$. Thus, R_g would be on the order of 500 k Ω .

The ohmic contacts used for SCM measurements presented in this thesis, had an area much greater than the area of the contacts of Figure 5.1. The resistance of these contacts would then be much less than 500 k Ω . This resistance is small enough so that it can be made negligible through the selection of an appropriate bias voltage for the SCM probe.

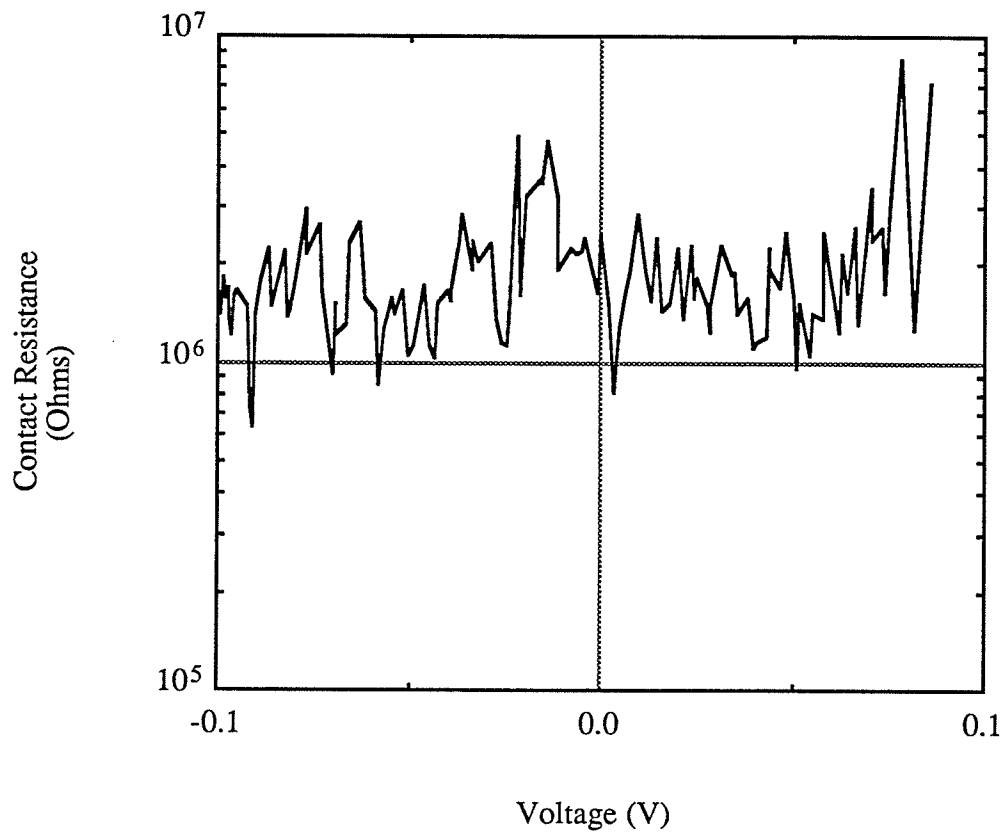


Figure 5.2: Resistance measured between the two contacts of Figure 5.1.

5.2 Current-Voltage Characteristic Of Probe-Surface Contact

As discussed in section 4.4.4, there are two forms of electrical conduction across a metal-semiconductor junction; thermionic emission, and field emission. Which mechanism is dominant depends on the doping concentration of the semiconductor. In low doped semiconductors, thermionic emission dominates. We then expect a significant current flow between the SCM probe and a sample when the probe-surface contact is forward biased. In the case of highly doped semiconductors, field emission is the dominant current flow mechanism. Thus, we expect significant current flow between the SCM probe and a sample for both forward and reverse biased probe-surface contacts.

The contact between the SCM probe and a sample was characterized by performing current-voltage (I-V) measurements over n-type and p-type regions of a semiconductor sample [48]. Both the n-type and p-type regions were electrically grounded for these measurements. The p-type region was boron doped by diffusion from a spin on glass source with thermal oxide used as a mask. Dopant concentrations of the n and p regions were $3 \times 10^{15} \text{ cm}^{-3}$ of phosphorus and 10^{20} cm^{-3} of boron respectively, as measured by spreading resistance profile [47]. Before the measurements were performed, the sample was etched in a buffered oxide etch to remove surface oxide.

Multiple I-V measurements were performed for three molybdenum probes and three tungsten probes. The measurements were performed with the SCM probe held stationary over each region during the voltage sweep. Furthermore, these measurements were performed in darkness, in order to minimize carrier generation due to illumination by room lights. Results of these current-voltage measurements are shown in Figures 5.3 to 5.6. Further results are presented in Appendix A. A discussion of these measurements is given in section 5.2.1.

It should be noted that for these measurements, AFM control of the probe-surface contact force was not used.

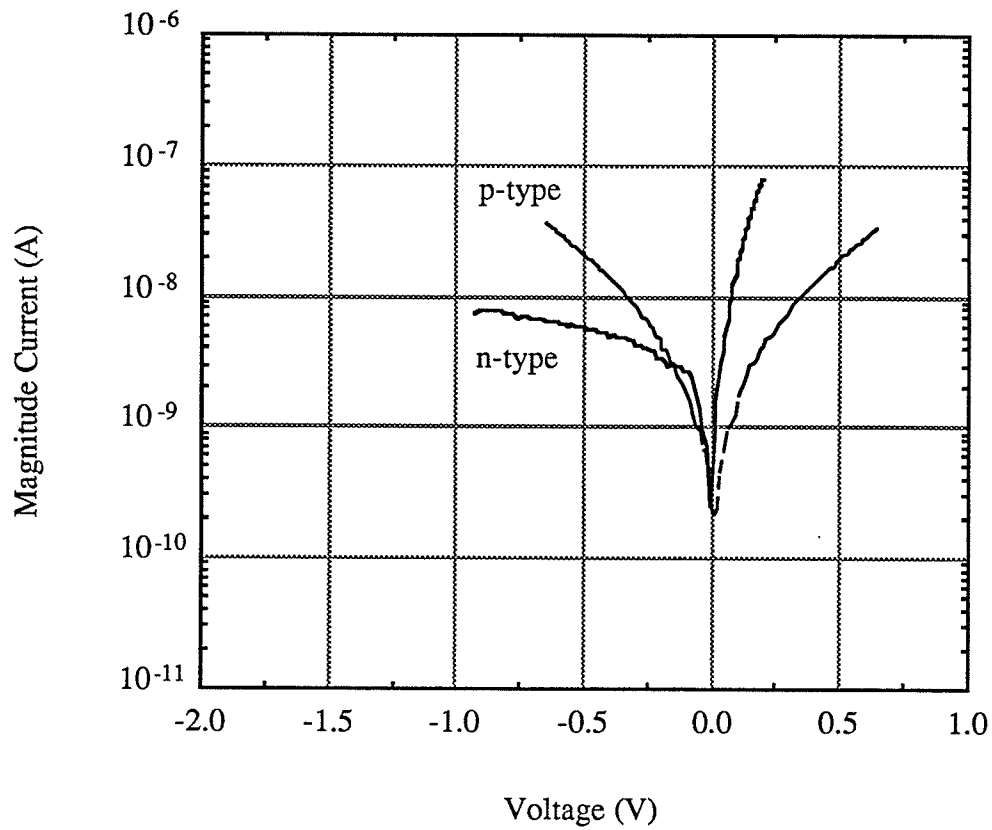


Figure 5.3: I-V measurements performed with tungsten probe[#] 1. In this plot we see that significant conduction current is present over the n-type region for positive probe bias voltages, and is present for both positive and negative bias voltages over the highly doped p-type region.

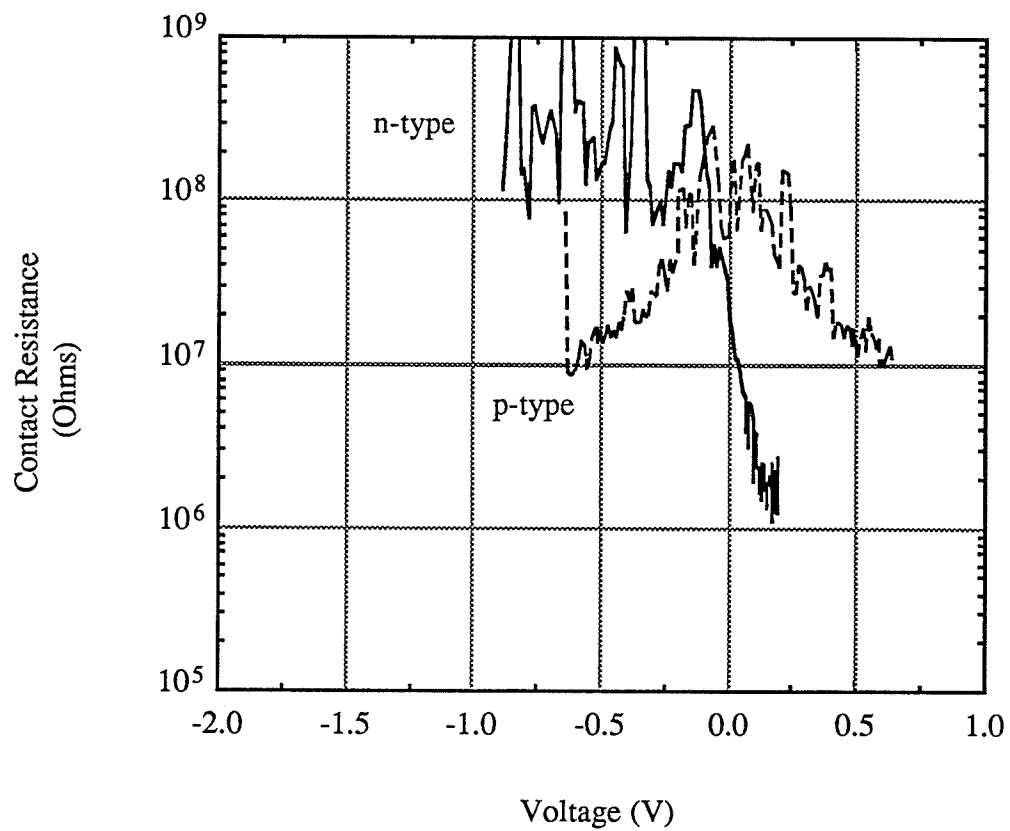


Figure 5.4: Contact resistance of I-V characteristics shown in Figure 5.3. In this plot we see that for high forward bias voltages, the differential resistance of the probe-surface contact over the n-type region, approaches a value close to the spreading resistance of the contact.

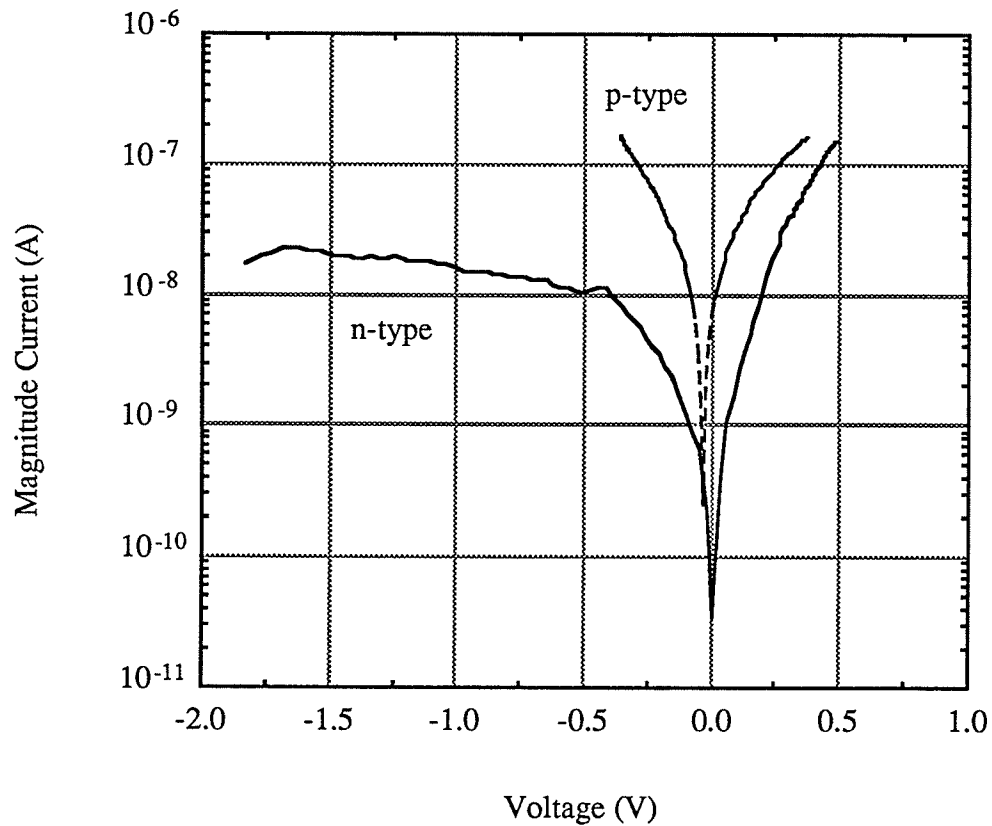


Figure 5.5: I-V measurements performed with tungsten probe[#] 3. In this plot we see that significant conduction current is present over the n-type region for positive probe bias voltages, and is present for both positive and negative bias voltages over the highly doped p-type region.

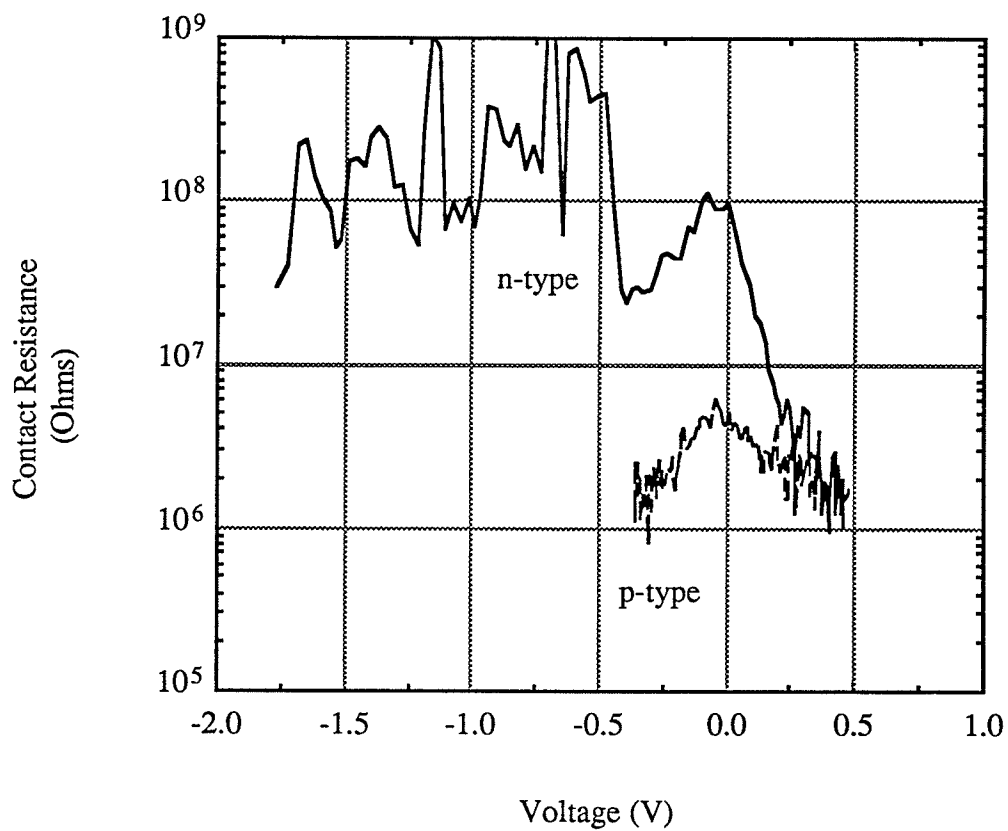


Figure 5.6: Contact resistance of I-V characteristics shown in Figure 5.5. In this plot we see that for high forward bias voltages, the differential resistance of the probe-surface contact over the n-type region, approaches a value close to the spreading resistance of the contact.

5.2.1 Discussion Of Current-Voltage Data

From the I-V spectra of Figures 5.3 and 5.5, it is apparent that the probe-surface contact over the low doped n-type region is Schottky like, with significant current conduction with a forward biased probe-surface contact (This corresponds to a positive bias of the SCM probe). Over the highly doped p-type region, significant current flow occurs for both forward and reverse biased probe-surface contacts. This agrees with what is expected of field emission current transport.

These results tell us two important things. First, for low doped semiconductors we should be able to distinguish between p-type and n-type regions by the presence of significant current flow. Significant current flow will only occur when the probe-surface junction is forward biased. When the SCM probe is operated at a constant bias voltage, this can be made to occur over n-type or p-type regions depending on the probe bias voltage. Second, regions of high dopant concentration can be located by the presence of current flow for both forward and reverse biased probe-surface contacts.

We can see from Figures 5.4 and 5.6, that for high forward bias voltages, the differential resistance of the probe-surface contact over the n-type region, approaches a value close to the spreading resistance of the contact (see Table 4.1). We also see that the contact over the highly doped p-type region exhibits more ohmic characteristics.

Figures 5.3 to 5.6, and the figures of Appendix A, show variations in the measured I-V characteristics between different probes and measurements. Variations may be due to different probe tip radii after etching, non-constant probe-surface contact force between measurements, or to the presence of contaminants at the probe-surface interface. Variations due to non-constant probe-surface contact force can be minimized by using AFM control of the probe-surface contact force (This was not done in these measurements).

Future work should be done in order to study the probe-surface contact characteristics further. Studies should be done for different probe etchant schemes, and over regions of different dopant concentrations.

5.3 One Dimensional Conductance Profiling

As a test of the SCM's profiling ability, one dimensional conductance profiles were performed by scanning the SCM probe across a cleaved p-n junction. An analysis of these conductance measurements will be discussed in this section, and will be compared to the known dopant profile of the p-n junction. The dopant profile of the sample, along with a theoretical analysis of the expected conductance profile as measured by the SCM, was shown previously in section 4.8.3. For a discussion of how this sample was fabricated, refer to section 5.2.

SCM conductance profiles of this p-n junction were performed as follows. First, the sample was cleaved in depth to expose the p-n junction. Second, the sample was oriented as shown in Figure 5.7. Third, an ohmic contact was made to both the n-type and p-type regions of the sample. Fourth, the sample was scanned beneath the SCM probe, such that the probe travelled from the n-type region toward the p-type region, and finally over the edge of sample. Thus, a conductance profile across the n-type region, across the p-n junction, and across the p-type region was obtained.

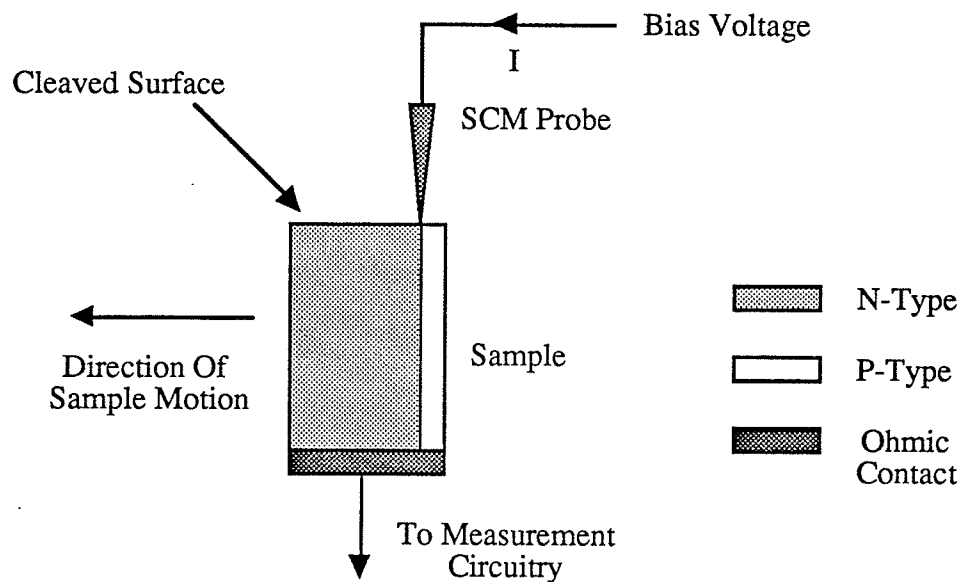


Figure 5.7: Experimental setup used to profile p-n junction.

While conductance measurements were taking place, the AFM was used to control the probe-surface contact force. In doing so, it was able to simultaneously obtain a topographical profile of the sample. This topographical profile is used to locate the edge of the sample in the conductance image. By knowing of the location of the sample edge, the conductance profile measured by the SCM can be compared to the dopant profile of the p-n junction.

It should be noted that these conductance measurements were performed in low light conditions, in order to minimize carrier generation due to illumination by room lights.

Figure 5.8 shows the result of a conductance profile taken with a molybdenum SCM probe biased to 0.2 volts. The width of this profile is $4.3 \pm 0.2 \mu\text{m}$.¹ This profile was performed several hours after the sample was cleaved, and with the SCM probe travelling across the junction with a velocity of $96 \mu\text{m}$ per second.² This figure has two traces in it; a thin trace and a thick trace. The thin trace represents the current flowing between the SCM probe and the sample. The thick trace is the simultaneous topographical profile obtained by the AFM.

Looking at Figure 5.8, we see that the measured current flow changes with the position of the SCM probe. In order to relate the current flow information to the dopant profile of the sample, we must locate the edge of the sample in the AFM topographical profile.

Figure 5.9a shows an AFM topographical profile of a hypothetical sample. The dashed line in this figure represents the sample surface as measured by the SCM probe tip. The edge of the sample can be located by drawing lines parallel to the topographical profile (see Figure 5.9b).³ The intersection of these lines is the located sample edge. This technique will locate the sample edge to within some fraction of the radius of curvature of the SCM probe tip.

¹ The uncertainty in the width of this profile, is due to possible error in the angular positioning of the sample with respect to the scan direction of the AFM's piezoelectric scanner.

² This corresponds to a scan frequency of 10 Hz on the AFM controller, with an angular scan angle of 64 degrees.

³ In Figure 5.9b, the parallel lines were offset slightly for illustrative purposes. In an actual measurement, these lines should overlap those of the AFM topographical profile.

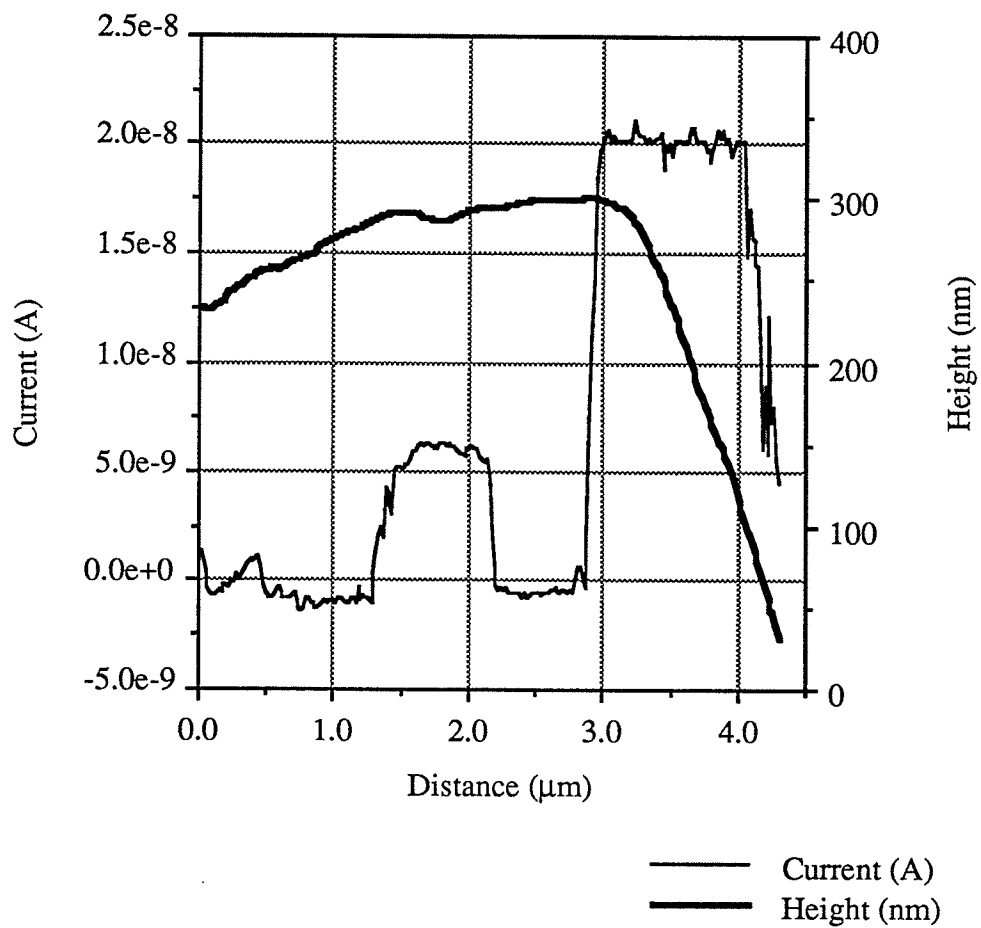
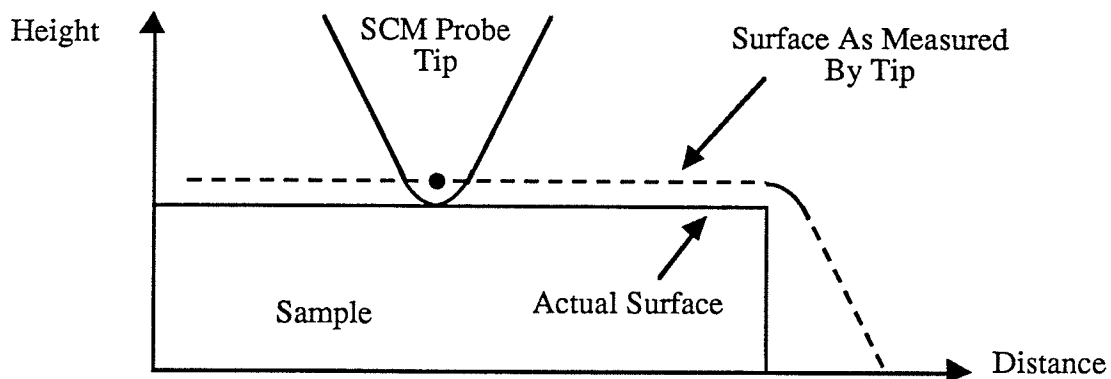
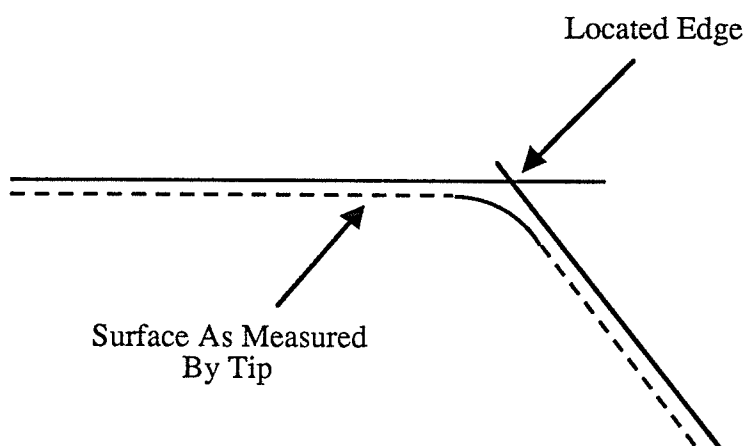


Figure 5.8: Conductance profile taken with a molybdenum SCM probe biased to 0.2 volts.



(a)



(b)

Figure 5.9: Determination of sample edge from AFM topographical profile.

(a) An AFM topographical profile of a hypothetical sample. The dashed line in this figure represents the sample surface as measured by the SCM probe tip.

(b) The edge of the sample can be located by drawing lines parallel to the topographical profile.⁴ The intersection of these lines is the located sample edge. This technique will locate the sample edge to within some fraction of the radius of curvature of the SCM probe tip.

⁴ In Figure 5.9b, the parallel lines were offset slightly for illustrative purposes. In an actual measurement, these lines should overlap those of the AFM topographical profile.

5.3.1 Analysis Of Figure 5.8

With the edge of the sample located from the topographical profile of Figure 5.8, we can offset the distance axis of Figure 5.8, such that the sample edge is located at 0.0 μm . This new profile is shown in Figure 5.10. In this figure the current flow data has been converted to conductivity information, with units of Amps/Volt. An expanded view of the region between -1.5 and 0.5 μm is shown in Figure 5.11. Analysis of these figures reveals the following.

Before reading the following analysis, readers are reminded that the measured distances are not exact. They are accurate to some fraction of the radius of curvature of the probe tip, and may be in slight error due to the angular positioning of the sample with respect to the scan direction of the AFM's piezoelectric scanner.

- Between -3.0 and -1.9 μm the measured conductivity is quite low, less than 10^{-8} A/V. It can be seen that this corresponds to a low region of the sample surface as shown in the topographical profile. The low measured conductivity may be due to the SCM probe not having good electrical contact with the sample in this region.
- Between -1.9 and -1.05 μm the measured conductivity is high, approximately 4×10^{-8} A/V. Referring to the doping profile of the sample (shown in Figure 4.13), this region corresponds to the n-type region of the sample.
- Between -1.05 and -1.0 μm the conductivity drops. This is then assumed to be the location of the metallurgical junction between the n-type and p-type regions. This is in close agreement with the doping profile of the sample.
- Between -1.0 and -0.35 μm the conductivity is low, less than 4×10^{-9} A/V. Referring to the doping profile of the sample, we see that this region corresponds to the p-type region doped to a concentration of less than 10^{20} cm^{-3} .
- Between -0.35 and 0.0 μm the conductivity is very high. This corresponds to the highly doped p-type region of the sample. The conductivity is approximately 10^{-5} A/V, which corresponds to a resistance of 100 K Ω . This is close to the resistance of the ohmic contact to the sample, as was shown in section 5.2.

- Beyond $0.0\ \mu\text{m}$ the conductivity remains high. This is because even after the SCM probe tip has passed over the sample edge, the side of the probe remains in contact with the sample edge and the highly doped p-type region.

Comparison With Theory:

What this analysis reveals to us is the following. A positive biased SCM probe resulted in a forward bias of the probe-surface junction when the probe was over the n-type region of the sample. When over the low doped p-type region, the probe-surface junction was reverse biased. This shows that the SCM is able to distinguish between low doped n-type and p-type regions. When the SCM probe was over the highly doped p-type region, significant current flowed. This shows that within a region of given dopant type, the SCM is able to distinguish between low doped and highly doped regions.

These results are in agreement with the theoretical discussions of section 4.8.

5.3.2 Negative Biased SCM Probe

Conductivity profiles of the p-n junction, with the SCM probe biased to $-0.2\ \text{V}$, are shown in Figures 5.12 and 5.13. In these profiles we can see the following.

- The SCM probe is in reverse bias over the n-type region of the sample, and in forward bias over the p-type region of the sample.
- The location of the metallurgical junction in this profile is in close agreement with the dopant profile of the sample, and with profile taken with the forward biased probe.
- The conductivity of the p-type region between -0.6 and $0.0\ \mu\text{m}$, is greater than that of the p-type region between -1.0 and $-0.6\ \mu\text{m}$. This may be due to increasing dopant concentration in the p-type region.

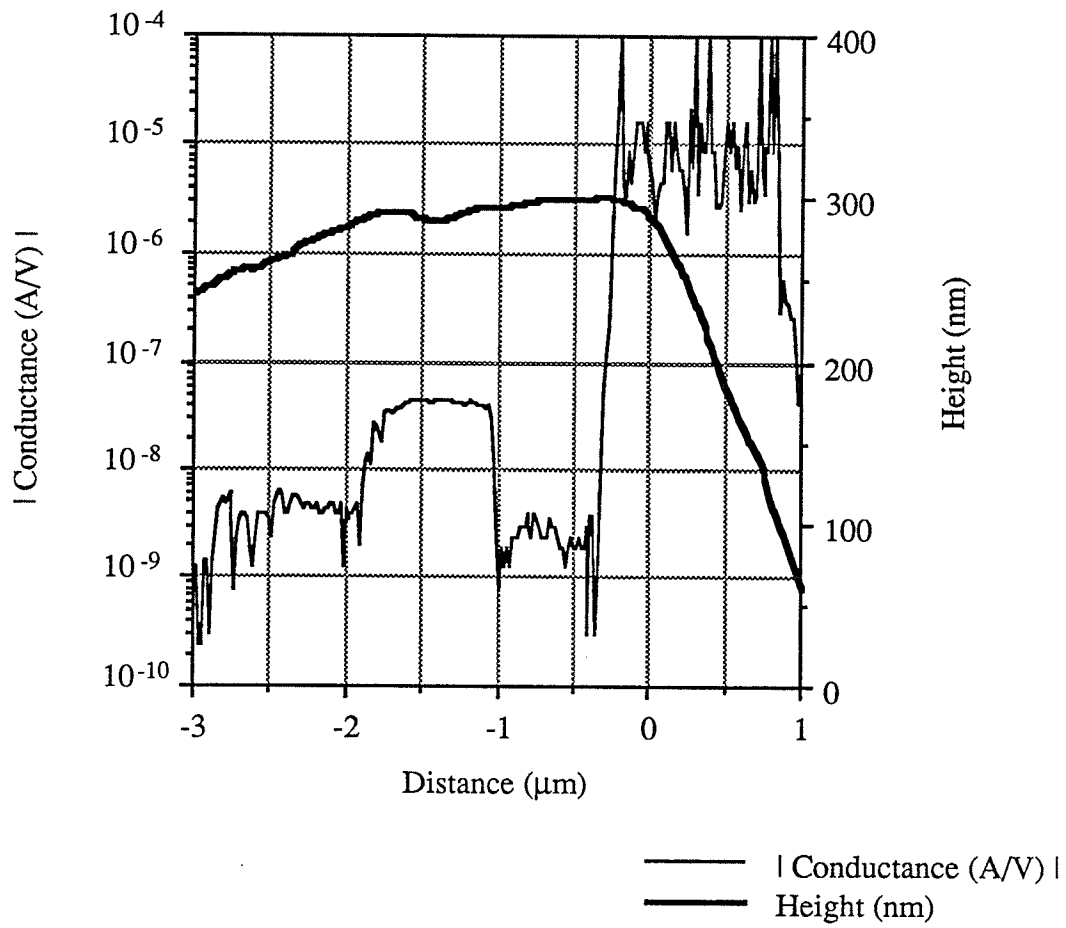


Figure 5.10: Conductance profile of p-n junction shown in Figure 5.8 with sample edge labeled as $0.0 \mu\text{m}$.

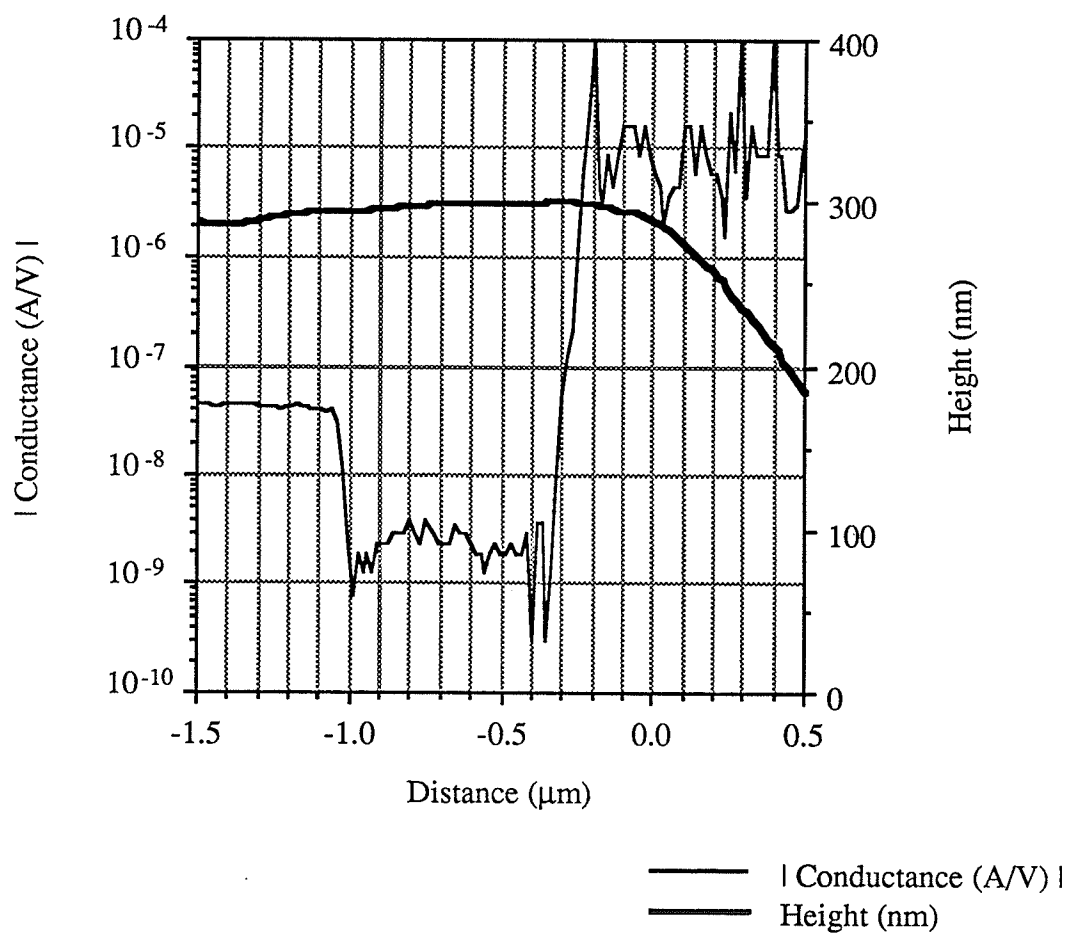


Figure 5.11: Expanded view of Figure 5.10.

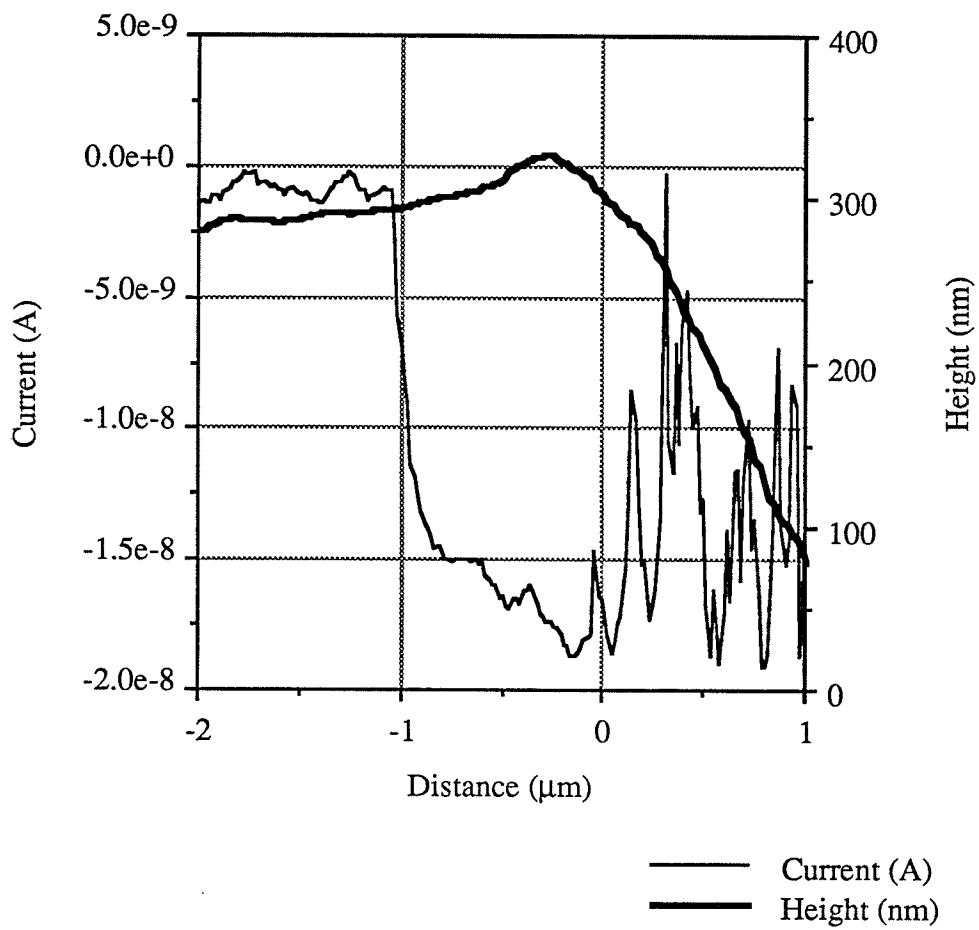


Figure 5.12: Current profile of p-n junction taken with a molybdenum SCM probe biased to -0.2 V.

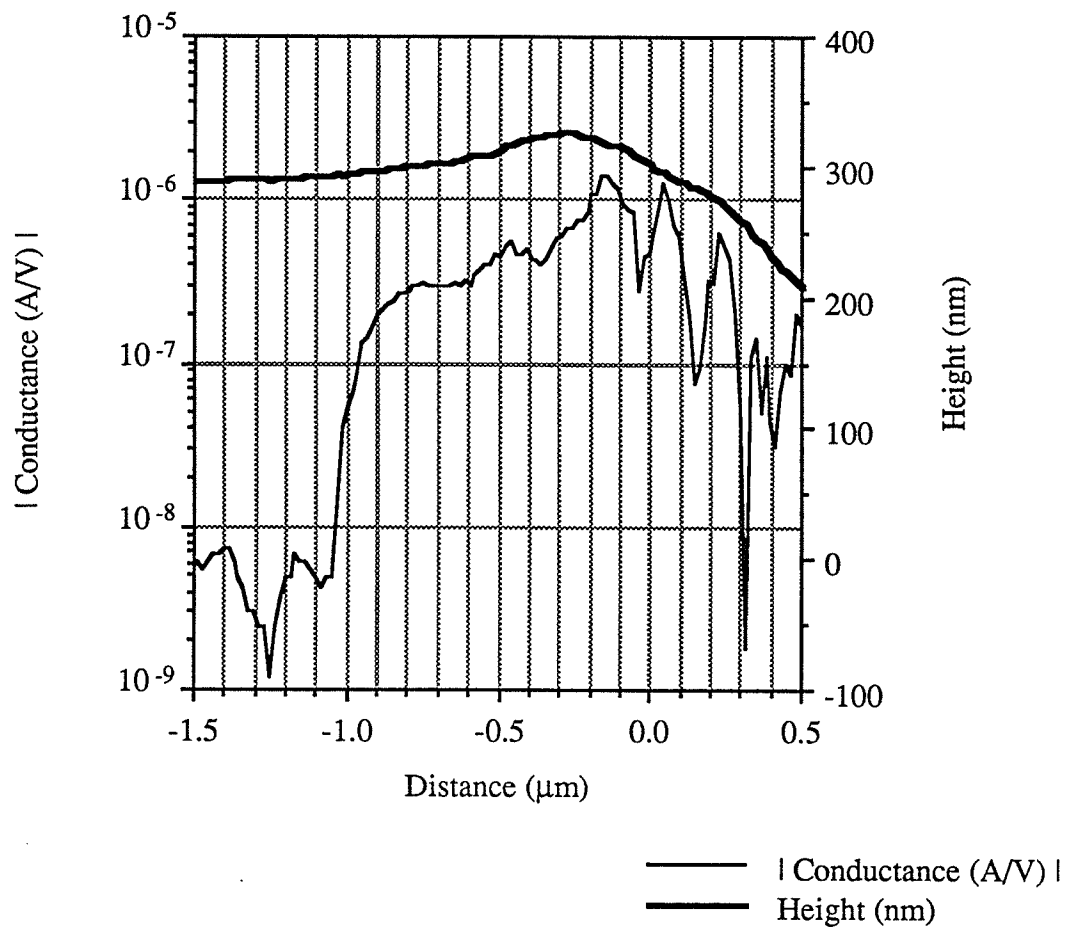


Figure 5.13: Expanded view of Figure 5.12. This plot shows the associated conductivity related to the current flow shown in Figure 5.12.

5.3.3 Conductivity Profile With A Tungsten Probe

Twelve days after the p-n junction sample was cleaved, conductivity profiles were again performed using a tungsten SCM probe. Figures 5.14 and 5.15 show the result of a conductance profile taken with the SCM probe biased to 0.2 V. Figure 5.14 shows the current flow measured by the SCM, and Figure 5.15 shows the associated conductivity. The profile measures $2.0 \pm 0.25 \mu\text{m}$ in width, and was taken with the AFM controller set to a scan speed of 5 Hz. The large uncertainty in the width of this scan, is due to difficulty in the angular positioning of the sample with respect to the scan direction of the AFM's piezoelectric scanner. Because of this large uncertainty measurements take from Figures 5.14 and 5.15 may be in error by up to 13 %. Analysis of these profiles reveals the following.

- Between -1.5 and $-1.1 \mu\text{m}$ the measured conductivity is high, approximately 3×10^{-8} A/V. Referring to the doping profile of the sample (shown in Figure 4.13), this region corresponds to the n-type region of the sample.
- The metallurgical junction appears to be located at a distance of $1.1 \mu\text{m}$ from the sample surface. This is in close agreement with the doping profile of the sample.
- Between -1.1 and $-0.3 \mu\text{m}$ the conductivity is low, less than 4×10^{-9} A/V. Referring to the doping profile of the sample, we see that this region corresponds to the p-type region doped to a concentration of less than 10^{20}cm^{-3} .
- Between -0.3 and $0.0 \mu\text{m}$ the conductivity is very high. This corresponds to the highly doped p-type region of the sample. The conductivity here appears to be limited by the ohmic contact to the sample, as was shown in section 5.2.

These results are in close agreement with the profiles taken with the molybdenum probe, and to the doping profile of the sample.

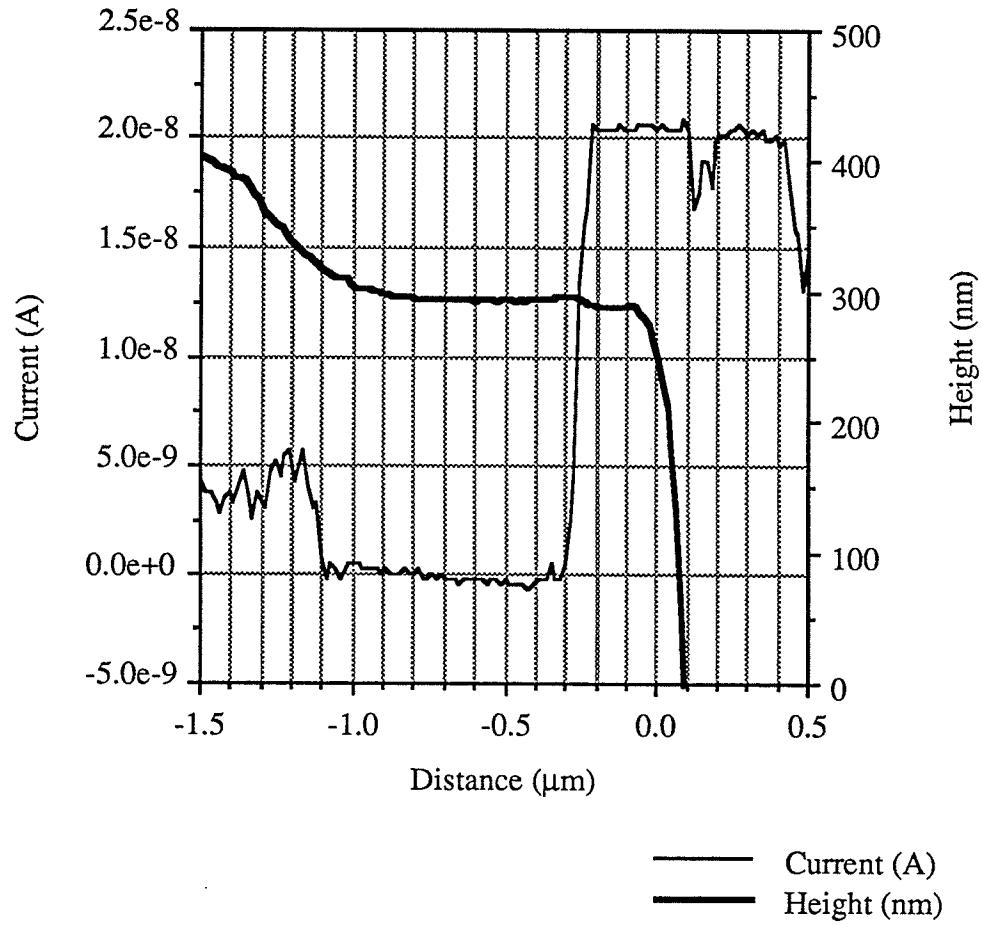


Figure 5.14: Current profile of p-n junction taken with a tungsten SCM probe biased to 0.2 volts.

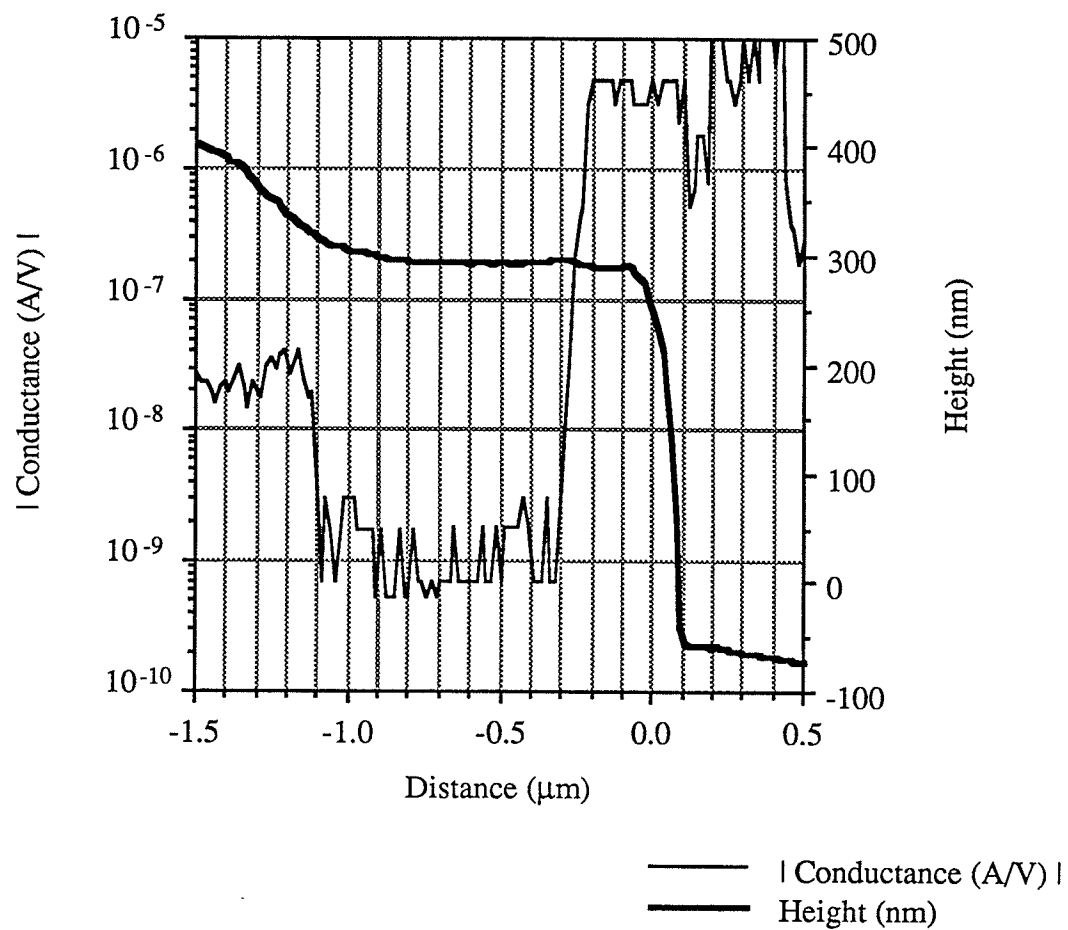


Figure 5.15: Conductance profile related to the current flow shown in Figure 5.14.

5.3.4 Dual-Bias Conductivity Profile

The data acquisition software on the PC is capable of sending two different bias voltages to the SCM probe on alternate scans. Thus, the probe can scan across the surface with one bias voltage, then on a subsequent scan it will scan across the surface with a different bias voltage. However, topographical data obtained by the AFM cannot be recorded in this mode of operation. Thus, the position of the sample edge cannot be identified. However, an rough idea as to the position of the sample edge can be inferred from the current measurements.

A dual bias scan was performed across the p-n junction, with a tungsten SCM probe scanning across the surface first with a bias voltage of 0.2 V, then with a bias voltage of -0.3 V. The current flow recorded in this scan is shown in Figure 5.16. The thin trace is the positive bias voltage scan. The thick trace is the negative bias voltage scan. The possible location of the metallurgical junction is indicated. It should be noted, that this measurement was performed twelve days after the sample was cleaved.

In Figure 5.16 we can see the following. The n-type region is forward biased for positive bias voltage. The highly doped p-type region conducts for both positive and negative probe bias voltages. However, for both positive and negative bias voltages, the low doped p-type region does not conduct significantly.

In an effort to see if this lack of conduction was due to this particular SCM probe or the sample, conductivity scans were performed with a different tungsten probe and with three different molybdenum probes. None of these probes could be made to conduct over the low doped p-type region, even with bias voltages as high as -1.0 V. Thus, this lack of conduction was attributed to surface contamination or oxide accumulation in the twelve days since the sample was cleaved.

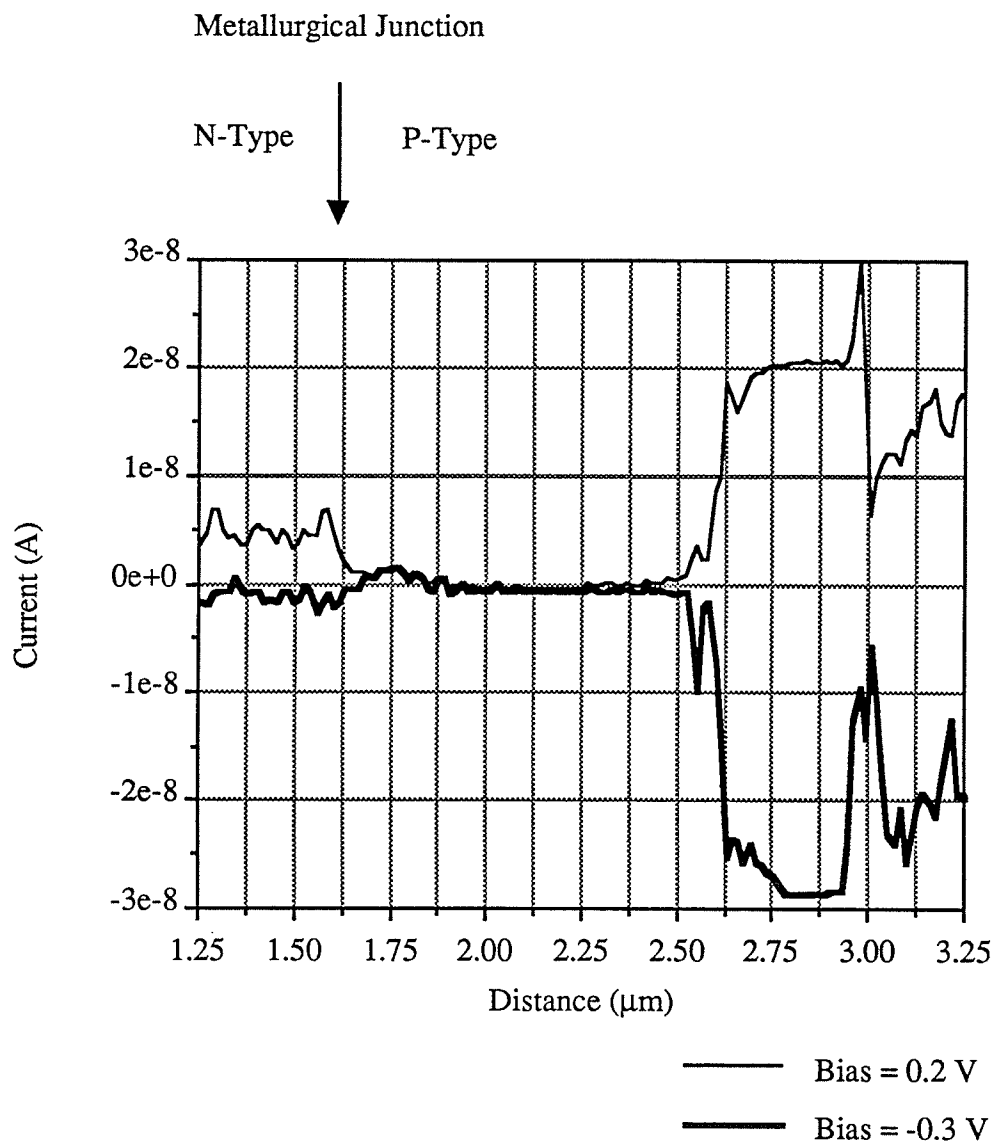


Figure 5.16: Dual bias scan across the p-n junction performed with a tungsten SCM probe.

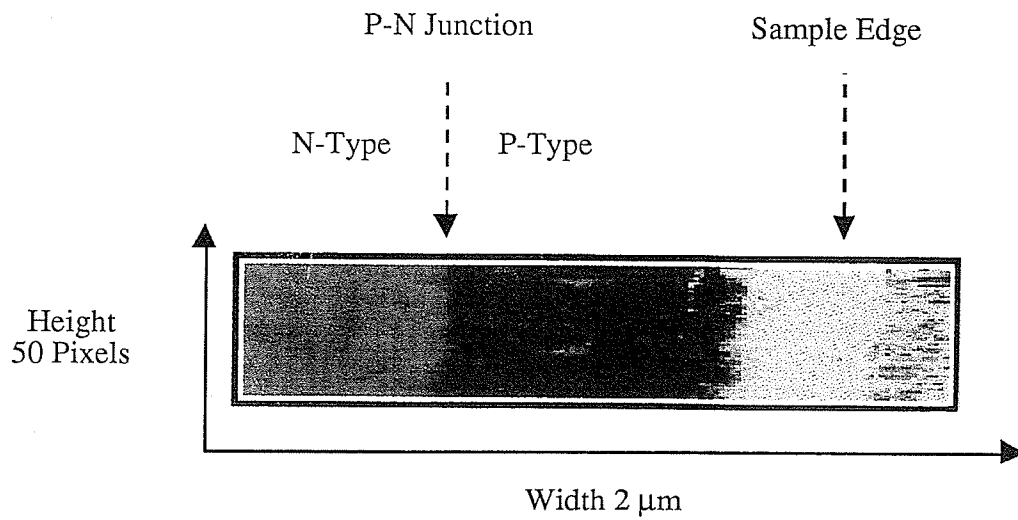
5.3.5 Grayscale Display Of Conductance Profiles

The data acquisition software on the PC is able to display the conductance information in the form of a grayscale image. In this format, the electric current flow between the SCM probe and the sample is represented by grayscale shading. White signifies regions of high current flow and so high probe-surface conductance. Black signifies regions of low current flow and so low probe-surface conductance.

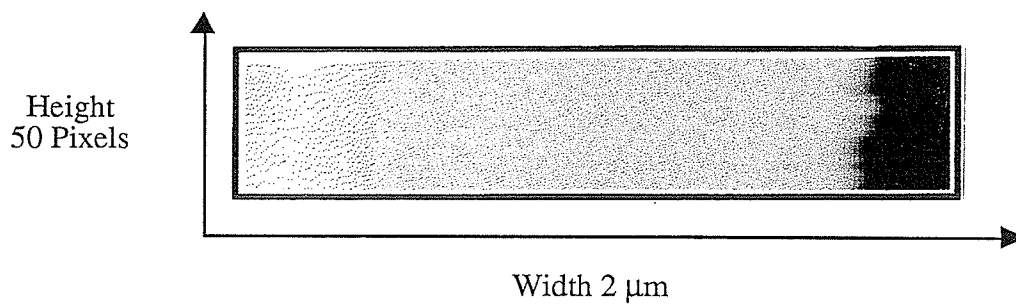
The PC is also able to display the topographical information obtained by the AFM in the form of a grayscale image. In this case, vertical height is represented by a grayscale. White signifies high surface features, and black signifies low surface features.

As an example, the current flow measured by the SCM during 50 consecutive conductance profiles (taken with a tungsten SCM probe biased to 0.2 V) is displayed as a grayscale in Figure 5.17a. Figure 5.17b displays a grayscale of the topographical information obtained by the AFM during the conductance measurement. These figures measure 2 μm in width and are 50 pixels high. Each pixel of height represents a single scan by the SCM probe across the p-n junction. Thus, each figure contains information of 50 consecutive scans across the p-n junction by the SCM probe. The close agreement between each of these scans, is an indication of the repeatability of the SCM technique. These scans were performed at a scan frequency of 5 Hz.

Labeled in Figure 5.17a is the located P-N junction, and the edge of the sample as found from the topography scan of Figure 5.17b.



(a)



(b)

Figure 5.17: SCM and AFM measurements across a p-n junction taken with a tungsten SCM probe biased to 0.2 volts. (a) A grayscale image of the current flow measured by SCM. (b) A grayscale image of the topography measured by the AFM during the SCM scan.

5.4 Two Dimensional Conductance Profiling

This section will present the results of lateral two dimensional conductance profiles over the surface of test samples. It should be noted that all of these measurements were performed without AFM control of the probe-surface contact force.

5.4.1 Imaging P-Doped Dots

The sample and the experimental setup is shown in Figure 5.18. The sample is a p-type substrate which is covered with an implanted n-type layer [49]. Dots, 1 μm in diameter, were masked during n-type implantation. Thus, they remain p-doped. An ohmic contact, acting as the return path for the conductance current, was placed on the p-type substrate. Before SCM measurements were performed, the sample was etched in HF to remove surface oxide.

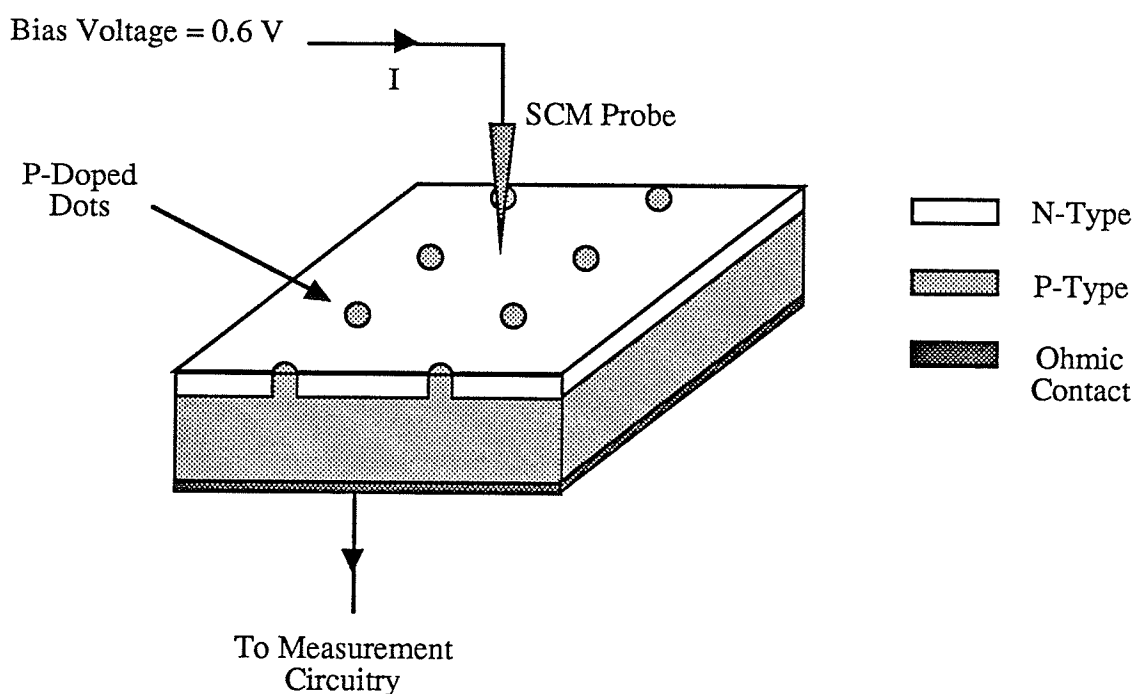


Figure 5.18: Experimental setup used to locate p-type dots on an n-type surface.

A theoretical analysis of what the expected current flow would be for a positive biased and a negative biased SCM probe is given below.

Positive Biased Probe:

When the SCM probe is over an n-type region, we would expect the probe-surface contact to be forward biased. However, the underlying n-type to p-type junction would be reverse biased. Thus, we would expect little current flow. When the probe is over a p-type dot, the probe-surface contact would be reverse biased. Thus, we would again expect little current flow. However, we may be able to distinguish between n-type and p-type regions, if the reverse saturation currents of the P-N junction and of the probe to p-type-surface junction differ.

Negative Biased Probe:

When a negative biased SCM probe is over an n-type region, the probe-surface contact would be reverse biased. Thus, we would expect little current flow. When the probe is over a p-type dot, the probe-surface contact would be forward biased. Thus, we would expect significant current flow.

SCM Conductivity Profile:

The theoretical analysis suggests that a negative biased SCM probe should be used to image the dots. However, the analysis also suggests that the dots may be imaged by a positive bias. A positive bias was used and the two dimensional current flow image is shown in Figure 5.19.

The scan of Figure 5.19 measures $7.2 \mu\text{m} \times 7.2 \mu\text{m}$ in size, and was obtained with a molybdenum SCM probe biased to 0.6 V. In this image, the electric current flow between the SCM probe and the sample is represented by grayscale shading. White signifies regions of high current flow and so high probe-surface conductance. Black signifies regions of low current flow and so low probe-surface conductance. Figure 5.19 clearly shows the p-doped dots represented by regions of high conductivity. A highly

conducting p-type region is also evident on the right side of this image. Aside from the highly conducting p-doped dots, we can see some other effects in this figure.

First, we can see that the dots on the left side of this image are larger than the dots on the right side of this image. This is because the displacement of the AFM's piezoelectric scanner becomes non-linear when it is operated at scan sizes greater than 5 μm .

At various parts of this figure, particularly at the bottom and top, we can see streaks in the conductance image. This is because the SCM probe is intermittently losing electrical contact with the sample. As mentioned in section 5.4, this experiment was performed without AFM control of the probe-surface contact. Had the AFM controlled the probe-surface contact, these streaks would not be present.

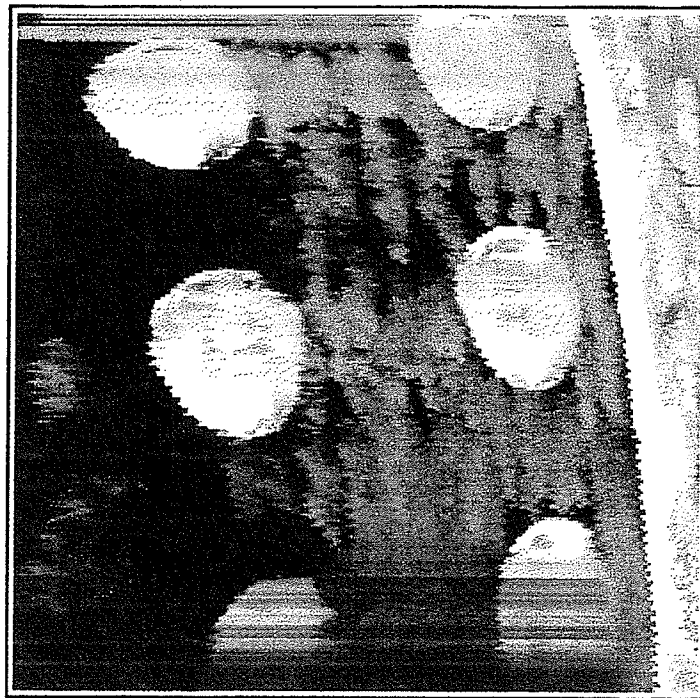


Figure 5.19: Two dimensional current flow image of p-type dots on an n-type surface. The scan measures 7.2 μm x 7.2 μm in size, and was obtained with a molybdenum SCM probe biased to 0.6 V with the p-doped regions electrically grounded.

5.4.2 Lateral Images Of A P-N Junction

Lateral two dimensional conductance images of a P-N junction were performed. For a discussion of how this sample was fabricated, refer to section 5.2. These measurements were performed with a molybdenum SCM probe biased to 0.5 V, with the n-type and p-type regions of the junction electrically grounded. Before SCM measurements were performed, the sample was etched in a buffered oxide etch to remove surface oxide.

Figure 5.20 shows the result of one of these scans. This image measures $7\ \mu\text{m} \times 7\ \mu\text{m}$ in size. The p-type region and n-type region in this image are labeled. A one dimensional cross section of this image, taken across the junction, is shown in Figure 5.21. The current flow data has been converted to conductance data in this figure. For comparison, the dopant profile of this junction as a function of depth is shown in Figure 5.22. Analysis of these figures reveals the following.

- At the far left side of Figures 5.20 and 5.21 (between 0.0 and 0.4 μm in Figure 5.21), we can see that the SCM probe is measuring a region of low conductivity. At this point the sample is changing scan direction. It is thought that at this point the SCM probe is “sticking” to the sample. Sticking will be discussed further in section 5.5.2.
- In Figure 5.20 we can see that there are many streaks present along the X direction. This is due to the SCM probe not having consistent electrical contact with the sample as it is scanned across the surface. As mentioned in section 5.4, this experiment was performed without AFM control of the probe-surface contact.
- From Figures 5.20 and 5.21, we are clearly able to distinguish between the p-type and n-type regions on the sample. We are able to see that the highly doped p-type region (between 0.0 and 4.5 μm) possesses high conductivity. That the conductivity drops to a minimum between 4.5 and 5.5 μm . This corresponds to the lower concentration of p-type dopant near the P-N junction. Finally, that the conductivity increases again in the n-type region between 5.5 and 7.0 μm . These effects agree with the results of the one dimensional conductivity profiles of section 5.3.

- Between the n-type and highly doped p-type regions are two regions of interest, labeled A and B on Figure 5.21.

Region A is the location of a drop in conductivity between the n-type and highly doped p-type regions. At the right side of region A, is the apparent metallurgical junction between the n-type and p-type regions. At the left side of region A is highly doped p-type dopant. Within region A is lower doped p-type dopant. The width of region A is labeled as $0.9 \mu\text{m}$.

The SCM profiles across cleaved P-N junctions (shown in section 5.3) showed that the conductivity of the p-doped region dropped significantly, when the dopant concentration dropped below 10^{20} cm^{-3} . Referring to the dopant profile of this sample (shown in Figure 5.22), we see that the distance separating the 10^{20} cm^{-3} p-doped region and the P-N junction is $1.1 \mu\text{m}$. Since we are making lateral measurements, we would expect to see a drop in conductivity after only 60 - 80 % of this distance.⁵ Thus, we would expect the distance separating the 10^{20} cm^{-3} p-doped region and the P-N junction to be between $0.66 \mu\text{m}$ and $0.88 \mu\text{m}$. This is in close agreement with the $0.9 \mu\text{m}$ width of region A.

At point B in Figure 5.21, we see that the measured conductance is a maximum. This spike could be attributed to two things. First, it may be that the positively biased SCM probe is locally forward biasing the P-N junction, from the p side. This was discussed in section 4.9. Second, this spike could be due to a surface feature which has the effect of increasing the electrical contact area between the SCM probe and the sample. AFM scans of the surface revealed that a 20-100 nm wide trench had formed in the near vicinity of the junction during formation of the P-N junction.

In order to determine which of these two effects may have caused the spike, conductivity scans across the junction were performed with a negatively biased SCM probe. These scans also revealed this spike. Therefore, since the spike appeared in the same location in scans with both positive and negative probe bias voltages, the origin of this spike was attributed to the trench.

⁵ Laterally the dopant diffusion distance should be between 60 - 80 % of the diffusion distance in depth [20].

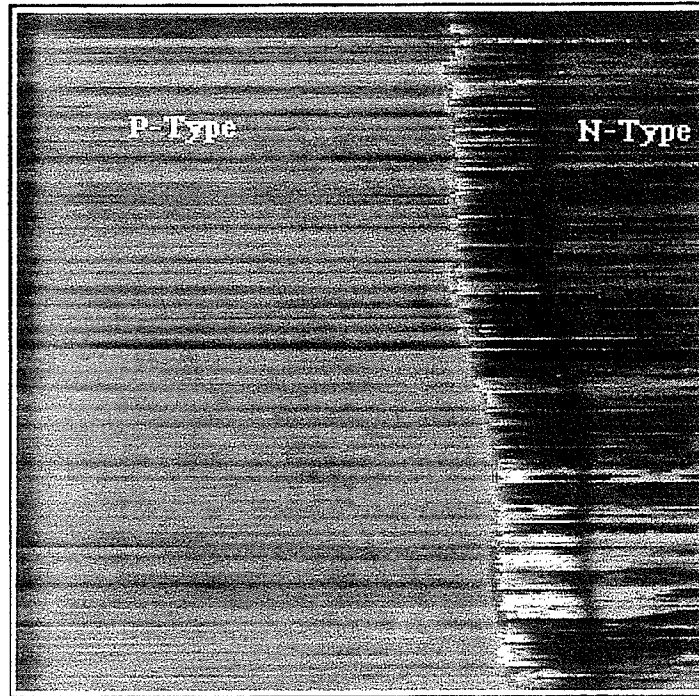


Figure 5.20: Lateral two dimensional current flow image of a p-n junction. The scan is $7\ \mu\text{m} \times 7\ \mu\text{m}$ in size, and was obtained with a molybdenum SCM probe biased to 0.5 V, with the p-type and n-type regions electrically grounded.

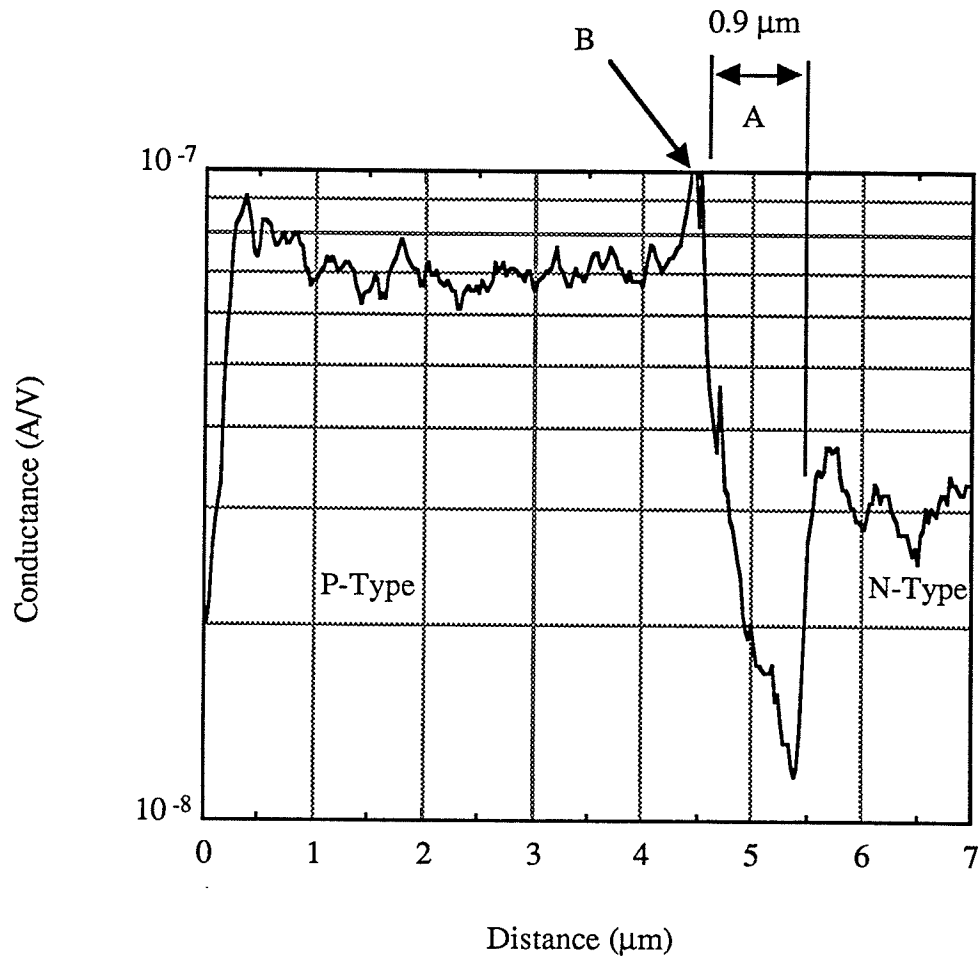


Figure 5.21: One dimensional cross section of the SCM profile of Figure 5.21, taken across the junction. This figure shows the conductivity of the probe-surface interface as the SCM probe is scanned across the junction.

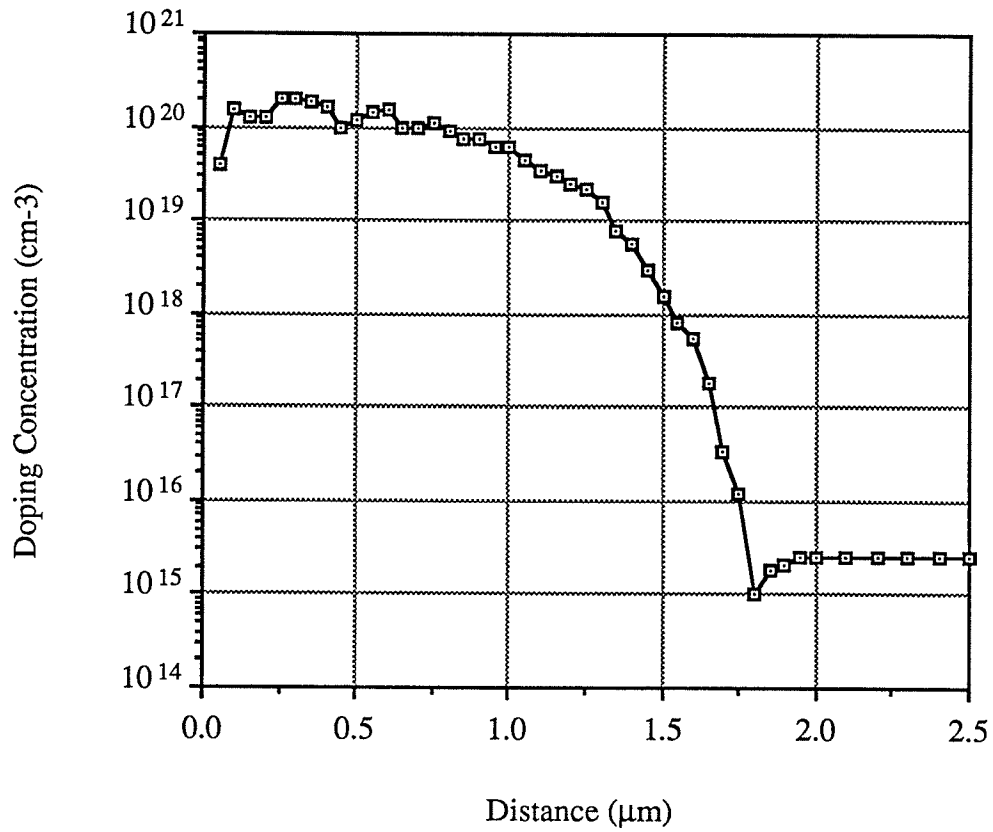


Figure 5.22: Doping profile as a function of depth for the sample of Figure 5.20.

5.4.3 Lateral Images Of Implanted N-Type Lines

As a test of the resolution of the SCM, the SCM was used to locate highly doped $0.1\ \mu\text{m}$ n-type lines implanted on a p-type substrate [50]. The experimental set up is shown in Figure 5.23. The n-type lines were As^+ implanted to $2 \times 10^{14}\ \text{cm}^{-2}$ at 200 keV and annealed at $1050\ ^\circ\text{C}$ for 20 seconds. They were $0.1\ \mu\text{m}$ in width and were implanted with a separation of $0.4\ \mu\text{m}$. The p-type substrate was boron doped to $10^{14}\ \text{cm}^{-3}$. Before SCM measurements were performed, the sample was etched in a buffered oxide etch to remove surface oxide.

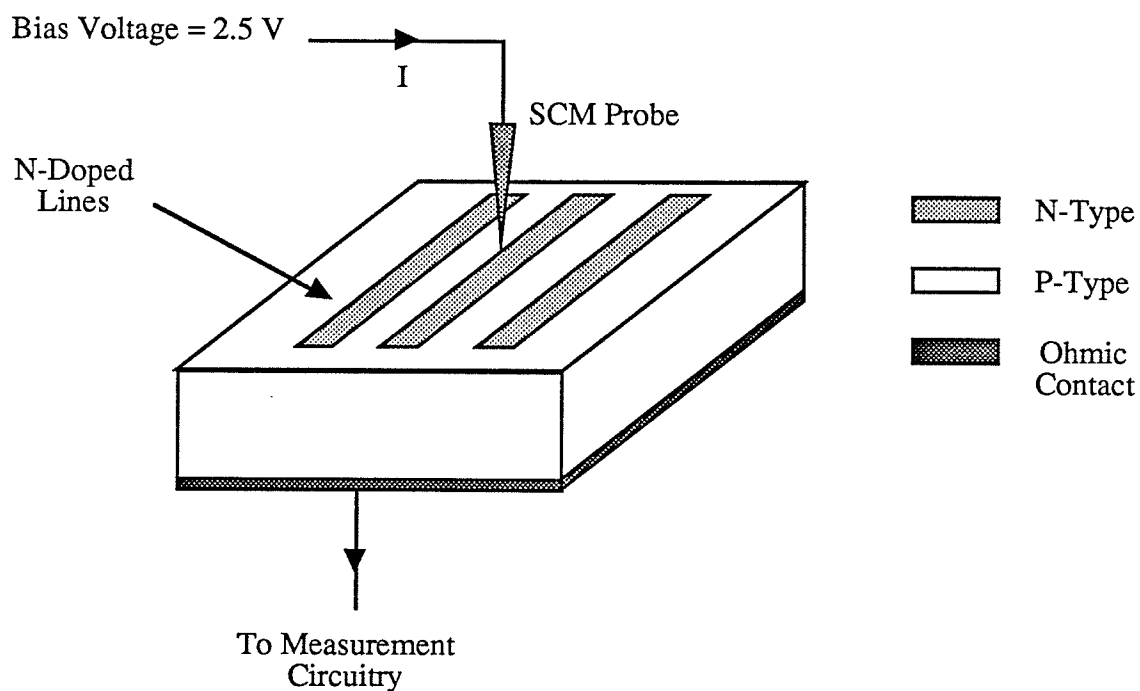


Figure 5.23: Experimental setup used to locate n-type lines on a p-type substrate.

A theoretical analysis of what the expected current flow would be for a positive biased and a negative biased SCM probe is given below.

Positive Biased Probe:

When the SCM probe is over an n-type line, the probe-surface contact would be forward biased. However, the underlying n-type to p-type junction would be reverse biased. Thus, we would expect little current flow. When the probe is over the p-type substrate, the probe-surface contact would be reverse biased. Thus, we would again expect little current flow. However, we may be able to distinguish between n-type and p-type regions, if the reverse saturation currents of the P-N junction and of the probe to p-type-surface junction differ.

Negative Biased Probe:

When a negative biased SCM probe is over an n-type line, the probe-surface contact would be reverse biased. Thus, we would expect little current flow. When the probe is over the p-type substrate, the probe-surface contact would be forward biased. Thus, we would expect significant current flow.

SCM Conductivity Profile:

The theoretical analysis suggests that a negative biased SCM probe should be used. Initial scans were performed successfully with positive bias. Attempts to duplicate this result at a later date with both positive and negative bias voltages failed.

Figure 5.24 shows the result of a $3.6 \mu\text{m} \times 3.6 \mu\text{m}$ scan taken with a tungsten SCM probe biased to 2.5 V. The implanted lines are observed as bright vertical bands in this picture. This image was of exceptionally poor quality and it was necessary to use a wiener filter to enhance the visibility of the n-type lines. A one dimensional cross section taken across this figure is shown in Figure 5.25. This cross section was taken from the original SCM scan, not from the filtered image. Analysis of these figures reveals the

following.

- At the left side of Figures 5.24 and 5.25 (between 0.0 μm and approximately 0.5 μm on Figure 5.25) is evidence of the SCM probe “sticking” to the sample. Sticking will be discussed further in section 5.5.2.
- The spacing between the periodic high conductivity regions of Figure 5.25 is approximately 0.4 to 0.45 μm . This is less than the 0.5 μm spacing of the lines. However, if we remove the approximate 0.5 μm of sticking from the total 3.6 μm length of this scan, we would expand the line spacing by the factor:

$$\frac{3.6}{(3.6 - 0.5)} = 1.16$$

This would result in a line spacing of approximately 0.46 to 0.52 μm . This is closer to the 0.5 μm spacing between the implanted n-type lines.

- After analysis of Figures 5.24 and 5.25, it was thought that the conductive bands in Figure 5.24 may be due to periodic variations in the surface roughness. Such variations would cause like variations in the probe-surface contact area, and thus would show up as variations in the measured conductivity.

AFM topographical scans of the surface were performed to see if this was the case. These scans revealed no such surface roughness. However, the AFM scans were performed after another etch of the sample in a buffered oxide solution. Thus, the result of the AFM scans may not be conclusive.

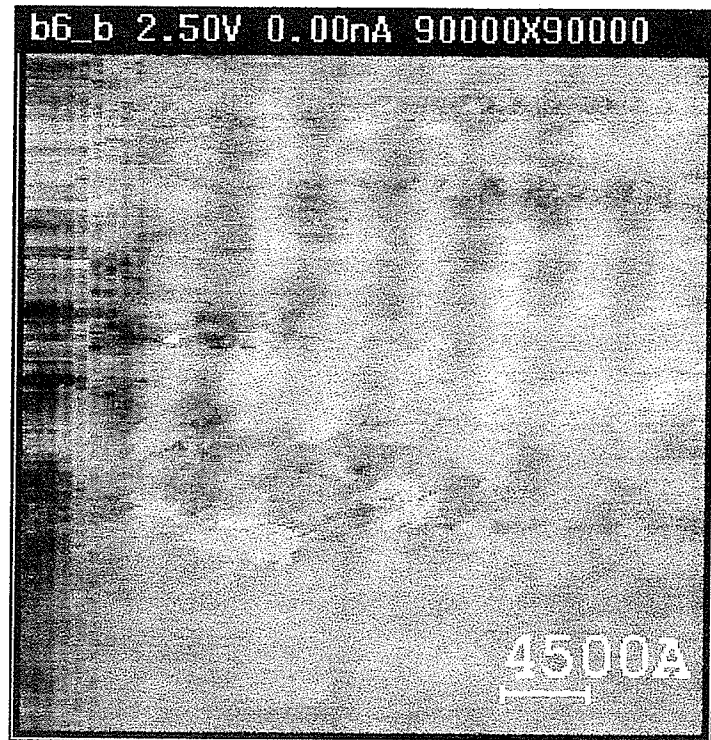


Figure 5.24: Two dimensional current flow image of highly doped implanted n-type lines on a p-type substrate. The scan measures $3.6 \mu\text{m} \times 3.6 \mu\text{m}$ in size, and was obtained with a tungsten SCM probe biased to 2.5 V with the p-doped regions electrically grounded.

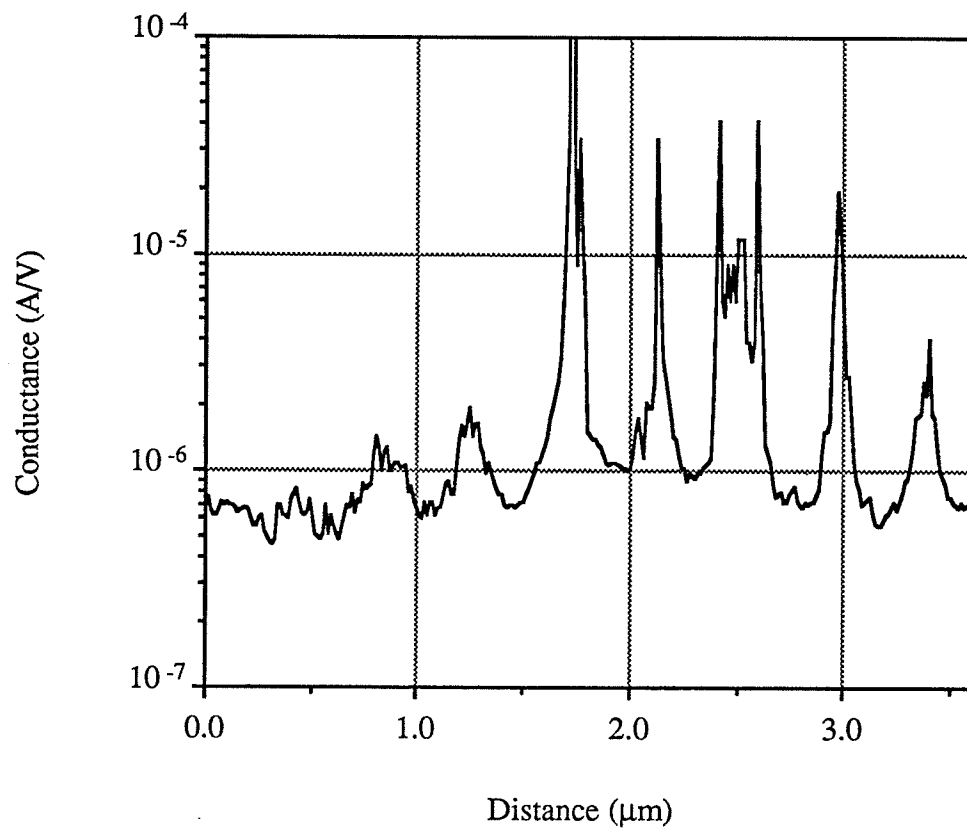


Figure 5.25: One dimensional cross section of the SCM profile of Figure 5.24.

5.5 Experimental Artifacts

5.5.1 Deposited Material By The SCM Probe

Occasionally it was noticed that the SCM probe was depositing a liquid on the sample surface. This "puddle" of liquid increases in size with time as the SCM probe was scanned over the surface. The origin of this liquid is unknown, but it seems to have no effect on the measured probe-sample conductance.

It is thought that this liquid is water present on the SCM probe [26]. Since water is a polar molecule, it would travel toward the SCM probe tip when a bias voltage is applied to the probe. This is because the electric field strength on the SCM probe is highest at the probe tip.

5.5.2 SCM Probe Sticking To The Sample

The SCM probe occasionally has problems measuring the surface conductance when the sample switches scan direction. An example of this effect is shown in section 5.4.2 in Figure 5.20. This effect was attributed to the SCM probe "sticking" to the sample. The size of the area effected by "sticking" increases in size when higher probe-surface contact forces are used, or when lower scan speeds are used. These two facts seem to backup this sticking theory. Sticking can be reduced by using lower probe-surface contact forces, and higher scan speeds.

Sticking is seen only on the far left side of conductance images, because the PC acquires conductance data when the sample travels towards the left.

It is worth noting, that sticking is less of a problem with tungsten probes as opposed to molybdenum probes. This is to be expected since tungsten is more rigid than molybdenum.

5.5.3 Resistive Heating At The Probe-Surface Interface

Resistive heating at the probe-sample interface is caused by the current flow between the SCM probe and the sample. Resistive heating is at a maximum when the

total probe-sample resistance R_T (given by equation 4.2), equals $10\text{ M}\Omega$ (the resistance of the current limiting resistor shown in Figure 3.11).

For example, if the SCM probe is biased to 0.2 V and R_T equals $10\text{ M}\Omega$, the current flow in the circuit is equal to 10 nA . The resistive heating is equal to I^2R and is equal to 1 nW .

5.5.4 Friction Heating At The Probe-Surface Interface

It is possible that the friction acting against the motion of the SCM probe over the sample may cause significant heating at the probe-sample interface. The rate of heating due to friction is equal to:

$$\begin{aligned} \text{Watts} &= (\text{contact force} \times \text{coefficient of friction}) \times (\text{scan speed}) \\ &= (\text{force of friction}) \times (\text{velocity}) \\ &= (\text{Newtons}) \times (\text{meters / second}) \\ &= \text{Joule / second} \end{aligned}$$

For example, suppose the probe-sample contact force is 10^{-6} N , the coefficient of friction is $\mu_T = 1$, and the SCM probe is scanning over the sample at a speed of $100\text{ }\mu\text{m/sec}$. This corresponds to a $5\text{ }\mu\text{m}$ scan performed with the AFM controller set to a scan speed of 10 Hz . The heating due to friction is 0.1 nW . This is within a factor of 10 of the resistive heating of the probe-sample interface.

5.5.5 Differences Between Tungsten And Molybdenum Probes

There were several differences observed between tungsten and molybdenum probes. First, tungsten probes are more robust. They last longer which gives them the ability to provide consistent and repeatable conductance images. Molybdenum probes are damaged easier and must be replaced more often. Second, tungsten probes are more rigid. This makes them less prone to "sticking". However, this also results in the reduced ability of tungsten probes to maintain consistent contact to a surface, when scanned over a surface without AFM control of the contact force.

5.6 Conclusions

The experimental results of this thesis have shown several things.

- The SCM has shown capable of distinguishing between regions of different dopant types on a surface.
- Within a region of given dopant type, the SCM has shown capable of distinguishing between regions with high and low dopant concentrations.
- The SCM has shown capable of measuring the conductivity of a sample beneath the SCM probe accurately as a function of distance. This was achieved with sub-micron resolution.
- SCM measurements of dopant depth over a cleaved P-N junction, agree with depth profiles performed by the spreading resistance technique. However, unlike the spreading resistance technique, beveling of the sample was not required.
- The SCM has shown capable of performing lateral two dimensional conductivity scans of a surface with sub-micron resolution.
- It has been shown that simultaneous topographical and conductivity measurements of a sample surface can be performed.

Chapter 6

RECOMMENDATIONS

Future experiments and analysis should be done in five areas.

- The etching of the SCM probe tips should be studied further, with emphasis on producing probes with consistent radius of curvature tips.
- The fiber interferometer and laser spring deflection sensors should be developed further. The implementation of these sensors would result in lower probe-surface contact forces, and thus, a smaller probe-surface contact radius.
- Experiments should be performed in a vacuum environment to minimize contamination by oxide and other materials.
- Future experiments should be performed over samples with a variety of different dopant levels, to study the measured probe-surface conductivity as a function of doping.
- Experiments should be performed over biased P-N junctions. These experiments should be done with the SCM probe operating such that the probe bias voltage is continuously adjusted, so that zero net current flows between the probe and the sample. The SCM would then be effectively operating as a potentiometer, and thus, would be able to measure the potential drop across a biased P-N junction. Control electronics and software are already in place to perform these measurements.

APPENDIX A

I-V MEASUREMENTS

Presented on the following pages, is the result of multiple I-V measurements performed with three molybdenum probes and three tungsten probes, over n-type and p-type regions of a semiconductor sample. Both the n-type and p-type regions were electrically grounded for these measurements. Dopant concentrations of the n and p regions were $3 \times 10^{15} \text{ cm}^{-3}$ of phosphorus and 10^{20} cm^{-3} of boron respectively, as measured by spreading resistance profiles.

Before the measurements were taken, the sample was etched in a buffered oxide etch to remove surface oxide. The measurements were performed with the SCM probe held stationary over each region during the voltage sweep. Furthermore, these measurements were performed in darkness, in order to minimize carrier generation due to illumination by room lights. A discussion of these measurements is given in section 5.2 of this thesis.

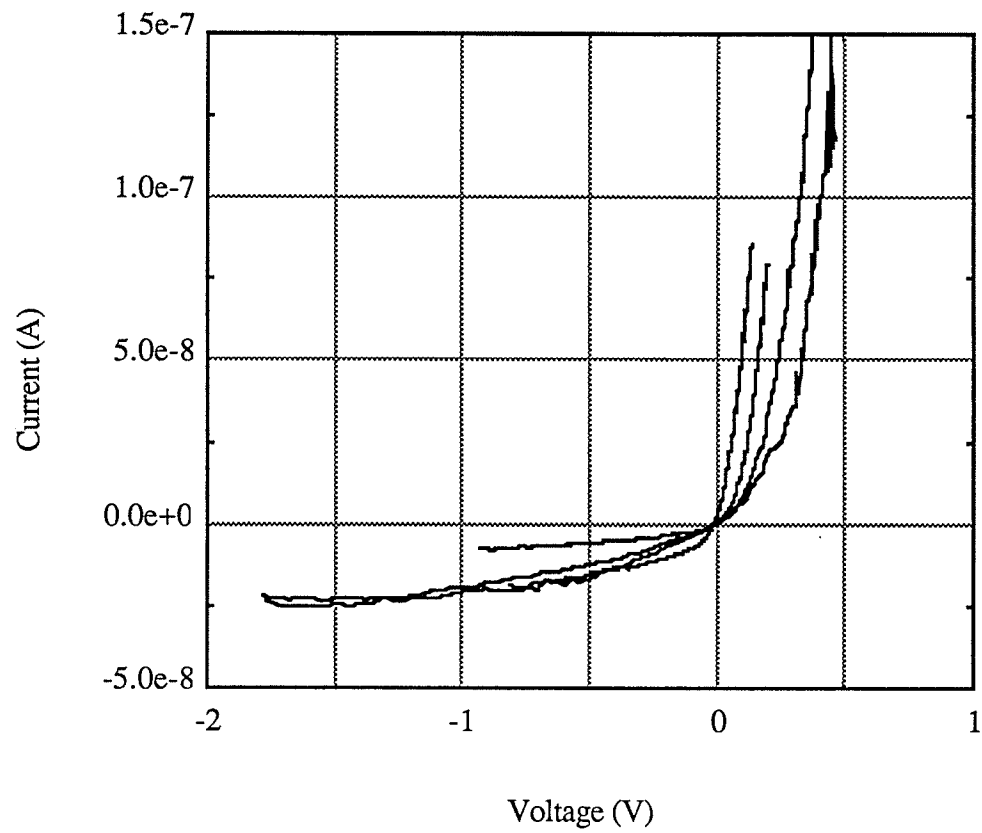


Figure A.1: I-V measurements performed with tungsten probe[#] 1 over the n-type region.

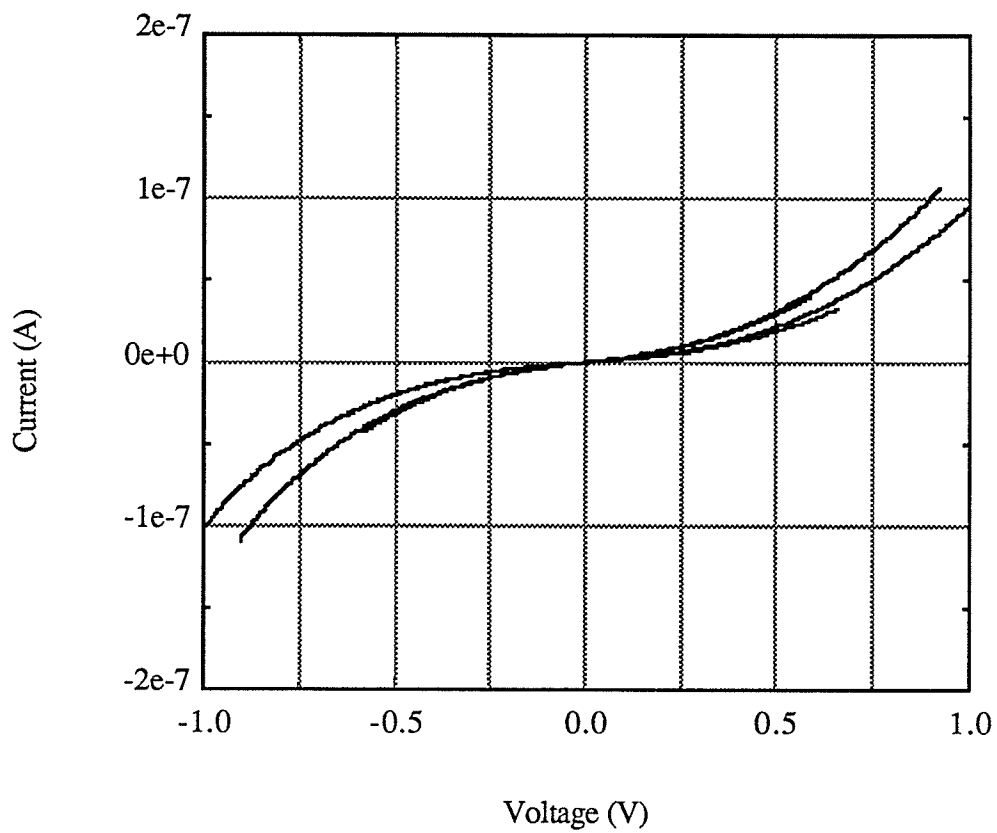


Figure A.2: I-V measurements performed with tungsten probe[#] 1 over the p-type region.

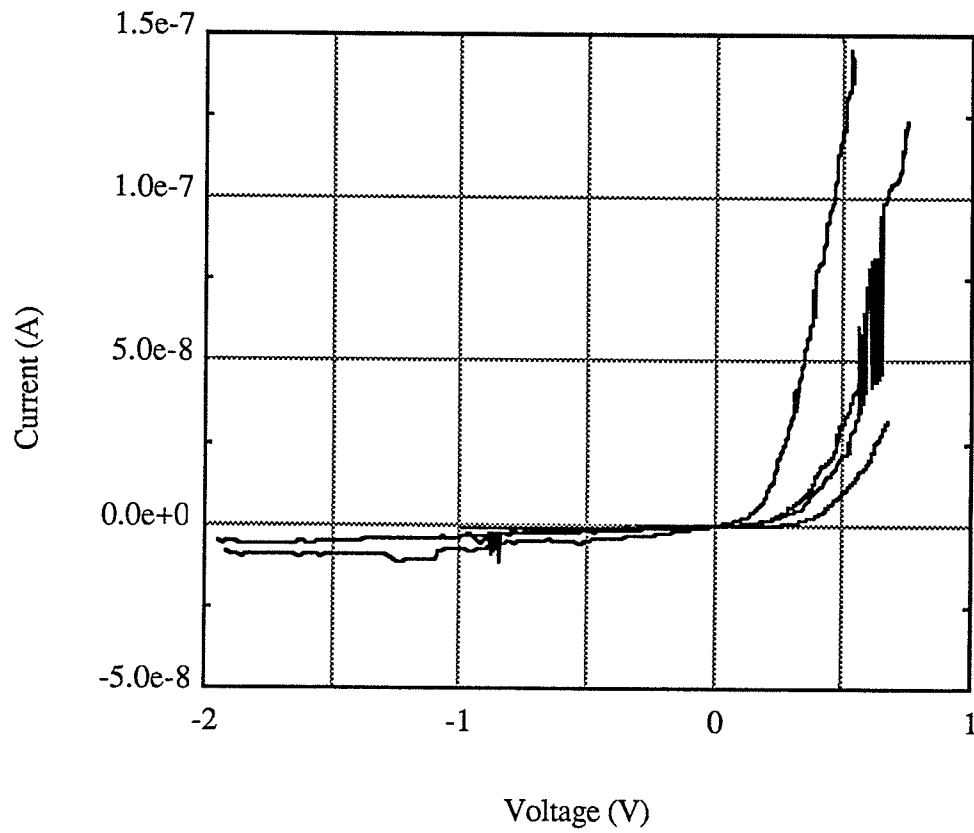


Figure A.3: I-V measurements performed with tungsten probe[#] 2 over the n-type region.

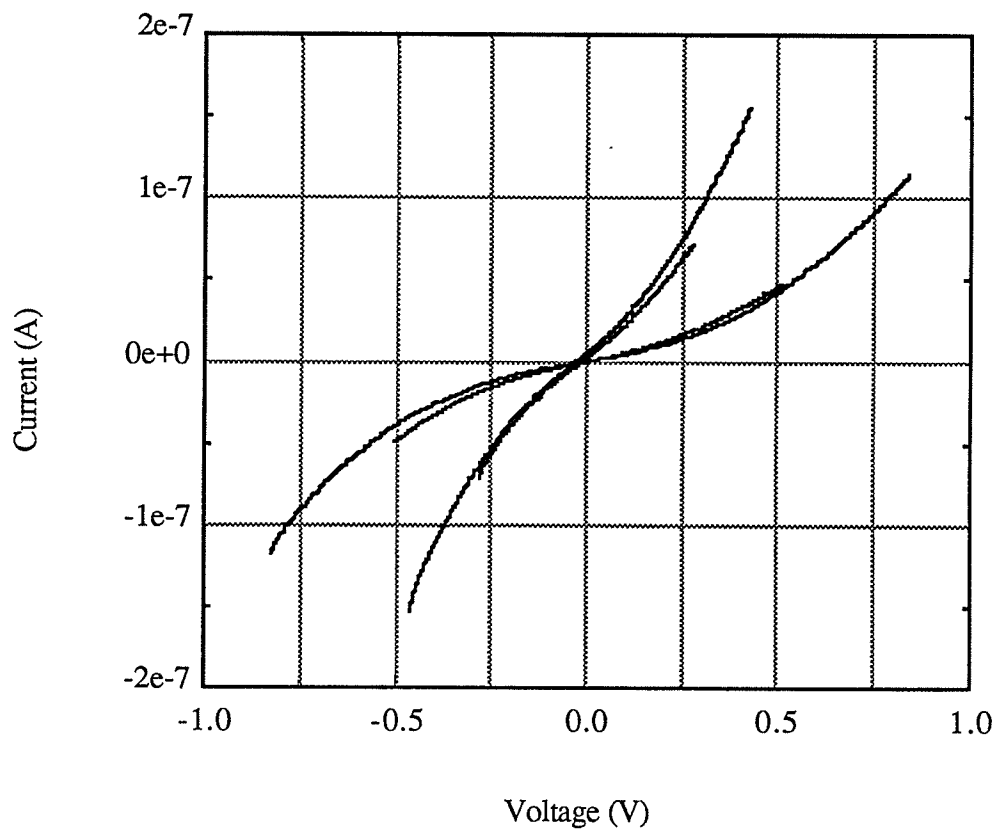


Figure A.4: I-V measurements performed with tungsten probe# 2 over the p-type region.

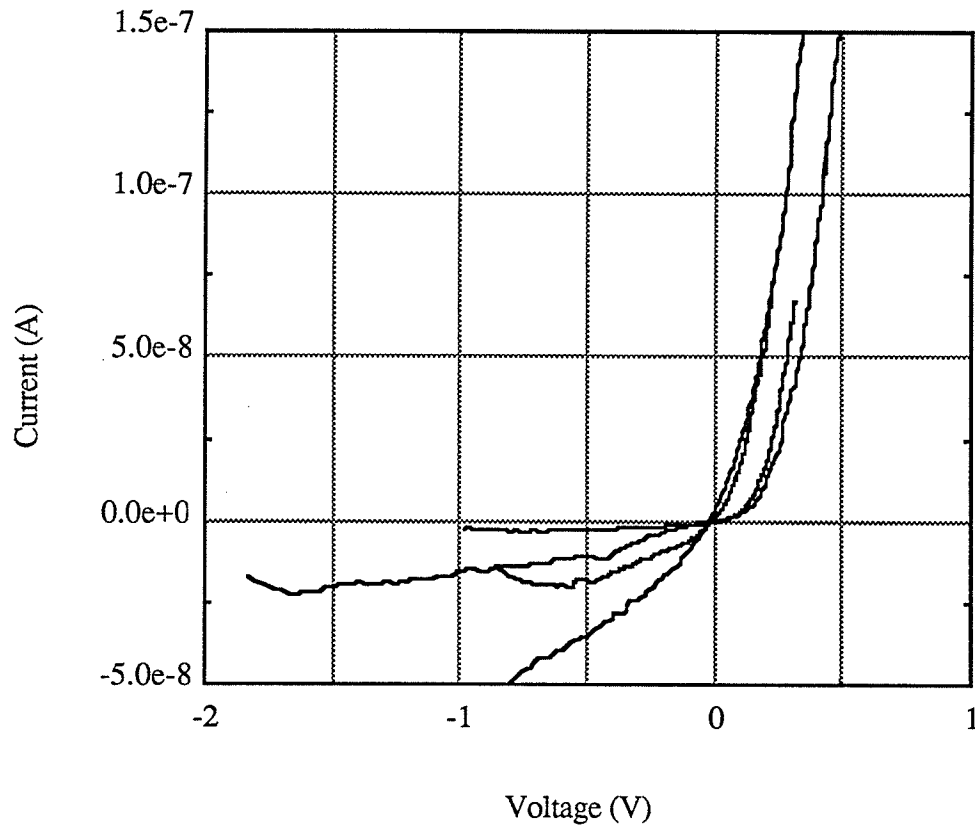


Figure A.5: I-V measurements performed with tungsten probe[#] 3 over the n-type region.

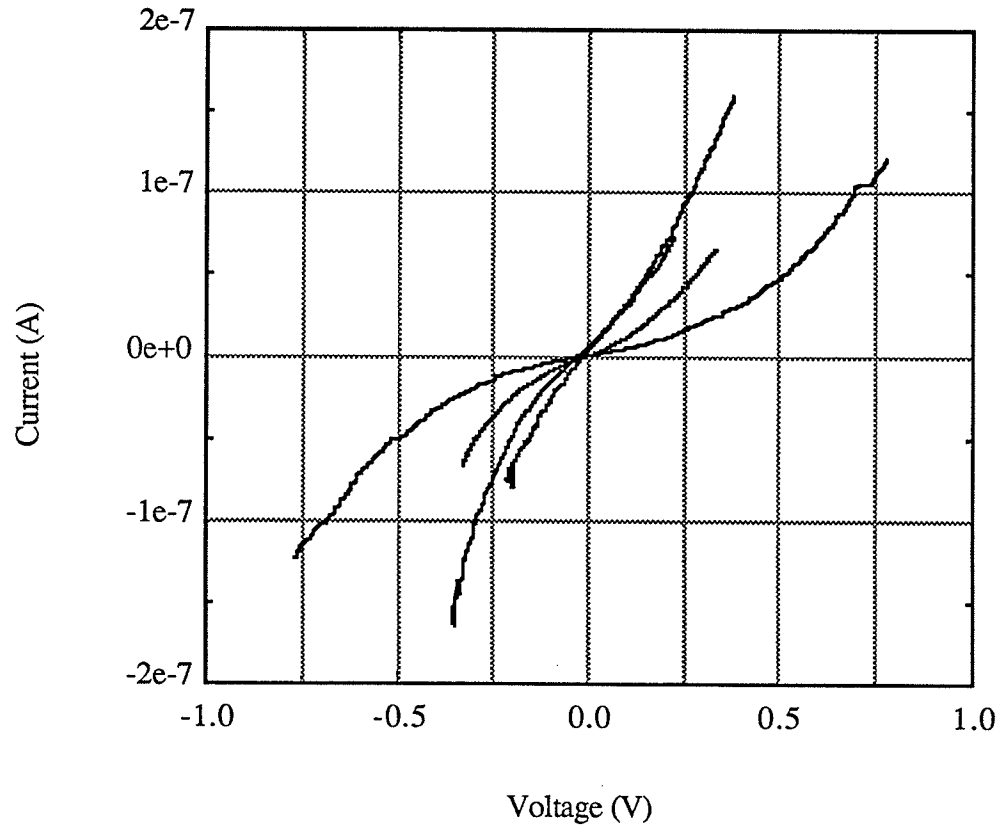


Figure A.6: I-V measurements performed with tungsten probe[#] 3 over the p-type region.

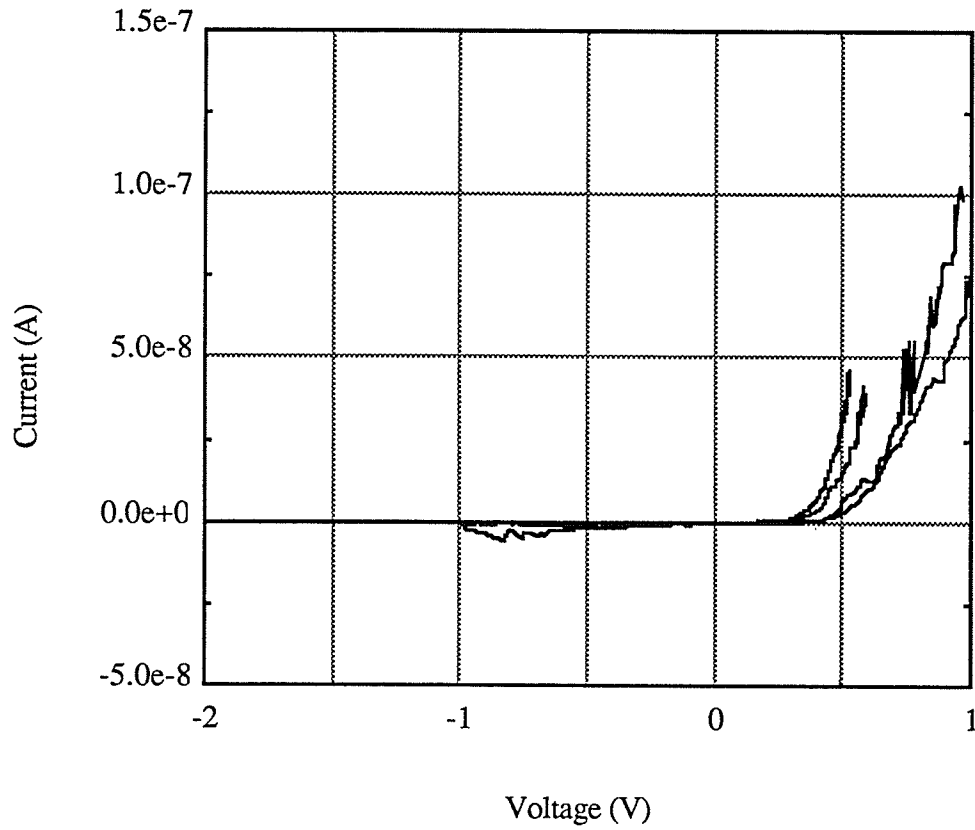


Figure A.7: I-V measurements performed with molybdenum probe# 1 over the n-type region.

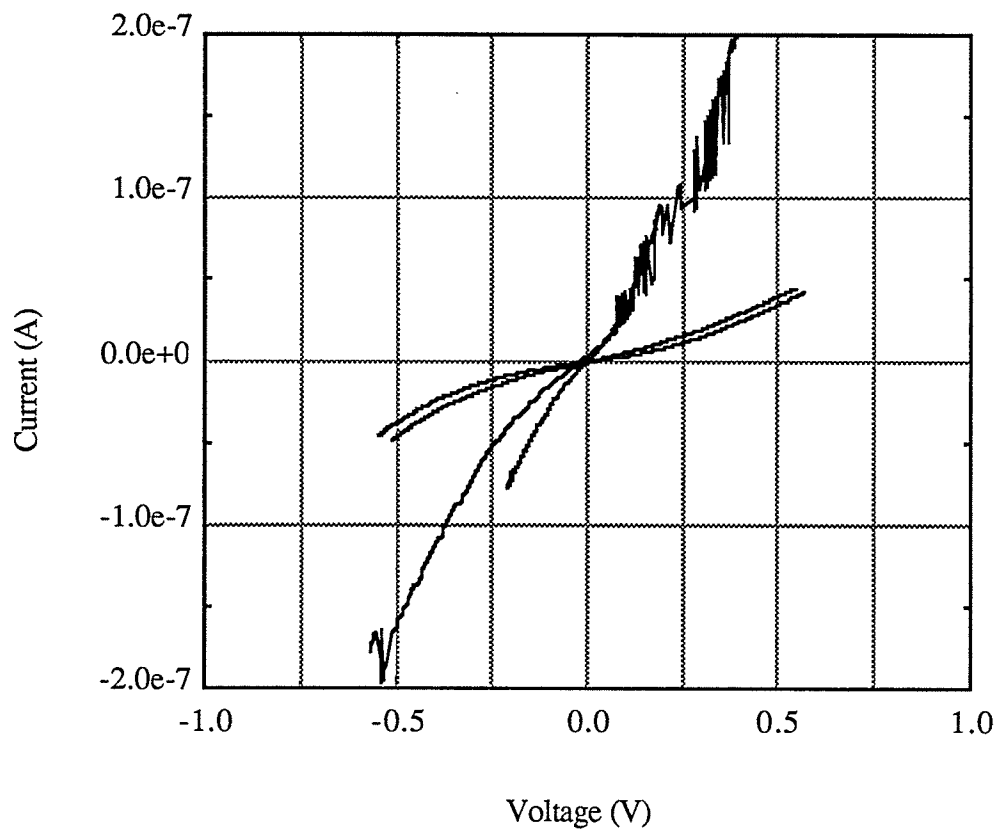


Figure A.8: I-V measurements performed with molybdenum probe# 1 over the p-type region.

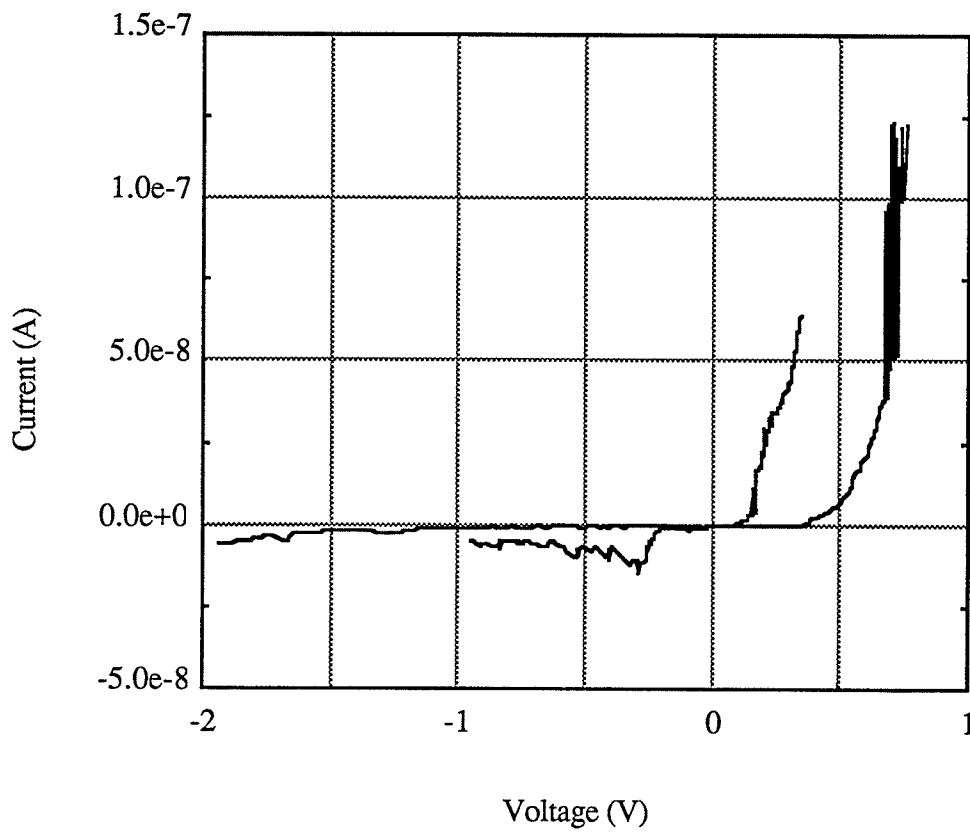


Figure A.9: I-V measurements performed with molybdenum probe[#] 2 over the n-type region.

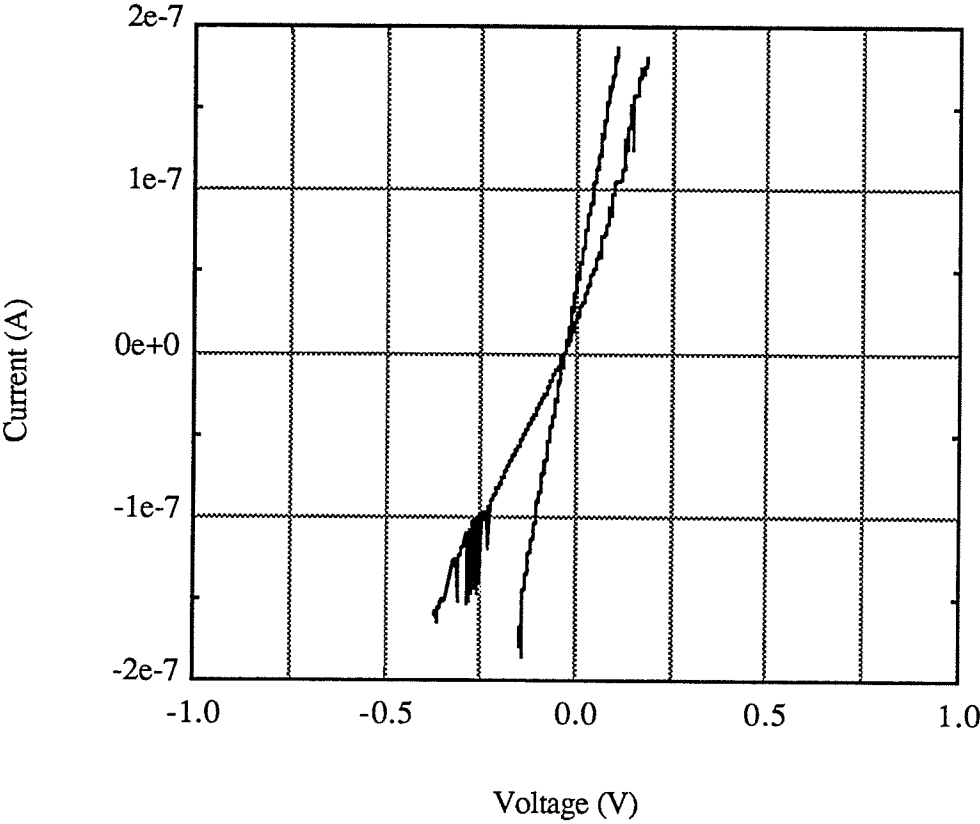


Figure A.10: I-V measurements performed with molybdenum probe# 2 over the p-type region.

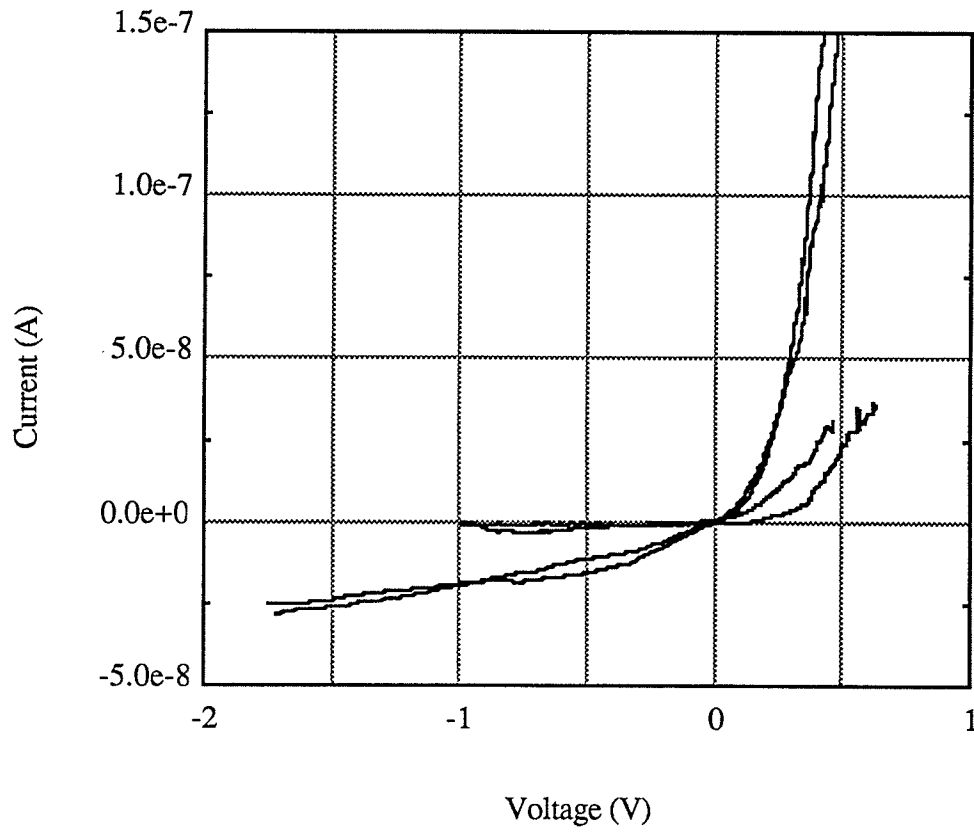


Figure A.11: I-V measurements performed with molybdenum probe# 3 over the n-type region.

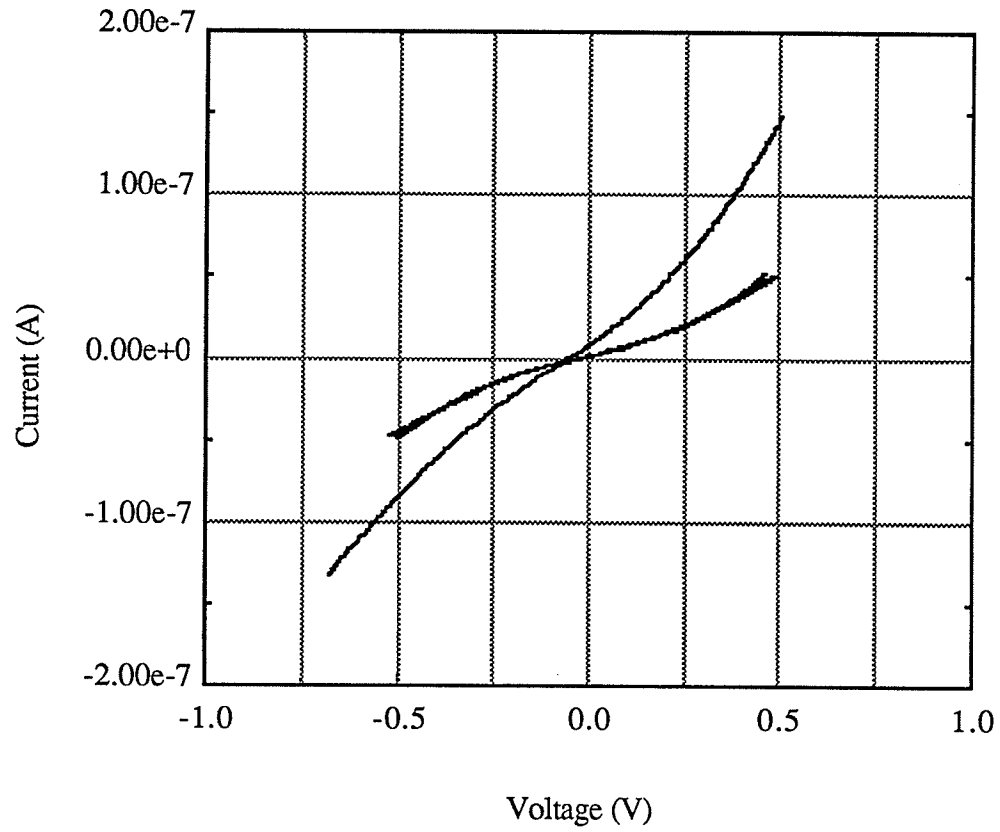


Figure A.12: I-V measurements performed with molybdenum probe# 3 over the p-type region.

REFERENCES

- [1] G. Binnig, C. F. Quate, and Ch. Gerber, "Atomic Force Microscope," *Phys. Rev. Lett.*, vol. 56, pp. 930-933, Mar. 1986.
- [2] D. K. Schroder, "Semiconductor Material And Device Characterization," John Wiley & Sons Inc., New York, 1990.
- [3] S. Wolf, R. N. Tauber, "Silicon Processing For The VLSI Era, Volume 1 - Process Technology," Lattice Press, California, 1986.
- [4] J. H. Linn, E. G. Solley, R. W. Belcher, and M. G. Shlepr, "Electrochemical Etching and Plating for Junction Delineation," *Solid State Technology*, pp. 63-69, Sept. 1991.
- [5] A. Romano-Rodriguez, J. Vanhellefont, A. De Deersgieter, W. Vandervorst, and J. R. Morante, "TEM Techniques For 2D Junction Delineation And Correlation With SIMS And SRP," *Solid State Phenomena*, vol. 19&20, pp. 449-454, 1991.
- [6] J. R. Ehrstein, "Two-Probe (Spreading Resistance) Measurements For Evaluation Of Semiconductor Materials And Devices," chapter 1 of: J. N. Zemel, "Nondestructive Evaluation of Semiconductor Materials and Devices," Plenum Press, New York, 1979.
- [7] R. J. Hillard, R. G. Mazur, H. L. Berkowitz, and P. Rai-Choudhury, "Profiling of Silicon and III-V Compounds by Point Contact Techniques," *Solid State Technology*, pp. 119-125, Aug. 1989.
- [8] W. Vandervorst. and T. Clarysse, "Recent Developments in the Interpretation of Spreading Resistance Profiles for VLSI-Technology," *J. Electrochem. Soc.*, vol. 137, pp 679-683, Feb. 1990.

- [9] H. L. Berkowitz, "The Effects of Surface Charge on Spreading Resistance Profiles Measured on p-on-p⁺ Epitaxial Si Wafers," J. Electrochem. Soc., vol. 137, pp 679-683, Aug. 1990.
- [10] G. Binnig, H. Rohrer, Ch. Gerber, and E. Weibel, "Tunneling through a controllable vacuum gap," Appl. Phys. Lett., vol. 40, pp 178-180, 1982.
- [11] R. H. Bernhardt, "Molecular Microplacement Using A Scanning Tunneling Microscope, MSc. thesis report, June 1990.
- [12] S. Hosaka, S. Hosoki, K. Takata, K. Horiuchi, and N. Natsuaki, "Observation of *pn* junctions on implanted silicon using a scanning tunneling microscope," Appl. Phys. Lett., vol. 53, pp. 487-489, Aug. 1988.
- [13] S. Kordic, E. J. van Leonen, and A. J. Walker, "Two-dimensional imaging of cleaved Si p-n junctions with 30 nm resolution using a UHV scanning tunneling microscope," IEEE Electron Device Letters, vol. 12, pp. 422-424, Aug. 1991.
- [14] S. Kordic, E. J. van Leonen, and A. J. Walker, "Current imaging of cleaved silicon *pn* junctions with an ultrahigh vacuum scanning tunneling microscope," Appl. Phys. Lett., vol. 59, pp. 3154-3156, Dec 1991.
- [15] J. V. LaBrasca, R. C. Chapman, G. E. McGuire, and R. J. Nemanich, "Scanning tunneling microscopy and spectroscopy of *pn* junctions formed by ion implantation," J. Vac. Sci. Technol., vol. B-9, pp. 752-757, Mar.-Apr. 1991.
- [16] H. E. Hessel, U. Memmert, H. Cerva, and R. J. Behm, "Dopant migration in silicon during implantation/annealing measured by scanning tunneling microscopy," J. Vac. Sci. Technol., vol. B-9, pp. 690-694, Mar.-Apr. 1991.
- [17] P. Muralt, "GaAs *pn* junction studied by scanning tunneling potentiometry," Appl. Phys. Lett., vol. 49, pp. 1441-1443, Nov. 1986.

- [18] E. T. Yu, M. B. Johnson, and J.-M. Halbout, "Electrical profiling of Si(001) p - n junctions by scanning tunneling microscopy," *Appl. Phys. Lett.* vol. 61, pp. 201-203, July 1992.
- [19] M. Tanimoto, T. Douseki, and T. Takagami, "Analysis of p - n junction capacitance with three dimensional impurity profiling method using scanning tunneling microscopy," *Jap. Jour. App. Phys.*, vol. 30, pp. 3638-3641, Dec. 1991.
- [20] T. Takigami, and M. Tanimoto, "Measurements of the three-dimensional impurity profile in Si using chemical etching and scanning tunneling microscopy," *Appl. Phys. Lett.* vol. 58, pp. 2288-2290, May 1991.
- [21] D. W. Abraham, C. Williams, J. Slinkman, and H. K. Wickramasinghe, "Lateral dopant profiling in semiconductors by force microscopy using capacitive detection," *J. Vac. Sci. Technol.*, vol. B-9, pp. 703-706, Mar.-Apr. 1991.
- [22] C. C. Williams, J. Slinkman, W. P. Hough, and H. K. Wickramasinghe, "Lateral dopant profiling with 200 nm resolution by scanning capacitance microscopy," *Appl. Phys. Lett.* vol. 55, pp. 1662-1664, Oct. 1989.
- [23] C. C. Williams, J. Slinkman, W. P. Hough, and H. K. Wickramasinghe, "Lateral dopant profiling on a 100 nm scale by scanning capacitance microscopy," *J. Vac. Sci. Technol.*, vol. A-8, pp. 895-898, Mar.-Apr. 1990.
- [24] J. Matey, and J. Blanc, "Scanning capacitance microscopy", *J. Appl. Phys.* vol. 57, pp. 1437-1444, Mar. 1985.
- [25] T. P. Weihs, Z. Nawaz, S. P. Jarvis, and J. B. Pethica, "Limits of imaging resolution for atomic force microscopy of molecules," *Appl. Phys. Lett.*, vol. 59, pp. 3536-3538, Dec. 1991.
- [26] D. J. Thomson, private communication.

- [27] S. Hosaka, H. Koyanagi, T. Hasegawa, S. Hosoki, and A. Hiraiwa, "Observation of natural oxide growth on silicon facets using an atomic force microscope with current measurement," *J. Appl. Phys.*, vol. 72, pp. 688-691, Jul. 1992.
- [28] A. J. Melmed, "The art and science and other aspects of making sharp tips," *J. Vac. Sci. Technol.*, vol. B-9, pp. 601-608, Mar.-Apr. 1991.
- [29] H. Lemke, T. Goddenhenrich, H. P. Bochem, U. Hartmann, and C. Heiden, "Improved microtips for scanning probe microscopy," *Rev. Sci. Instrum.*, vol. 61, pp. 2538-2541, Oct. 1990.
- [30] L. A. Nagahara, T. Thundat, and S. M. Lindsay, "Preparation and characterization of STM tips for electrochemical studies," *Rev. Sci. Instrum.*, vol. 60, pp. 3128-3130, Oct. 1989.
- [31] D. Rugar, H. J. Mamin, and P. Guethner, "Improved fiber-optic interferometer for atomic force microscopy," *Appl. Phys. Lett.*, vol. 55, pp. 2588-2590, Dec. 1989.
- [32] S. Breen, B. E. Paton, B. L. Blackford, and M. H. Jericho, "Fiber optic displacement sensor with subangstrom resolution," *Applied Optics*, vol. 29, pp. 16-18, Jan. 1990.
- [33] Technical Staff, "Digital Instruments NanoScope™ I Scanning Tunneling Microscope Instruction Manual Version 1.1," Digital Instruments Inc., Santa Barbara, California, 1988.
- [34] J. P. Den Hartog, "Mechanical Vibrations," McGraw-Hill Book Company Inc., New York, 1947.

- [35] S. Kordic, E. J. van Loenen, D. Dijkkamp, A. J. Hoeven, and H. K. Moraal, "Scanning tunneling spectroscopy on cleaved silicon *pn* junctions," *J. Vac. Sci. Technol.*, vol A-8, pp. 549-552, Jan/Feb 1990.
- [36] H. K. Henisch, "Rectifying Semi-Conductor Contacts," Oxford University Press, Glasgow, 1957.
- [37] S. M. Sze, "Physics of Semiconductor Devices," John Wiley & Sons Inc., New York, 1981.
- [38] H. C. Card, and E. H. Rhoderick, "Studies of tunnel MOS diodes, I. Interface effects in silicon Schottky diodes," *J. Phys. D: Appl. Phys.*, vol. 4, pp. 1589-1601, 1971.
- [39] W. Shockley, "Electrons and Holes in Semiconductors," D. Van Nostrand Company Inc., New Jersey, 1959.
- [40] E. H. Rhoderick, and R. H. Williams, "Metal-Semiconductor Contacts," Oxford University Press, New York, 1988.
- [41] K. C. Kao, W. Hwang, "Electrical Transport In Solids," Pergamon Press, Oxford, 1981.
- [42] C. Weaver, "Adhesion of thin films," *J. Vac. Sci. Technol.*, vol. 12, pp. 18-25, Jan./Feb. 1975.
- [43] C. Kittel, H. Kroemer, "Thermal Physics," W. H. Freeman and Company, San Francisco, 1980.

- [44] D. Redfield, "Revised model of asymmetric p-n junctions," *Appl. Phys. Lett.* vol. 35, pp. 182-184, July 1979.

- [45] C. Julian Chen, "Electromechanical deflections of piezoelectric tubes with quartered electrodes," *Appl. Phys. Lett.*, vol. 60, pp. 132-134, Jan. 1992.

- [46] E. A. Taft, "Growth of Native Oxide on Silicon," *Journal of the Electrochemical Society*, vol. 135, pp. 1022-1023, April 1988.

- [47] Spreading resistance profiles by Solecon Laboratories Inc., San Jose, California.

- [48] Sample supplied by Y. Loke, Alberta Microelectronics Center, Edmonton, Canada.

- [49] Sample supplied by M. Normandin, Northern Telecom Limited, Ottawa, Canada.

- [50] Sample supplied by G. A. Mattiussi, and P. J. Scanlon, Queen's University, Kingston, Canada.